

**UCSF**

**UC San Francisco Electronic Theses and Dissertations**

**Title**

Patient-Specific Mechanical Analysis of Atherosclerotic Arteries with Resolved Pre- and Post-Rupture Intraplaque Composition

**Permalink**

<https://escholarship.org/uc/item/1155h9rv>

**Author**

Leach, Joseph R.

**Publication Date**

2009

Peer reviewed|Thesis/dissertation

Patient-Specific Mechanical Analysis of Atherosclerotic Arteries with Resolved  
Pre- and Post-Rupture Intraplaque Composition

by

Joseph Ryan Leach

DISSERTATION

Submitted in partial satisfaction of the requirements for the degree of

DOCTOR OF PHILOSOPHY

in

BIOENGINEERING

in the

GRADUATE DIVISION

of the

UNIVERSITY OF CALIFORNIA, SAN FRANCISCO

AND

 UNIVERSITY OF CALIFORNIA, BERKELEY

Copyright (2009)  
by  
Joseph Ryan Leach

## Acknowledgements

I would like to thank my friends and family, who have always been patient, supportive, and encouraging. Without you, I might have ended up as a really sub-par amateur skateboarder or a terrible out-of-work comedian. I am so fortunate to have you all in my life. Thank you.

For the past four years, I have enjoyed working in the Vascular Imaging Research Center at the SFVA Medical Center. I am lucky to be part of such a wonderful team, and I have learned a great deal about medicine, science, life, and friendship during my time there. Gabriel Acevedo-Bolton, Loic Bousset, and Hannes Kroll are great friends, excellent teachers, and unparalleled coworkers. I couldn't think of a better group to spend my days with. I must give special thanks to Vitaliy Rayz for being not only a great friend, but also an unwavering source of encouragement and mentorship. Lastly, I would like to thank our team leader David Saloner. David has been a large influence on me as a scientist and as a person and I consider myself lucky to know him. While I must have caused him some frustration through the years, David was always supportive of my ideas and plans, and showed more patience than I thought was humanly possible. David also sets a fine example of how to be a physicist in the world of medicine, something that will undoubtedly help me for years to come. Thank you David.

Outside of our team, I would like to thank Mohammad Mofrad and Sharmila Majumdar. Mohammad has been a great adviser to me during the past few years, and amidst all the fun of our conversations, Mohammad has helped me to better understand the role of physics and computation in medicine. Sharmila was my academic adviser, and handled my paperwork delinquency with the utmost grace. More importantly,

Sharmila was always willing to listen to my concerns and provided much needed encouragement at some very key moments. Thank you Mohammad and Sharmila.

I would also like to thank Joe Rapp, Stan Berger, SarahJane Taylor, Steve Conolly, and Liang Ge for all the help they have been to me over the past four years. I have not only learned from them all, but I have directly benefitted from their generosity and enthusiasm. Thank you all.

# Patient-Specific Mechanical Analysis of Atherosclerotic Arteries with Resolved Pre- and Post-Rupture Intraplaque Composition

Joseph Ryan Leach

Atherosclerotic plaque rupture at the carotid bifurcation is a major cause of stroke. While plaques vulnerable to rupture progress under significant influence from the local biochemical environment, and often experience a chronic or acute inflammatory process, mechanical forces are also of importance. Finite element studies have been conducted on models of diseased vessels to elucidate the effects of lesion characteristics on the stresses within plaque materials. Ultimately, it is hoped that patient-specific biomechanical analyses may serve as a robust clinical tool to assess the rupture potential for any particular lesion, allowing better stratification of patients into the most appropriate treatment plans.

The relationship between various mechanical descriptors such as stresses or strains and rupture vulnerability is incompletely known, however, and the patient-specific utility of biomechanical analyses is thus unclear. Progress on this front has been impeded by several distinct challenges. First, data on *in vivo* plaque rupture, under normal physiologic conditions, is unfortunately sparse. Second, methods for building highly realistic patient-specific finite element models of diseased vessels are lacking, and the simplifications common in the literature may render current analyses inadequate. Third, the time and computational resource demands of realistic analyses including fluid-structure interaction prohibit large-scale investigation.

In this dissertation, a strategy for accurate and efficient patient-specific modeling of the atherosclerotic carotid bifurcation is developed. We present surface-based methods for rapid yet detailed geometric discretization of image-derived vessel features, allowing for highly resolved stress calculations. A two-stage solution method is also introduced to compliment the unstructured meshes representing different tissues, allowing sizeable reductions in the time and computing resources needed for arterial fluid-structure interaction simulations.

Using these methods, we present a fluid-structure interaction analysis of a patient for whom pre- and post-rupture imaging data is available. The effects of image imprecision on the calculated stress fields are characterized to further elucidate challenges of image-based modeling. We find that plaque rupture location and extent, derived from post-rupture imaging data, correspond well to a region of elevation in first principal stress within the fibrous plaque layer of the lesion.

# Contents

ACKNOWLEDGEMENTS.....	iii
ABSTRACT.....	v
LIST OF TABLES.....	xi
LIST OF FIGURES.....	xii
Chapter 1 – INTRODUCTION.....	1
1.1 The Circulatory System.....	1
1.1.1 – The Conducting Vessels.....	2
1.1.2 The Carotid Arteries.....	5
1.2 Atherosclerosis.....	6
1.3 Carotid Plaque Stability, Rupture, and Stroke.....	10
1.4 Plaque Characterization.....	13
1.5 The Role of Medical Imaging in Plaque Characterization.....	17
1.5.1 Magnetic Resonance Imaging.....	18
1.5.2 Computed Tomography.....	21
1.5.3 Ultrasound.....	23
1.6 A More Comprehensive Assessment of Vulnerability and Rupture Risk.....	24
1.7 Literature Review – FEM Studies of Atherosclerotic Vessels.....	26
1.7.1 Idealized Diseased Vessels.....	26
1.7.2 Studies on Calcification.....	28
1.7.3 2D Patient-Specific FEM Studies.....	29
1.7.4 3D Patient-Specific FEM Studies.....	34



1.8 Toward an Understanding of Plaque Rupture.....	36
Chapter 2 – METHODS.....	39
2.1 Geometry.....	40
2.1.1 Imaging.....	40
2.1.2 Segmentation Strategy.....	41
2.1.3 3D Active Contour Segmentation and Manual Segmentation.....	44
2.1.4 Geometry Reconstruction from Segmented Images.....	47
2.1.5 Fibrous Plaque Layer.....	55
2.1.6 Final Geometry.....	56
2.2 Physics.....	58
2.2.1 Physics of the Vessel Wall.....	58
2.2.2 Physics of Flowing Blood.....	60
2.2.3 Interactions Between the Vessel Wall and Flowing Blood.....	61
2.3 Materials.....	62
2.3.1 Large Deformation Mechanics.....	63
2.3.2 Constitutive Relation for Diseased Carotid Bifurcation Tissues.....	65
2.3.3 Material Properties of Blood.....	68
2.4 Loading and Boundary Conditions.....	69
2.4.1 Construction of Patient-Specific Flow Boundary Conditions.....	70
2.4.2 Pressure Boundary Condition.....	74

2.4.3	Vessel Displacement Boundary Conditions.....	74
2.5	Geometric Discretization.....	75
2.5.1	Basic Requirements for Finite Element Mesh of Multi-Component Arterial Models.....	75
2.5.2	Construction of the 3D Multi-Component Finite Element Mesh.....	78
2.6	Finite Element Representation of Physics.....	84
2.6.1	Solid Domain FEM.....	84
2.6.2	Fluid Domain FEM.....	87
2.6.3	Fluid-Structure Interaction.....	90
2.7	Finite Element Representation of Flow Boundary Conditions.....	92
Chapter 3 –	TWO STAGE SOLUTION.....	99
3.1	Geometry Partitioning.....	102
3.2	Mesh Generation – Fine Model.....	103
3.3	Mesh Generation – Coarse Model.....	104
3.4	Solution Strategy.....	105
3.5	Computation Time Reduction Test.....	106
3.5.1	Computation Time Results.....	107
3.6	Accuracy of Two-Stage Approach.....	108
3.6.1	Effects of Solid Domain Truncation.....	108
3.6.2	Effects of Fluid Domain Truncation.....	110
Chapter 4 –	FSI STRESS ANALYSIS.....	114
4.1	Patient Data.....	114

4.2 Construction of the Geometric Model.....	116
4.3 Computational Mesh.....	116
4.3.1 Mesh Dependence of Displacement Solution.....	117
4.3.2 Mesh Dependence of Stress Field Prediction.....	120
4.3.3 Mesh Dependence of Pressure Field Prediction.....	122
4.4 Loading, Boundary Conditions, and Materials.....	126
4.5 FSI Stress Analysis.....	128
4.6 Results.....	128
4.6.1 First Stage Flow Results.....	128
4.6.2 Second Stage Flow Results.....	131
4.6.3 Second Stage Stress Results.....	132
4.7 Effects of Imaging Imprecision.....	139
Chapter 5 – DISCUSSION AND FUTURE WORK.....	148
5.1 Geometric Modeling and Two-Stage Solution.....	148
5.2 FSI Stress Analysis.....	152
Chapter 6 – CONCLUSION.....	160
REFERENCES.....	162
APPENDIX.....	178

# List of Tables

Table 1.1	Major and minor criteria for plaque vulnerability.....	16
Table 2.1	Hounsfield units used for plaque and vessel segmentation in CTA studies.....	42
Table 2.2	Volumes of triangulation surface meshes before and after Gaussian smoothing and remeshing.....	52
Table 2.3	Material parameters used to define vessel and plaque materials.....	68
Table 2.4	Bounding surfaces for each material in the vessel wall.....	80
Table 3.1	Simulation runtimes for two-stage solution test.....	108
Table 4.1	Mesh density scheme used in solid domain mesh tests.....	121
Table 4.2	Element counts for solid domain test meshes.....	121
Table 4.3	First principal stress dependence on mesh density.....	122
Table 4.4	Volumes of original and modified lipid pools within region of interest.....	141

# List of Figures

Figure 1.1	Cross-section of typical conducting artery.....	3
Figure 1.2	Location of carotid bifurcation.....	5
Figure 1.3	Representative geometry and dimensions of healthy carotid bifurcation.....	6
Figure 1.4	Schematic representation of thin-cap fibroatheroma.....	16
Figure 1.5	Comparison of 2D, 3D, and 3D FSI stress predictions.....	36
Figure 2.1	Axial, sagittal, and coronal views of carotid artery with CTA.....	41
Figure 2.2	Outer wall of carotid bifurcation exposed during surgery.....	43
Figure 2.3	Semi-automatic segmentation of lumen and lipid pool.....	46
Figure 2.4	Segmentation of lumen, lipid pool, and fibrous tissue.....	47
Figure 2.5	Lumen surface before and after Gaussian smoothing.....	49
Figure 2.6	Lipid pool surface before and after Gaussian smoothing.....	49
Figure 2.7	Outer vessel wall before and after Gaussian smoothing.....	50
Figure 2.8	Lipid pool surface before and after remeshing.....	51
Figure 2.9	Deviation of final lumen surface from original triangulation.....	52
Figure 2.10	Deviation of final lipid pool surface from original triangulation.....	53
Figure 2.11	Deviation of final outer vessel wall surface from original triangulation.....	54
Figure 2.12	Consecutive CTA slices and geometric model slices shown side-by-side.....	57
Figure 2.13	General body used for physics definitions.....	59

Figure 2.14	Typical CCA blood pressure waveform.....	69
Figure 2.15	Simple 2D mesh showing node-matching at material boundaries.....	76
Figure 2.16	NURBS surface representations of vessel and plaque components.....	78
Figure 2.17	Formation of ICA outlet end caps.....	79
Figure 2.18	Mutual trimming of lumen and fibrous plaque NURBS surfaces.....	80
Figure 2.19	Re-partitioning of NURBS surfaces for mesh generation.....	82
Figure 2.20	Cut-open view of multi-component volume mesh.....	83
Figure 2.21	CCA inlet mesh, showing main nodes and boundary nodes.....	93
Figure 2.22	Rotation of CCA inlet mesh to align surface normal and global z-axis.....	94
Figure 2.23	Determination of equivalent radius for Womersley mapping.....	95
Figure 2.24	CCA flow rate waveform used for Womersley mapping test.....	96
Figure 2.25	Computational meshes used for Womersley mapping test.....	96
Figure 2.26	Flow rate relative error curves from Womersley mapping test.....	98
Figure 3.1	Truncation planes bounding region of interest.....	102
Figure 3.2	Construction of truncation plane end caps.....	103
Figure 3.3	Surface and volume meshes for region of interest.....	104
Figure 3.4	Volume mesh of full domain, and mesh conformity at truncation plane.....	105
Figure 3.5	Further truncation of region of interest for two-stage solution test.....	109
Figure 3.6	Stress results for two-stage solution test.....	110
Figure 3.7	Pressure field solution from full domain model and	

	two-stage solution.....	111
Figure 3.8	Nodal pressure comparison between full domain model and two-stage solution.....	112
Figure 4.1	Selected images from pre- and post- plaque rupture CTA studies.....	115
Figure 4.2	Test model and meshes used to investigate mesh dependence of displacement solutions.....	118
Figure 4.3	Nodal positions on unloaded lumen during mesh test.....	118
Figure 4.4	Nodal positions on pressurized lumen during mesh test.....	119
Figure 4.5	Nodal positions on outer wall surface of pressurized vessel during mesh test.....	120
Figure 4.6	Steady-state pressure distribution on 5 progressively finer fluid meshes.....	124
Figure 4.7	Mesh dependence of selected pressure measurements.....	124
Figure 4.8	Final fluid mesh used for FSI stress analysis.....	125
Figure 4.9	Flow rate boundary conditions for FSI stress analysis.....	126
Figure 4.10	Pressure and Velocity field predictions at key cardiac phase.....	129
Figure 4.11	Close-up views of prominent flow features.....	131
Figure 4.12	First- and second-stage flow field solutions.....	132
Figure 4.13	Cut-planes on which stresses are presented.....	134
Figure 4.14	First principal stresses within fibrous plaque layer.....	137
Figure 4.15	Fibrous plaque stresses at lumen surface.....	138
Figure 4.16	Surface representations of original and modified lipid pools.....	141
Figure 4.17	Fibrous plaque stresses for slices 1-3 (for models with	

	dilated lipid pool).....	142
Figure 4.18	Fibrous plaque stresses for slices 4-6 (for models with dilated lipid pool).....	143
Figure 4.19	Effects of improper smoothing of stress results.....	145
Figure 4.20	Peak stress trends with lipid pool dilation.....	146
Figure 4.21	Fibrous plaque stresses at lumen surface as a function of lipid pool dilation.....	147
Figure 4.22	Fibrous plaque stresses at the lumen surface for 0.4 mm lipid surface offset.....	147



# Chapter 1 – Introduction

Although the ultimate goal of vascular mechanics analyses is often a deeper understanding of pathology, it is imperative to first understand the structure of healthy vessels. The following serves to present the healthy structure and function of the carotid bifurcation within the context of the greater circulatory system.

## 1.1 The Circulatory System

The vasculature comprises the arterial and venous vessels, which convey blood away from and toward the heart, respectively. Every cardiac cycle, oxygenated blood is pumped from the heart into the systemic arteries. The aorta is the largest systemic artery (lumen diameter  $\sim 2.5\text{cm}$ ), and receives blood directly from the left ventricle through the aortic valve. From the aorta, oxygenated blood passes to the other conducting arteries (diameter  $\sim 2.5\text{cm} - 1\text{cm}$ ), which convey blood to the various anatomical regions. Next, blood is distributed through a branching series of tapering vessels (diameter  $\sim 1\text{cm} - 300\mu\text{m}$ ) until it reaches the arterioles (diameter  $\sim 300\mu\text{m} - 10\mu\text{m}$ ) and capillary beds (diameter  $\sim 10\mu\text{m} - 8\mu\text{m}$ ), where the blood exchanges gases, nutrients, and wastes with the body. The deoxygenated blood is collected by a network of venules and is carried by the systemic veins back to the right atrium of the heart. Next, blood is pumped from the right atrium, through the tricuspid valve, into the right ventricle. The two pulmonary arteries arise from the pulmonary trunk, just past the pulmonary valve, to convey deoxygenated blood from the right ventricle of the heart into a tree-like structure of smaller arterioles in the lungs. These arterioles in turn feed into a branching system of

even smaller pulmonary capillaries. The pulmonary capillaries allow gaseous diffusion to occur between the blood and the atmosphere, and the now-oxygenated blood is returned to the left atrium of the heart through venules and the pulmonary veins. Oxygenated blood is then pumped from the left atrium, through the mitral valve, into the left ventricle and the cycle begins anew.

From this rather simplistic view of the circulatory system, we see that the arterial vasculature can be conveniently divided into four classes of vessels based on size: the conducting vessels like the aorta, the distributing vessels that deliver blood to specific organs, the arterioles, and the capillaries. The structure of the healthy arterial wall differs between vessel classes, reflecting their different locations in the circulatory system, and the different roles they play in the body. The carotid arteries are conducting arteries and thus only this class of vessel is further discussed.

### **1.1.1 The Conducting Vessels**

Conducting vessels are named for their function within the body, namely, conducting blood from the heart to the rest of the body. The aorta and other conducting vessels are generally of larger diameter (approx. 2.5 – 1 cm), are thick walled, and are elastic. These bulk properties, and the underlying microstructure of the conducting vessel wall are optimized for proximity to the heart and the support of large volume flow rates. The conducting artery wall consists of three primary layers, the tunica intima, tunica media, and the tunica adventitia (see Fig. 1.1).

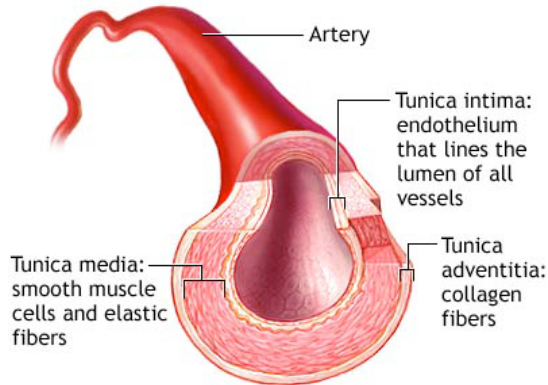


Fig. 1.1 Cross-section of a typical conducting artery showing the intimal, medial, and adventitial layers.

From <http://adam.com>.

The intima is the innermost layer, and comprises a monolayer of biologically active endothelial cells supported by the basal lamina, which consists largely of a mesh of type IV collagen, and the glycoproteins laminin and fibronectin. The endothelium of the intima provides a non-thrombogenic interface between the vessel wall and flowing blood.

Beyond the intima is the media, which is composed primarily of smooth muscle cells (SMCs), elastic connective tissue, and various types of collagen. Fenestrated elastin sheets divide the media into concentric layers of smooth muscle reinforced with elastin and collagen fibrils. The innermost and outermost elastin sheets are known as the inner elastic lamina and the outer elastic lamina, and they separate the media from the intima and adventitia, respectively. The SMCs and collagen fibrils of the media are often oriented helically about the vessel axis with a small pitch such that the dominant mechanical reinforcement is nearly circumferential. Vessels closer to the heart generally have a greater number of elastic lamina than more peripheral vessels, which are more muscular in structure.

The elastic compliance of the conducting vessels, and particularly the aorta, serves to smooth out the pressure wave of the cardiac cycle. When the left ventricle contracts, blood is expelled into the aorta. This sudden rise in aortic pressure, to 100-160 mmHg, causes the vessel to distend radially, acting as a capacitor for blood. After the systolic peak, when no blood is being pushed into systemic circulation by the heart, the compliant aorta relaxes and its elastic potential energy is used to propel blood forward into the vasculature. In this way, systemic flow is maintained during diastole, and the blood flow waveform of the cardiac cycle is smoother than the pump action of the heart. The media is the most mechanically relevant layer in the healthy arterial wall at physiologic load, and is what gives conducting vessels their capacitance.

Outward from the media, beyond the outer elastic lamina, is the tunica adventitia. The adventitia is composed primarily of fibroblasts, ground substance, and bundles of collagen fibers. The collagen fibers are arranged roughly helically with the vessel axis. The average pitch of the helices is typically much greater than that of the medial collagen, although significant directional dispersion is often present (Finlay, McCullough et al. 1995; Gasser, Ogden et al. 2006). The adventitia secures the vessel to perivascular tissue and also contains the *vasa vasorum*, microvasculature that provides circulatory support to the adventitia and outer portion of the media. At low luminal pressures, the collagen fibrils in the adventitia are only partially stretched, and the adventitia is much more compliant than the media. Under a high-pressure load, however, the collagen fibrils are further extended and the adventitia stiffens significantly. Thus, the structural mechanical role of the adventitia is to act as a sheath that prevents overstretching of the vessel wall. There is also nervous tissue in the adventitia, and recent studies show that

this layer plays a role in growth and remodeling and maintenance of vessel tone (Laflamme, Roberge et al. 2006; Maiellaro and Taylor 2007).

### 1.1.2 The Carotid Arteries

The left and right common carotid arteries normally arise from the aortic arch and the brachiocephalic trunk, respectively, and continue without branching until approximately the level of the fourth cervical vertebra. At this level, each common carotid bifurcates into an internal carotid artery that supplies blood to the cerebral circulation, and an external carotid artery that supplies more superficial anatomy of the head and neck (see Fig. 1.2).

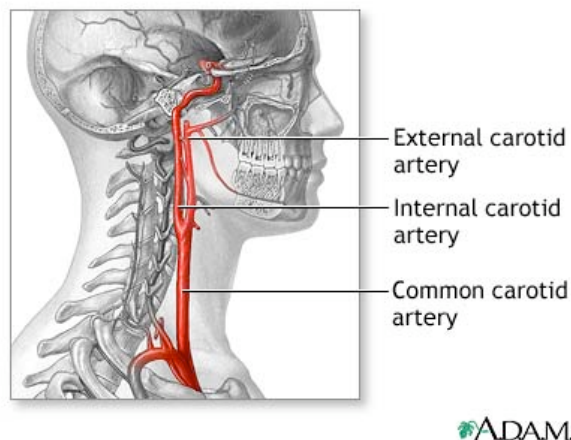


Fig. 1.2 Location of the carotid bifurcation with respect to head and neck anatomy. From <http://adam.com>.

The representative dimensions of the carotid bifurcation are shown in Fig. 1.3, where the cross-section of each branch is approximated to be circular. Note the widening of the internal carotid artery just distal to the bifurcation. This region, known as the carotid sinus, contains baroreceptors that detect and help regulate the systemic blood pressure.

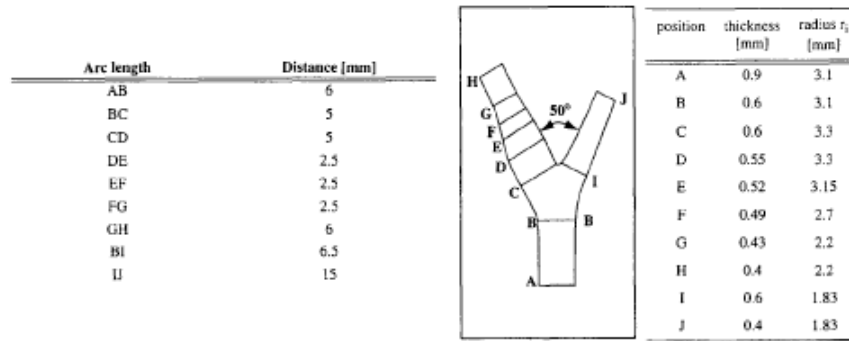


Fig. 1.3 Representative geometry of the human carotid bifurcation, as determined by A. Delfino (Delfino 1996).

For a more comprehensive review of vascular anatomy and physiology, see (Guyton 1974; Guyton 1976; Humphrey 2002).

## 1.2 Atherosclerosis

Atherosclerosis is a slowly progressing disease characterized by the accumulation of material within the artery wall. The disease is typically initiated in adolescence, and is seen with greater frequency with increasing age. Atherosclerosis preferentially affects larger arteries, and its presence has been correlated with local hemodynamic complexity. Specifically, it has been shown that regions of the vessel wall experiencing low and oscillatory wall shear stress are more likely to develop atherosclerotic lesions (Ku, Giddens et al. 1985). Presumably, this is due to shear-dependent alterations in the arrangement and permeability of the endothelial cells at the lumen surface (Dewey, Bussolari et al. 1981; Nerem, Levesque et al. 1981; Conklin, Vito et al. 2007).

Atherosclerosis is recognized pathologically as an ongoing inflammatory response to local endothelial dysfunction, which may be caused by any combination of several

factors. In addition to flow-induced shear stress, some of these factors are local infection, oxidative stress, chronic hypertension, and most notably, elevated low-density lipoprotein (LDL) levels (Ross 1999). At the dysfunctional endothelium, LDL is allowed to pass into the vessel wall, where it is oxidized by reactive oxygen species. The reactive oxygen species are present naturally, and in increased concentrations when the patient is exposed to one or more atherosclerosis risk factors. An inflammatory response to the oxidized LDL is mounted, and monocytes are recruited locally through the expression of various inflammatory mediators.

Low mean or oscillatory wall shear stress tends to coincide with portions of the flow field where particle residence time is significantly elevated, such as areas of flow recirculation or oscillation. Coupled with increased endothelial permeability, locally increased residence time can enhance the mass transport into the vessel wall of both LDL and inflammatory cells at the lesion site (Ku, Giddens et al. 1985). Inside the intima, monocytes are activated to macrophages that phagocytize oxidized LDL; after extensive phagocytic activity the swollen macrophages take on a *foamy* appearance and are termed *foam cells*. It is the accumulation of foam cells, collagen, elastin, fibrin, extracellular cholesterol, and other cellular debris that forms an atheromatous plaque. The initiation and progression of atherosclerosis is strongly influenced by local biochemistry and cellular-level processes, and a comprehensive review may be found in many other works (Richardson 2002; Stoll and Bendszus 2006; Forrester 2007). For the present purpose, it will suffice to describe the structural aspects of the atherosclerotic vessel.

The earliest macro-scale manifestation of atherosclerosis is the presence of fatty streaks, which are caused by the accumulation of lipid-laden macrophages and T-lymphocytes under the intimal endothelium (Libby 2002). At this stage, the atherosclerotic vessel has the mechanical response of the healthy vessel in a passive sense, although there may be a local decrease in nitric oxide (a vasodilator) production affecting its active response.

As atherosclerosis progresses, the arterial wall adopts a structure quite different from that of the healthy artery, and the mechanical response reflects this difference. Because atherosclerosis is a slowly progressing disease and its severity often correlates with advancing age, it should be noted that the aging intima thickens and becomes stiffer naturally (Holzapfel, Sommer et al. 2005). Thus, in a diseased artery, even at locations without an acute plaque lesion, the intima can play a significant role in the mechanical response of the artery. This is in contrast to the healthy young intima, which does not have a significant impact on the structural mechanics of the arterial wall.

Earlier in the progression of a plaque, as foam cells accumulate in the intima, the vessel wall remodels and expands outward to preserve the patent lumen area (Glagov, Weisenberg et al. 1987). Thus, the outer vessel wall may adopt a swollen appearance focally around the plaque and little or no luminal narrowing is present on an angiographic study. As the inflammatory response continues, SMCs are signaled to proliferate and are recruited from the media to the intima directly overlying the lipid and macrophage-rich plaque. These smooth muscle cells, and other fibrous components of the actively remodeling extracellular matrix constitute the *fibrous cap* of the plaque. It is the rupture or ulceration of this fibrous cap and subsequent exposure of highly thrombogenic plaque



contents to flowing blood that can cause acute thromboembolic events like stroke and myocardial infarction (Virmani, Burke et al. 2006). A coarse view of the early atherosclerotic vessel would recognize the intima, fibrous cap, lipid and macrophage-rich plaque core, media, and the adventitia as distinct structural components with individual mechanical behavior. Of course, at the histological scale, each one of these components has a highly heterogeneous microstructure of its own.

Not every plaque ulceration or rupture will cause a thrombo-embolic event, and the disruption may eventually “heal” with the reformation of the fibrous cap. A series of ruptures and repairs can eventually lead to a large plaque that grows inward into the vessel lumen. Plaques with such a history are often the cause of high degree arterial stenosis, where the patent lumen diameter has been reduced by 50% or more (Mann and Davies 1999). These and other older plaques have a more irregular appearance and structure. The fibrous cap is of non-uniform thickness, and the lipid-rich plaque core has a very irregular shape and may not be a single continuous body. Additionally, bulk calcification and smaller calcium hydroxyapatite deposits are often present within surrounding fibrous plaque (regions of smooth muscle cells, collagen, and macrophages) and in the plaque core. The mechanical characteristics of the later stage atherosclerotic vessel are determined from the size, shape, strength and relative locations of the intima/fibrous cap, the remodeled media, the lipid-rich plaque core, fibrous plaque, calcification, and the adventitia.

### **1.3 Carotid Plaque Stability, Rupture, and Stroke**

The atherosclerotic artery wall is very different from the healthy artery wall in both composition and mechanical response. In addition to the compositional and geometric complexities of an atherosclerotic lesion, there are numerous ongoing biochemical processes that can affect the mechanics of the lesion tissues. The cells and materials present in atherosclerotic plaques play regulatory roles in these biochemical processes in addition to their structural roles, and thus the full mechanical characterization of a lesion is time dependent.

During the course of a plaque's evolution there are both stabilizing and destabilizing cellular processes at work. Matrix metalloproteinases (MMPs), most notably MMP-8 and MMP-9, are expressed by macrophages in the lesion, and are capable of degrading structural proteins of the extracellular matrix such as collagen and elastin. MMPs 8 and 9 were found in higher levels in carotid endarterectomy specimens from patients with recent (< 4 weeks) cerebrovascular events when compared to specimens from asymptomatic patients (Loftus, Naylor et al. 2000; Molloy, Thompson et al. 2004). Macrophages are stimulated to produce MMP-9 by activated T-lymphocytes, and the population of these inflammatory cells in plaque tissues seems to be an important determination of the stability of the lesion and symptom status of the patient. Jander et al. showed that T-cells and macrophages were found in greater abundance in endarterectomy specimens from symptomatic patients in comparison to those from asymptomatic patients (Jander, Sitzer et al. 1998). More direct evidence of the destabilizing activity of inflammatory cells comes from observations of increased

numbers of macrophages in the fibrous caps of ruptured plaques relative to those without rupture (Milei, Parodi et al. 1996; Carr, Farb et al. 1997; Virmani, Burke et al. 2006).

In some plaques, an imbalance between the proteolytic activity of MMPs and the stabilizing effects of anti-inflammatory cytokines and SMC migration will proceed to the extent that local tissue strength is critically compromised. When this happens, the tissue fails and intraplaque hemorrhage from the vasa vasorum or plaque rupture may occur (Ross 1999). Although intraplaque hemorrhage is not a thromboembolic event, its presence has been shown to correlate strongly with plaque rupture (Carr, Farb et al. 1996) and less strongly with patient symptoms (Gao, Chen et al. 2007), indicating its likely role in enhancing the inflammation and matrix degradation already in effect.

Plaque rupture exposes flowing blood to thrombogenic sub-endothelial tissues and plaque components, which can induce thrombus formation and/or spill into the circulation. Macrophages within the lesion are rich in tissue factor, a critical protein in the blood coagulation cascade, and activated T-lymphocytes stimulate upregulation of tissue factor production (Lafont 2003). Thus, the inflammatory process not only affects rupture potential, but also influences mechanisms subsequent to rupture. The size of thrombus formed, whether or not it remains at the vessel wall, and the volume and thrombogenicity of material shed from the plaque will determine the extent to which blood supply from the carotid distribution is limited in distal tissues. Plaque rupture may result in a range of symptoms extending from a relatively minor transient ischemic attack to a massive ischemic stroke, or rupture may even be fully asymptomatic (Qiao, Farber et al. 2008). The effects of plaque rupture are determined not only by the extent of thromboembolism, but also by the availability of collateral blood flow to distal tissues.

Stroke is the third leading cause of death in the United States, behind coronary heart disease and cancer; stroke is also the country's leading cause of long-term disability. Approximately 500,000 Americans will have a first stroke in a given year, and another 200,000 will have a recurrent stroke, with nearly 30% proving fatal. Roughly 87% of all strokes result from brain tissue ischemia, with the balance being caused by hemorrhagic conditions (Rosamond, Flegal et al. 2007). Thromboembolism from carotid disease is a major cause of ischemic stroke, and rupture or ulceration is the predominant lesion morphology associated with symptomatic carotid disease (Redgrave, Lovett et al. 2006).

These daunting statistics, and the fact that that the world's number one killer, coronary heart disease, shares a similar plaque-rupture mechanism in its acute form, have stimulated an intense search for the appropriate characterization of the plaque that is "vulnerable" to rupture. Detailed understanding of the mechanism(s) of plaque rupture and accurate *in vivo* assessment of a plaque's rupture potential could help clinicians better stratify patients into the optimal treatment plans, thereby reducing the morbidity and mortality of advanced carotid disease. Additionally, although carotid plaques and coronary plaques may not necessarily progress and rupture in precisely the same manner, it seems reasonable that advances in our understanding of carotid plaque rupture could be of benefit in the diagnosis, characterization, and treatment of coronary heart disease. Despite our significant advances in understanding atherosclerosis progression and structural and inflammatory correlates to plaque rupture, the precise mechanism of plaque rupture remains elusive. Furthermore, our ability to assess the vulnerability, and thus danger, of any particular lesion is wanting. This is in no small part due to the multifactorial nature of plaque vulnerability and rupture.

It is clear that a chronic or acute inflammation plays a significant role in the progression and stability of a lesion. Rupture, however, is a mechanical phenomenon related to the balance of stress and tissue strength, and so the presence of inflammation does not solely determine a plaque's rupture potential. The stress field within the diseased arterial wall is largely determined by the composition, size, and shape of the artery and plaque components, and so it is plausible that certain morphologies are associated with rupture vulnerability. Indeed, the hunt for an appropriate and clinically useful measure of plaque vulnerability and rupture potential has yielded contributions from the perspectives of several diverse fields, including cellular biology, histology, medical imaging, and biomechanics.

## 1.4 Plaque Characterization

Currently, percent luminal stenosis is the plaque feature considered most strongly by clinicians when deciding the appropriate treatment for a carotid disease patient. The percent luminal stenosis is calculated as

$$\text{Percent Luminal Stenosis} = \left( 1 - \frac{\text{minimum luminal diameter}}{\text{post - stenotic luminal diameter}} \right) \times 100\% \quad (1.1)$$

with lumen diameter measured angiographically. To consider percent stenosis as the primary predictor of complications from carotid atherosclerosis seems reasonable, and agrees well with intuition that a greater reduction in lumen cross-sectional area implies a greater plaque burden and thus more severe disease. Percent stenosis as the dominant feature for clinical plaque characterization is supported or rather, suggested, by the

outcomes of the NASCET and the ECST trials that examined the efficacy of carotid endarterectomy in preventing stroke. Carotid endarterectomy is the surgical removal of atheromatous material from the carotid artery. It was shown to reduce the incidence of stroke by 21.2% for symptomatic patients with luminal stenosis greater than 70%, when compared to treatment with best medical therapy. Current multidisciplinary consensus statements from The American Heart Association state that endarterectomy shows benefit for symptomatic patients with severe stenosis ( $> 70\%$ ) and a surgical risk less than 6%, and for asymptomatic patients with stenosis greater than 60% and a surgical risk less than 3% (Moore, Barnett et al. 1995; Morey 1998).

While stratifying patients into surgical or medical therapy based on percent stenosis has shown a clear benefit (Moore, Barnett et al. 1995), the classification of carotid lesions as vulnerable to rupture or not based upon lumen reduction is inappropriate. Many advanced plaques that will progress to rupture cause stenosis below 50% due to positive vessel remodeling, first introduced by Glagov et al. for coronary disease (Glagov, Weisenberg et al. 1987). Thus, a number of patients with angiographically innocuous disease will not receive effective surgical treatment. Conversely, some lesions causing severe stenosis or even complete vessel occlusion will never cause symptoms or experience rupture, and a number of patients will undergo unnecessary surgery. Complications as a result of carotid endarterectomy are rare, but potentially serious and life threatening; it is estimated that the risk of stroke or death during or immediately following endarterectomy is between 3% and 5% (Bond, Rerkasem et al. 2003).

A more suitable way to assess the rupture risk of a plaque is to consider the morphological and compositional characteristics of the lesion. Stary et al. used such characteristics to construct the American Heart Association scheme for atherosclerosis classification, for initial stages of the disease to advanced complex plaque lesions, with no specific focus on rupture-prone plaques (Stary, Chandler et al. 1994; Stary, Chandler et al. 1995). Several groups have used *post mortem* observations and histological studies of plaque specimens to extend this classification and define characteristics of lesions that are likely to cause symptoms or rupture. The terminology is vast and often confusing, and we refer to the paper by Naghavi et al. for the definition of a vulnerable plaque (Naghavi, Libby et al. 2003). Their definition is broad and encompasses all “thrombosis-prone plaques and plaques with a high probability of undergoing rapid progression...,” not strictly those that are prone to rupture. Table 1 lists the major and minor criteria identified by Naghavi et al. to be met for any particular plaque to be classified as vulnerable. The criteria were established through post-mortem identification of culprit plaques, that is, those responsible for coronary occlusion and subsequent death. Much of what is known about plaque vulnerability has been established through studies of coronary disease, and the knowledge garnered has been generally applied to understanding carotid disease as well.

---

Major criteria

- Active inflammation (monocyte/macrophage and sometimes T-cell infiltration)
- Thin cap with large lipid core
- Endothelial denudation with superficial platelet aggregation
- Fissured plaque
- Stenosis >90%

Minor criteria

- Superficial calcified nodule
  - Glistening yellow
  - Intraplaque hemorrhage
  - Endothelial dysfunction
  - Outward (positive) remodeling
- 

Table 1.1 Major and minor criteria to be met for a plaque to be considered vulnerable, according to Naghavi et al.

Of the seven vulnerable plaque types presented in Naghavi et al.'s paper, one stands out as especially rupture-prone. The thin-cap fibroatheroma, a plaque with a large necrotic lipid core and thin, macrophage-infiltrated fibrous cap has been recognized as a common precursor to plaque rupture (Virmani, Burke et al. 2002; Virmani, Burke et al. 2003). A schematic of the thin-cap fibroatheroma is shown in Fig. 1.4.

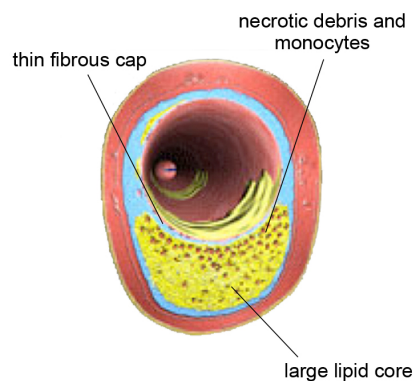


Fig. 1.4 Illustration of representative thin-cap fibroatheroma. From <http://texasheart.org/Research>



In addition to the large necrotic lipid core, the thin-cap fibroatheroma often has a paucity of smooth muscle cells in the fibrous cap, with 95% of ruptured caps being 65  $\mu\text{m}$  or thinner (Virmani, Burke et al. 2006). In the following, the term “vulnerable plaque” will refer specifically to the rupture-prone thin-cap fibroatheroma unless otherwise stated.

Although these descriptions are based on observations of culprit coronary lesions, similar trends are seen in symptomatic carotid plaques. Bassiouny et al. note that the necrotic lipid cores of symptomatic or disrupted carotid plaques are twice as close to the lumen as those of asymptomatic plaques. They additionally state that the macrophage content of symptomatic plaque caps is three times higher than in asymptomatic lesions. No difference between symptomatic and asymptomatic lesions could be found with regard to percent stenosis, total lipid core volume, total calcification, or location of the calcification in respect to the lumen surface (Bassiouny, Sakaguchi et al. 1997). Virmani et al. examined carotid endarterectomy specimens that experienced rupture and showed that the mean ruptured fibrous cap thickness was 3 times larger than in ruptured coronary plaques ( $72 \pm 15 \mu\text{m}$  vs.  $23 \pm 17 \mu\text{m}$ ), and that carotid plaques contained less macrophage burden in both their caps and lipid cores (Virmani, Ladich et al. 2006). Thus, themes may be shared in carotid and coronary plaque rupture, but absolute histological quantifications may be significantly different.

## **1.5 The Role of Medical Imaging in Plaque Characterization**

Histological analysis and post-mortem observation have provided us with a set of morphological and physiological features that are commonly found in culprit lesions, that

is, lesions that have produced symptoms or have ruptured. Armed with this information, medical imaging has the potential to detect vulnerable lesions before they rupture, thereby helping to prevent dangerous sequelae of plaque instability and rupture. Several medical imaging modalities show promise in the identification of vulnerable plaques.

### **1.5.1 Magnetic Resonance Imaging**

Magnetic resonance imaging (MRI) forms images by reconstructing a map of the magnetization vectors of the hydrogen nuclei in the water of body tissues. The powerful magnet of the MRI scanner causes a small but significant net alignment of magnetization within the tissue in the direction of the scanner's main magnetic field. The tissue magnetization precesses about the direction of the scanner's main magnetic field at a frequency related to local field strength, generating a small magnetic field of its own which is detected by receiver coils for imaging purposes. Through the application of radiofrequency pulses to the tissue, and the construction of spatial gradients in the magnetic field bathing the tissue, the magnitude and precessional frequency of tissue magnetization can be manipulated. Sequences of radiofrequency pulses and magnetic field gradients of specific design are used to encode the spatial location of tissue in its precessing magnetization. The timings and modulation of the radiofrequency pulses and magnetic field gradients can be further specified so that the signal produced by the precessing magnetization will reveal information about the local composition and chemical environment. Because encoding is performed on the precessional frequency, the signal detected by the receiver coils is related to the magnetization map by a Fourier relationship. Encoding can be such that the detected signal conveys information about

2D tissue slices or 3D volumes, with the spatial extent and orientation determined by the pulses and gradients used. The continuous signal is discretely sampled in time and inverse Fourier transformed to reveal a collection of discrete pixels (2D) or voxels (3D) that correspond to small segments of the tissue imaged.

The MRI techniques most commonly used to image the diseased vessel wall are based on 2D spin-echo sequences similar to those used to image other soft tissues in the body. One important modification to these sequences is the use of additional radiofrequency pulses, termed double inversion preparation, which eliminates signal from tissue outside of the slice of interest. The signal strength of intraluminal blood in the slice of interest reflects the magnetization state that is transported into the slice by blood flowing from outside the slice of interest. Double inversion preparation is designed such that the magnetization of blood outside the slice of interest reaches a null condition, and these images therefore have a black lumen allowing for greater discrimination of the vessel wall. This form of vessel wall imaging is referred to as “black blood” imaging. Fat saturation preparation is also commonly used to suppress signal from adipose tissue adjacent to the vessel wall. Spin echo sequences can be created with the usual contrast weightings employed in routine clinical imaging, referred to as T1-, T2- or proton density weighting; intermediate contrast weightings have also been used to study the vessel wall. Typical pixel dimensions in black-blood MRI are 0.5mm x 0.5mm in the image plane, and a 2mm slice thickness over which signal is effectively averaged.

Several groups have used MRI techniques to identify features of the diseased wall of the carotid artery. STIR sequences, useful for nulling signal from tissue based on T1 relaxation, have been used to quantify the relative thicknesses of the fibrous cap and lipid

core in patients prior to endarterectomy. The thickness ratio of these features determined from *in vivo* imaging compared well to the ratio obtained from histological analysis of the endarterectomy specimens (Trivedi, JM et al. 2004). Studies on endarterectomy specimens have shown that *ex vivo* multi-contrast MRI imaging, using T1-, T2-, and intermediate-weighting was able to accurately identify the lipid-rich plaque core, intraplaque hemorrhage, and calcification as verified with histology (Shinnar, Fallon et al. 1999). Similar multi-contrast MRI/histology studies using *in vivo* imaging, with the addition of a 3D time-of-flight angiographic sequence, have shown the strength of MRI identification of all major plaque features, including characterization of the fibrous cap as thick, thin, or ruptured (Hatsukami, Ross et al. 2000; Saam, Cai et al. 2006).

Progress has also been made in imaging the inflammatory state of the carotid lesion, exploiting the enhanced uptake of gadolinium contrast agents in the inflamed vessel wall with extensive neovascularization and pathologically heightened permeability (Aoki, Aoki et al. 1999; Yuan, Kerwin et al. 2002; Kerwin, O'Brien et al. 2006). More specific imaging of inflammatory status is becoming possible with the use of small and ultra-small paramagnetic iron oxides (SPIO, USPIO). SPIO and USPIO particles are phagocytized by macrophages when introduced into the circulation, causing susceptibility artifacts in T2\*-weighted MR images in areas of high macrophage density. Signal dropout has been seen in actively inflamed plaques within a 1 to 3 day window after injection, and histological analysis has confirmed that regions with pronounced dropout correspond to significantly elevated macrophage populations (Kooi, Cappendijk et al. 2003; Lee, Kang et al. 2006).

### 1.5.2 Computed Tomography

Computed tomography (CT) forms images of structures internal to the body by making several linear projection radiographs of the same tissue at different angles and then combining their information. Each linear radiograph measures the line integral of x-ray attenuation through the body along the projection axis, and so contains information about x-ray absorption inside the body. By obtaining enough projection radiographs and applying the Fourier slice theorem, it is possible to construct the 2D Fourier transform of a planar slice through the body. 2D inverse Fourier transformation can then provide the spatial distribution of x-ray attenuation over that slice (Kak and Slaney 1988). In practice however, using a limited number of projections, the frequency-domain data would be sparse at higher spatial frequencies, requiring laborious and error-prone interpolation. Furthermore, two-dimensional Fourier transformation is computationally expensive compared to other methods. The reconstruction algorithm most heavily used in computed tomography, filtered backprojection, relies on Radon transformation.

Each projection is the Radon transform of the original planar distribution of x-ray attenuation in the tissue slice. The analytic inversion of the Radon transform amounts to a filtering operation on the original projection, followed by a back-projection onto the spatial plane. The filtering can be accomplished in the spatial domain or in the spatial-frequency domain. Filtering in the spatial domain requires an expensive convolution operation, while filtering in the frequency domain requires a 1D Fourier transformation of the projection into the frequency domain, a multiplication by the response function of the filter, and an inverse Fourier transformation back into the spatial domain. As it is faster and more robust, the frequency-domain filtering is typically used. After each

projection is transformed, filtered, and inverse transformed, the filtered projections are back-projected along their original projection axes across the spatial domain and summed. The resulting summation is a reconstructed image of the 2D distribution of x-ray attenuation in the slice of tissue imaged.

Computed Tomography Angiography (CTA) is a robust method for vascular imaging with uniform signal intensity in the flow lumen. Compared to MRI techniques, CTA can achieve large volume coverage in relatively short acquisitions (Dammert, Krings et al. 2004; Lell, Anders et al. 2006). Images are acquired following the intravenous injection of a contrast agent which opacifies intraluminal blood, providing high contrast against the vessel wall. When the contrast agent is within the vascular region of interest, x-ray transmission data is acquired on a series of thin slices covering the region. The data from these slices can be reconstructed using interpolation across slices to form a three-dimensional volume of data. Typical resolution in these studies is of the order of 0.4 mm along each axis and the total acquisition can be performed in under 10s. The ability to uniquely identify different plaque materials in a CTA study depends on the relative x-ray attenuation of each component. In this regard, calcifications within the plaque have high absorption and their presence and distribution can be readily determined. It is more difficult to discriminate between other components of an atheromatous plaque due to their similar x-ray attenuations, but progress has been made in using this modality to differentiate the necrotic lipid core from fibrous components of the plaque (de Weert, Ouhlous et al. 2006; de Weert, de Monye et al. 2008; Wintermark, Jawadi et al. 2008).

### 1.5.3 Ultrasound

B-mode ultrasound (US) imaging builds up a grey scale image of tissue interfaces by transmitting ultrasound pulses into the body and detecting the time of return of echoes reflected off those interfaces. At the most common transducer frequencies, in-plane spatial resolution in US images is of the order of 0.5mm. US is often the preferred modality for carotid artery screening examinations, owing to its portability and affordability relative to MR and CT imaging. US is also preferred when the patient has contraindications to MR (such as metal or electrical implants, claustrophobia, or impaired renal function) or CT (such as contrast agent allergy). In addition to B-mode imaging, Doppler US is used to measure blood flow in the artery and provide physiological information. With Doppler US, an insonation volume is placed in a desired location, for example, in the center of the vessel of interest. The full spectrum of flow velocities within the insonation volume can be determined with a temporal resolution on the order of 10ms. While the combination of B-mode and Doppler US has been a primary tool for the evaluation of carotid stenosis (Grant, Duerinckx et al. 2000; Schulte-Altdorneburg, Droste et al. 2002), and lesion echogenicity has been correlated to symptom development (Nagano, Yamagami et al. 2008), US is not capable of reliably resolving features of the carotid plaque (Droste, Karl et al. 1997). Contrast-enhanced US has, however, enjoyed recent progress in the identification of neovascularization in carotid plaques, which is thought to be related to lesion vulnerability (Coli, Magnoni et al. 2008; Giannoni and Vicenzini 2009).

Intravascular ultrasound (IVUS) places the US transducer on a catheter so that data can be collected from very near the luminal surface. Such proximity to the vessel wall allows use of a greater ultrasonic frequency than conventional ultrasound permits (between 20 – 45 MHz vs. ~10 MHz), as penetration depth is of less concern for intravascular applications. The increased frequency allows imaging to be performed with high spatial resolution, on the order of ~150  $\mu\text{m}$  in-plane. Catheter pullback allows data to be acquired in the longitudinal direction as well, and volumetric imaging can be performed, although 3D reconstruction can be limited by catheter placement, vessel curvature, and pullback inconsistency. Several studies have been made to compare *in vivo* and *ex vivo* plaque characterization via IVUS to histological data, with results being mixed (Nair, Kuban et al. 2002; Granada, Wallace-Bradley et al. 2007). Most applications of IVUS have been in the coronary arteries, the study of which often necessitates catheterization anyway, although investigators have recently explored the role of IVUS in carotid plaque analysis (Diethrich, Pauliina Margolis et al. 2007; Joan, Moya et al. 2009).

## **1.6 A More Comprehensive Assessment of Vulnerability and Rupture Risk**

Medical imaging is undergoing a period of rapid growth in atherosclerosis detection and characterization. Non-invasive (save for a possible contrast injection) modalities like MRI and CTA can provide data regarding plaque morphology and are capable, to varying extents, of identifying the major features of vulnerable plaques. Progress is additionally being made with respect to the imaging of physiologic processes



indicative of active inflammation. Invasive modalities like IVUS and Optical Coherence Tomography (OCT, an optical analogue to IVUS) also show promise and offer greater spatial resolution and the ability to image within the coronary vessels. With such technological advancement, we will no doubt enjoy an ever-increasing capability to detect atherosclerotic lesions with features consistent with vulnerability.

We must bear in mind three points, however. First, vulnerability does not engender rupture any more than a match makes fire. Like the match that must be struck to produce a flame, a vulnerable plaque must be acted upon for rupture to occur. Rupture is a mechanical process in which material stress exceeds tissue strength. Thus, a vulnerable plaque inadequately challenged may remain intact indefinitely, or eventually remodel to a more stable form. Second, rupture need not occur only when a plaque fulfills the histologically determined criteria for vulnerability. The geometry, loading, composition and material properties of any structural system have great influence on the stress field experienced, and thus a plaque which appears non-vulnerable may actually be under a stress large enough to induce rupture. Lastly, atherosclerotic plaques generally have a complex morphology, and it may be more difficult to judge vulnerability from imaging data in three dimensions. The local quantification of fibrous cap thickness or lipid core volume should be viewed in the context of the full plaque structure. This could make an image-based rupture-risk or vulnerability assessment more complicated and less reliable.

In light of these points, it is clear that mechanical analysis has the potential to augment image-based assessments of plaque vulnerability. Coupled together, it may be possible to make a rupture-risk assessment that takes into account both the plaque's

vulnerability and the extent to which it is challenged by local mechanical forces. To this end, many mechanical studies of model atherosclerotic lesions have been made to elucidate the nature of the stress field within a diseased artery. These efforts have shed light on the relative influence of various plaque components and lesion features on the stress field within the diseased vessel wall. While the very simplest of these analyses have made analytical solutions for the stress field, the overwhelming majority of studies have relied on numerical methods, most notably the finite element methods (FEM).

## **1.7 Literature Review - FEM Studies of Atherosclerotic Vessels**

### **1.7.1 Idealized Diseased Vessels**

Because of the great variety of plaque component shapes and distributions, several groups have constructed idealized models of atherosclerotic vessels. In this way, geometric characterization of the model is trivial, and stresses and strains are easily related to features such as fibrous cap thickness, lipid pool volume, calcification/lipid volume ratio, and lumen eccentricity. Loree et al. constructed a series of 2D FEM models of atherosclerotic coronary arteries to investigate the effects of fibrous cap thickness and stenosis severity on circumferential stress, which is thought to be directly related to plaque rupture risk (Richardson, Davies et al. 1989; Loree, Kamm et al. 1992). This classic 2D study was of a transverse cross-section of an artery with an eccentric fibrous plaque burden and a crescent-shaped lipid pool extending 140° concentric with the lumen. Ten similar geometries of varying fibrous cap thickness and stenosis severity were analyzed under systolic pressure loads. Increasing the lipid pool thickness at constant stenosis severity reduced fibrous cap thickness, resulting in a significant increase

in cap circumferential stress. No significant changes in peak circumferential stress were observed through variation of the degree of stenosis at a constant lipid pool thickness. Thus, the study showed that fibrous cap thickness, and not stenosis severity, was likely the dominant factor influencing plaque rupture risk, as fibrous plaque must experience mechanical failure at some level of stress.

The use of a plane strain FEM model by Loree et al. was justified by the assumption that the plaque structures of interest would extend nearly a vessel diameter along the vessel axis. Such an assumption is reasonable for many analyses and is common in the literature, but careful attention must also be paid to the longitudinal distribution of stress in the diseased vessel. Imoto et al. used FEM to study the longitudinal distribution of stress in representative plaque/artery structures (Imoto, Hiro et al. 2005). The authors noted stress concentrations at the ‘shoulders’ of the plaques, the longitudinal positions where the plaque began and ended. This important result cannot be seen in a transverse 2D model. Peak stresses were higher, assuming constant thickness plaques, for geometries with positive remodeling as opposed to those with stenotic remodeling. For the models that included lipid pools, the cap stresses increased dramatically with decreasing cap thickness, in agreement with the conclusions of Loree et al.. Referencing the literature, the study assumed a fibrous plaque yield strength of 300 kPa, and noted that this stress was exceeded when the fibrous cap over a lipid pool was thinner than 60 to 100  $\mu\text{m}$ , depending on vessel radius. This finding agrees well with critical cap thicknesses observed histologically (Virmani, Burke et al. 2006).

Tang et al. investigated the effects of lipid pool size and cap thickness on the stress distributions in fully 3-dimensional models of vessels with 100% eccentric lesions

using fluid-structure interaction (FSI) to load the diseased artery wall (Tang, Yang et al. 2004). The model with a smaller lipid pool and thicker cap than in the baseline model experienced a peak stress reduction of about 20%. The same geometry without a lipid pool demonstrated a peak stress reduction of 33%. When the size of the lipid pool was greater than that of the baseline model, the stress peak increased by about 30%. Li et al. (Li, Howarth et al. 2006) further investigated the deformation of an idealized dome-shaped, 100% eccentric plaque subjected to carotid artery-like flow conditions. In their longitudinal cross-section model, fibrous cap thickness was varied between 0.1 mm and 2 mm, and 90 different stenosis severities between 10% and 90% were simulated. Due to the inlet pressure, and impinging flow, maximum deformation of the plaque was seen on the proximal edge of the plaque about midway from shoulder to peak stenosis. Maximum first principle stress was highest at points surrounding maximum deformation, indicating a bending mode of deformation in the cap. The parameter study showed that for stenosis of 30% to 70%, plaque cap thickness was a critical determinant of rupture potential, using the often cited 300 kPa possible rupture stress (Lendon, Davies et al. 1991). Although their model was very simple, the authors noted that the stress distributions calculated correspond well with the proximal-surface ulcerations seen histologically in such lesions.

### **1.7.2 Studies on Calcification**

The work of Imoto et al. (Imoto, Hiro et al. 2005), and studies by several other groups, show that calcifications within the fibrous cap attenuate cap stress levels and therefore make rupture less likely. Additionally, the study by Huang et al. (Huang,

Virmani et al. 2001) showed that there was no significant change in maximum principle stress when calcifications were replaced by fibrous plaque in the 2D FEM models of 20 resected coronary arteries. This was in contrast to the sometimes-severe decrease in stress when a lipid pool was replaced with fibrous plaque in the models. In these studies the calcifications considered were large, on the order of the cap thickness or bigger. Recently, Vengrenyuk hypothesized that smaller calcifications can actually induce fibrous cap rupture through a debonding process caused by significantly elevated interfacial stresses at the surface of the calcified inclusion (Vengrenyuk, Carlier et al. 2006). The theoretical solution presented in the paper was not specific to a vascular model, and was based on a single rigid spherical inclusion eccentrically located in a thin elastic layer (2-10 inclusion diameters) under uniaxial tension. Results suggested that if an inclusion is present in a thin fibrous cap near the lipid-pool boundary, then local stresses could increase by nearly a factor of 2. The authors noted that this might explain the paradox that although plaque rupture is commonly seen at regions where high stress was predicted, the rupture point is not always at the point of maximum stress. Microcalcifications are very small, on the order of 10  $\mu\text{m}$ , and are not detected by clinical imaging. For this reason, mathematical models of atherosclerotic plaque had not previously considered their effects.

### **1.7.3 2D Patient-Specific FEM Studies**

As many 2D studies of idealized plaques have shown, the stress and strain fields in the diseased artery wall are strongly influenced by the shape and size of the lumen and other features like lipid pools, calcifications or fibrous plaque burden. Although these

models have yielded much useful information about the mechanics of the atherosclerotic vessel, idealized geometries impose limitations on their utility. Studies on idealized diseased vessels cannot be used to investigate the mechanics of a real lesion, whose evolution *in vivo* may be known. These studies are also not capable of relating the mechanical environment to biological factors like histologically determined inflammatory state or composition. It is therefore of great interest to study the mechanics of the atherosclerotic vessel on a patient-specific basis, using geometries and compositions determined from histological analysis, or *in-* or *ex vivo* imaging methods.

Due to a lack of suitable non-invasive imaging techniques, the earliest patient-specific studies of atherosclerotic lesion mechanics used histological information to construct the finite element model. The possibility for specimen distortion and damage made this approach challenging for discerning the true *in vivo* state of the diseased vessel. Additionally, histological analysis requires a very thin slice of the tissue to be used, and thus these models were restricted to 2D analyses that invariably assumed a plane-strain state of stress. While the plane-strain assumption is likely admissible for certain lesions, other lesions involving significant longitudinal variation in composition, loading, or boundary conditions require a fully 3D analysis.

Cheng et al. investigated their hypothesis that plaque rupture occurs at sites of elevated circumferential stress by performing FEM analyses of 24 coronary lesions (Cheng, Loree et al. 1993). Twelve ruptured lesions from patients who died from coronary thrombosis, and twelve unruptured lesions from patients without thrombosis were modeled. Ruptured plaques were reconstructed into their probable pre-rupture states. The study found that 12 out of 12 ruptured lesions had a combined 31 regions of

circumferential stress exceeding 300 kPa, while only one stable lesion demonstrated one area of such elevated stress. Furthermore, the authors found that 7 out of 12 ruptured lesions ruptured at the location of peak stress, and 10 out of twelve ruptured at regions where stress exceeded 300 kPa. The average calculated peak stress in ruptured lesions was significantly almost 2.8 times higher than in the stable control lesions. These results indicated that elevated circumferential stress might indeed contribute to plaque rupture in the coronary arteries.

Patel et al. also employed FEM models built from histological data (Patel, Kaazempur-Mofrad et al. 2003). The authors investigated the correlation between various mechanical descriptors and histological findings for unruptured plaques freshly harvested at carotid endarterectomy. The transverse slices of diseased vessel were cut radially so that they could assume their macroscopically stress-free state. Histological staining for collagen, smooth muscle cells, lipids, and macrophages allowed delineation between arterial wall tissue, fibrous plaque, calcification, and lipid pool. The histologically determined segmentation of each component was used to construct a finite element mesh of the artery in the stress-free state. Thermally contracting truss elements were used to rejoin the cut ends of the unstressed vessel wall, and thus residual stresses were approximated for the diseased vessel models. After the thermal load was applied to rejoin the cut ends of the section, the luminal surfaces of the diseased vessels were loaded with patient-specific diastolic and systolic pressures, as measured prior to surgery. von Mises stress, circumferential stress, and cyclic strain were calculated for each specimen. Significant negative correlations were found for both collagen and macrophage content and the mechanical descriptors at the luminal surface averaged over 15° circumferential

sectors. No significant correlation could be made for lipid or smooth muscle cell content. The most significant correlations were made with respect to cyclic strain, indicating that this descriptor should not be overlooked when trying to establish rupture risk, as it is may be indicative of an active, remodeling plaque.

Other studies, such as that by Versluis et al. (Versluis, Bank et al. 2006), have investigated the cyclic straining of the tissue of a plaque lesion, and its implications on fatigue modes of failure. The vessel modeled was similar to the classic 2D model of Loree et al. A crack propagation algorithm using a modified Paris relation was employed to determine the progressive fracture in the lesion based on evolving stress fields. While there are still many uncertainties in the fracture mechanics of fibrous plaque tissues, the study yielded several interesting results. Cracks were seen to propagate nearly radially from the initiation point, a point of peak stress, so initial stress distributions may be suitable for prediction of a fracture path. Also, reduction of heart rate, mean and pulse pressure, and a reduction in stiffness disparity between plaque components were shown to increase time to rupture in the evolution models.

Accurate soft tissue discrimination and no need for tissue handling and preparation have prompted several groups to use MRI data to construct patient-specific FEM simulations of the atherosclerotic vessel. Li et al. used multi-contrast MRI to image diseased carotid arteries in 5 patients, and constructed 2D FEM models based on the axially acquired images to study plaque rupture (Li, Howarth et al. 2006). Of the five plaques studied, two were ruptured as verified by MRI and histology, and three were intact. FEM meshes for the ruptured plaques represented their probable pre-rupture states. The models of unruptured plaques predicted an average maximum von Mises



stress of 226.9 kPa, whereas the models of ruptured plaques showed an average maximum stress roughly three times greater. The study's use of actual plaque morphologies from *in vivo* MRI effectively introduced a new method by which plaque mechanics could be studied.

The same group extended their work by modeling the carotid plaques of 30 patients, 15 of whom had recently experienced a transient ischemic attack ipsilateral to their carotid disease (Li, Howarth et al. 2007). The remaining 15 patients were asymptomatic. FEM mesh generation and analysis was performed independently from image acquisition and segmentation to avoid biasing of results. The symptomatic group showed a significantly higher maximal effective stress than the asymptomatic group,  $508.2 \pm 193.1$  vs  $269.6 \pm 107.9$  kPa (95% confidence interval of the difference was  $121.7 - 355.6$  kPa,  $P = .004$ ). Similarly, Tang et al. used *ex vivo* MRI as the basis for FEM models of 2D transverse cross-sections of 11 diseased coronary arteries (Tang, Yang et al. 2004). The plaque specimens were classified by pathology on a 0 to 5 scale of rupture vulnerability, and a correlation between the classification and maximum principle stress was investigated. The data suggested a significant correlation between maximum principle stress and vulnerability, but the authors noted that a more comprehensive and large-scale patient study was needed to verify the patterns observed. The results of these studies suggest that stratifying carotid disease patients into risk groups based on careful biomechanical analysis may be of clinical utility.

Citing Lovett and Rothwell's observation that carotid plaques were more likely to ulcerate proximal to the site of maximal stenosis (Lovett and Rothwell 2003), Kock et al. used *in vivo* MRI and FEM modeling to investigate the longitudinal stress distributions in

two patients with symptomatic carotid stenosis (Kock, Nygaard et al. 2008). Axial T1-, T2-, and proton density-weighted images, as well as time-of-flight angiographic images were acquired at resolution of 0.6 x 0.6 x 2 mm. Because all imaging studies were made with axial orientation and the FEM models were of longitudinal slices through the diseased carotid bifurcation, significant image processing and geometry preparation was necessary. While the models showed clear first principle stress peaks of reasonable magnitude proximal to the stenotic throat, interpretation of these stresses must be made carefully. It is unlikely that the actual stresses in the artery are represented. A real artery would exhibit maximal stress in the circumferential direction, a state of stress not resolvable with this model. From earlier work (Kock, Frund et al. 2006) it is assumed that plane strain elements were used to account for an extended geometry, but it is not clear how well this approximation would hold for such geometry and loading. Kock et al.'s model, nonetheless, represents a comprehensive approach to constructing an FEM model of the carotid bifurcation from *in vivo* MRI studies, and contains nearly all salient modeling techniques used for fully 3D patient-specific simulations.

#### **1.7.4 3D Patient-Specific FEM Studies**

While 2D analyses of diseased vessels have helped to identify relationships between morphological features and distributions of stress and strain, the *in vivo* mechanical state of the vessel is fully three-dimensional. 2D studies of transverse cross-sections of the diseased vessel make a plane-strain assumption, which may not be suitable for lesions whose composition is longitudinally heterogeneous. These models also fail to resolve out-of-plane components of deformation, which may be significant for some

lesions. Furthermore, as shown in several studies of stenotic vessels, the pressure load felt at a longitudinal position in a diseased vessel is highly dependent on local geometry and flow conditions. It is difficult to be certain that using systolic pressure loading at the luminal boundary of the vessel is appropriate in the 2D model. Because of these limitations, several groups have begun to model diseased arteries using multi-component 3D FEM simulations, with either uniform pressure or strongly-coupled FSI to load the vessel wall. There are numerous challenges in 3D modeling of diseased vessels. Suitable imaging, image processing and segmentation are difficult to achieve. Mesh generation for complex 3D geometries is tedious and mesh independence is not easily established. Additionally, nonlinear material response and strong FSI lead to convergence issues and high computational expense. For these reasons, 3D multi-component models of atherosclerotic vessels are relatively few in the literature compared to 2D studies.

Tang et al. used high resolution *ex vivo* MR images of a carotid endarterectomy specimen as the basis for a 3D FSI model (Tang, Yang et al. 2004). 64 image slices at a resolution of 0.1 x 0.1 x 0.5 mm were segmented into fibrous plaque and lipid pool. A constant 0.8 mm thick layer was added around the segmented geometry to account for the portion of vessel left behind during the endarterectomy. While several variations were modeled to examine the relative influence of different plaque features on the stress field, the baseline model used normal tractions of 100 mmHg and 98.5 mmHg at the inlet and outlet of the flow domain, respectively, for a physiological peak carotid flow rate of 17.5 ml/s. An axial stretch of 20% was applied to the solid domain (the flow domain follows due to FSI boundary conditions) to simulate *in vivo* residual stressing conditions. The study showed that the stresses and strains in the diseased vessel wall under physiological

conditions are indeed highly variable in all three dimensions, and are determined by several factors. The flow boundary conditions and assumed state of axial stretch were shown to greatly affect the stresses and strains in the wall. Fig. 1.5 compares the results obtained at the same location using 2D and 3D models with and without FSI and with varying axial stretches.

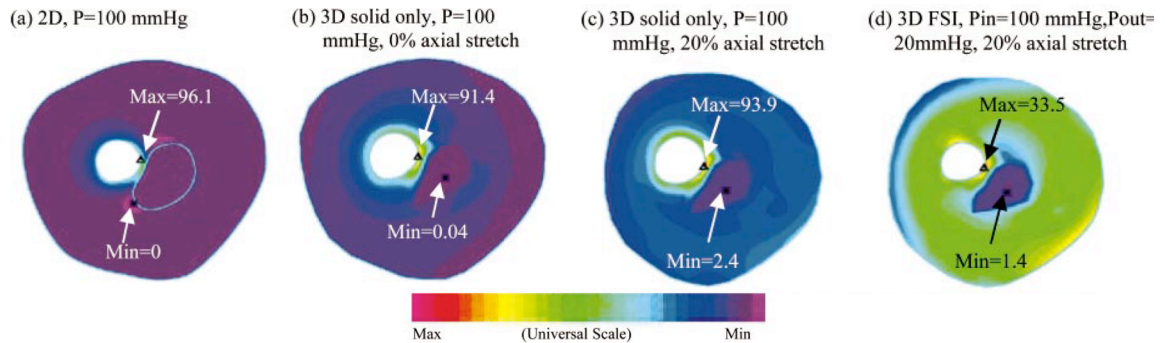


Fig. 1.5 (a) 2D, solid-only model with plane-strain assumption; (b) Fully 3D solid-only model without axial stretch; (c) 3D solid-only model with axial stretch of 1.2; (d) Full 3D, FSI model with pressure conditions at inlet and outlet for physiological flow rate, axial stretch of 1.2. Taken from (Tang, Yang et al. 2004).

In the solid only results shown in Fig. 7b,c the effect of the 3D modeling and inclusion of axial stretch is minimal, as the material distribution in this model varied little longitudinally. The differences between models a and d, however, clearly make a strong case for needing 3D FSI simulations for stenotic geometries.

## 1.8 Toward an Understanding of Plaque Rupture

There is a pressing clinical need for a robust way to assess the rupture risk of atherosclerotic lesions. Specific to carotid atherosclerosis, such a capability could help reduce the significant morbidity and mortality associated with plaque rupture and stroke.

It is thought that the combination of state-of-the-art medical imaging and biomechanical analysis could identify carotid plaques that are likely to rupture and cause potentially devastating thromboembolism. Many studies have succeeded in revealing the complexities of diseased vessel mechanics, and have made comparative analyses of various lesion types in an attempt to understand how plaque features influence plaque stresses and rupture potential. As a result of the diverse models studied and the equally diverse modeling strategies employed, a number of possible rupture mechanisms have been proposed, including plaque exposure to extreme flow-induced shear stress (Gertz and Roberts 1990; Groen, Gijssen et al. 2007; Fukumoto, Hiro et al. 2008), local vessel collapse from critical flow conditions (Binns and Ku 1989; Tang, Yang et al. 1999), cyclic stress/strain conditions (McCord and Ku 1993; Bank, Versluis et al. 2000; Versluis, Bank et al. 2006), and critical stresses within the fibrous cap of a lesion (Loree, Kamm et al. 1992; Cheng, Loree et al. 1993; Li, Howarth et al. 2007).

The mechanical analyses used to explore these possible rupture mechanisms have, with exception to that by Groen et al. (Groen, Gijssen et al. 2007), used idealized diseased vessel geometries, artificially repaired geometries from ruptured lesions, or have used histological features, structural features, or the patient's symptom status as a surrogate for rupture. Groen et al. used serial MRI data of a 67 year old woman with pre- and post-rupture imaging studies to show that a carotid plaque ruptured in a region of locally elevated wall shear stress. Their analysis was based on a rigid-wall computational fluid dynamics (CFD) simulation with large assumptions made of the flow boundary conditions, which can dramatically affect the predicted hemodynamics (Friedman and Giddens 2005).

There is currently a deficiency in the literature regarding well-posed mechanical analyses of atherosclerotic plaques that are known to rupture. Boundary conditions on geometry, composition, flow, and vessel displacement have potentially enormous influence on the results of such analyses and should be determined from the pre-rupture conditions within the diseased vessel. Additionally, these boundary conditions should be enforced with a realism and fidelity commensurate with their effects on analysis predictions.

In the following, we present a modeling methodology suitable for such mechanical analyses. We will also present a useful scheme for keeping the computation time reasonable for these highly realistic computational models, facilitating accurate *and* timely simulation. This is important, as conclusions drawn from such analyses will take on more meaning and reliability as a greater number of cases are studied. Finally, we will present the first 3D FSI analysis of an atherosclerotic carotid bifurcation based upon pre-rupture imaging data with available post-rupture imaging information on rupture site and extent.

## Chapter 2 – Methods

Construction of a model requires adequate definition of the features and relevant physics that determine the behavior of the system. Roughly speaking, for a mechanical analysis, an appropriate definition is needed for each of the following:

Geometry	The size, shape, distribution, and connectivity of materials present in the system
Physics	The laws of motion describing the system's evolution and/or interactions between subsystems
Materials	The mechanical response of the materials present, under the range of loading considered
Loading	The mechanical forces that act on the system
Boundary Conditions	Constraints placed upon the primary variable(s) of the analysis, commonly the displacements in a mechanical model and pressures and velocities in a fluid dynamics model

Additionally, a suitable method of analysis must be defined for the model. For a finite element model, several types of analysis are available, each employing different approximations and numerical representations of the physics of the system. The finite element methods are diverse, and nearly every parameter of the analysis may be optimized for any particular problem. The following is a coarse overview of the analysis features that must be defined for the model.

Geometric Discretization	The numerical representation of the geometry as a set of finite elements
Element Formulation and Discretized Physics	The specific physical behavior assumed to be valid over each element and the mathematical representation of relevant physics over the discretized domain

Time Discretization, Time Integration	Discrete representation of continuous behavior and the numerical scheme to predict system evolution from initial conditions
Load and Boundary Condition Discretization	Redefinition of distributed loads or displacement constraints in a manner suitable to the discretized geometry
Numerical Methods	The mathematical techniques used to solve for primitive variables of the system's behavior.

This chapter will present the methods used to construct patient-specific finite element models of the atherosclerotic carotid bifurcation. Each one of the major system and analysis features listed above will be discussed with regard to a 3D fluid-structure interaction model. Thus, the methods presented will relate to the solid mechanics of the vessel wall, the fluid dynamics of the circulation, and the interaction between the two.

## 2.1 Geometry

### 2.1.1 Imaging

Patient-specific mechanical analyses of *in vivo* conditions rely on medical imaging to provide geometric boundary conditions relating to vessel morphology and plaque composition. In this work, computed tomography angiography images were used to reconstruct the three-dimensional geometry of the diseased vessel wall, including delineations between wall and plaque components. The CT technique used to acquire the images is as follows: Spiral mode; collimation, 16 x 1.25mm; 240 kVp/350 mA; 70 mL at 4mL/sec power injection in antecubital vein, Omnipaque contrast. Images were acquired caudocranial, covering from the vertex to the heart with an in-plane resolution of .49 mm x .49 mm. Representative CTA images of the diseased carotid bifurcation are



shown in Fig. 2.1. The methods used to construct a 3D FSI model of the atherosclerotic carotid bifurcation will all be presented in respect to the imaging dataset shown in Fig.

2.1.

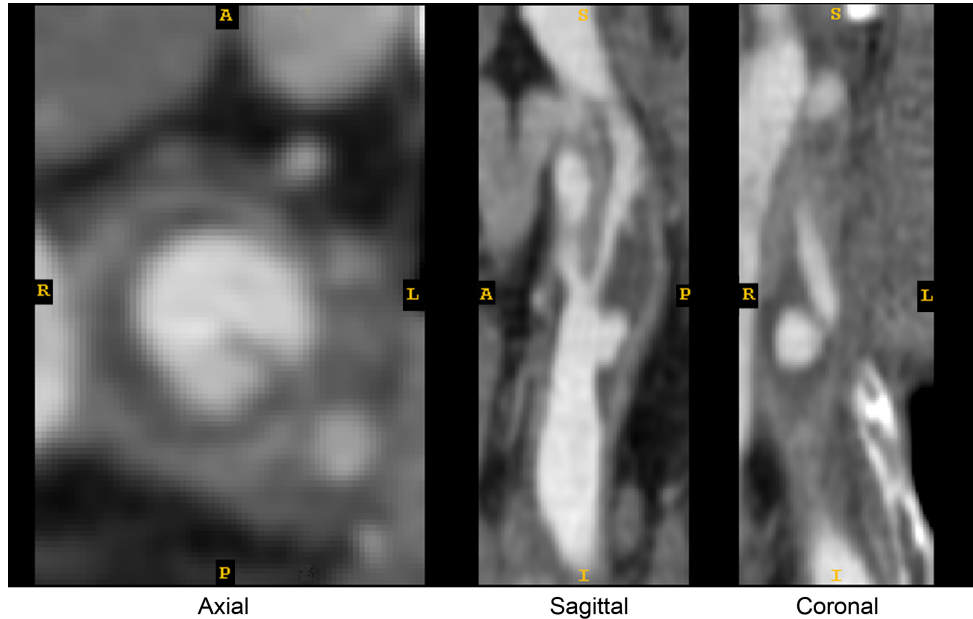


Fig. 2.1 Axial, sagittal, and coronal views of diseased carotid bifurcation from CTA study.

### 2.1.2 Segmentation Strategy

Unlike MR imaging, the contrast between materials in a CT study relates to only one property of the materials, namely, their attenuation of x-ray radiation. Thus, materials can be distinguished in CT studies based upon their intrinsic x-ray attenuation, or the attenuation enhancement provided by highly radiodense contrast agents. The x-ray attenuation is quantified on the Hounsfield scale, and this is displayed in the CT images. The Hounsfield unit ranges we used to identify different materials were based on results from de Weert et al. (de Weert, de Monye et al. 2008), from Wintermark et al. (Wintermark, Jawadi et al. 2008), and from image features, and are provided in table 2. Note that the ranges for the contrast enhanced blood and calcification overlap. Careful

observation near the lumen boundary, and attention to very high image intensities (> 400 H.U.) can help to correctly identify the boundary between these two features.

<b>Material</b>	Hounsfield Unit Range
Fibrous Tissue (Vessel Wall, Fibrous Plaque)	65 – 170
Lipid Pool	65 and below
Contrast Enhanced Circulating Blood	170 - approx 400
Calcification	255 and above

Table 2.1 Hounsfield unit ranges used for segmentation.

To establish a vascular geometry from the stack of planar medical images, the images must first be segmented into the materials listed in Table 1. The image series may be segmented on a slice-by-slice basis, generating an axial series of vessel and plaque component contours, or a 3D segmentation algorithm may be employed.

Construction of a 3D geometry from a series of independent contours is achieved by lofting a surface in the axial direction, using the contours as constraints. Although this is commonly done in the literature, this is problematic for three reasons. First, segmentation of plaque and vessel components on each slice, independent from other slices neglects what we know about the continuity of certain features of the diseased vessel. Independent segmentation of each slice, given image noise, is likely to generate consecutive axial contours that have unrealistic transverse deviations from one another. The result is a geometrical model with a falsely “stepped” appearance. Second, when lofting between contours, a piecewise linear interpolation can be used, or a spline interpolation across 3 or more contours may be used. Piecewise linear interpolation requires significant post-lofting smoothing to rid the geometry of sharp features. Multi-contour spline interpolation generates smoother geometries, but drastically decreases the reproducibility of the method, and can generate “wavy” geometries. Third, lofting

methods are incapable of directly handling bifurcating geometries, and a great deal of user interaction is required to produce a reasonable model. This increases the possibility of modeling bias and again is injurious to method reproducibility.

To avoid artificially stepped or wavy geometries and prevent modeling bias, and to ensure reproducibility of our methods, a semi-automatic algorithm was used to identify regions of lipid pool, calcification, and contrast-enhanced blood in the images. In this way, fibrous plaque thickness between the lumen and lipid pool, the feature of utmost importance to plaque stresses, is determined solely from the semi-automated segmentation. Because perivascular tissue often has an image intensity similar to that of the vessel wall, a manual segmentation of the vessel wall outer boundary was made. As shown in Fig. 2.2, when the carotid bifurcation is exposed during endarterectomy, the outer vessel wall appears smooth. For this reason, manual segmentation was guided by not only image intensity, but also curvature of the vessel boundary in 3 dimensions.

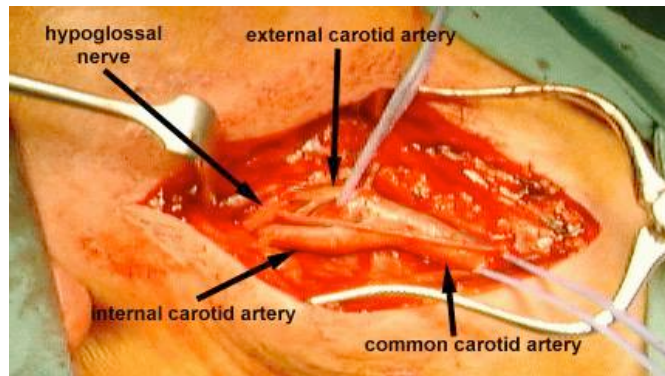


Fig 2.2. Carotid bifurcation exposed during endarterectomy procedure. Note the smoothness of the vessel wall. Taken from <http://www.gvg.org.uk/>.

### 2.1.3 3D Active Contour Segmentation and Manual Segmentation

The CTA images were segmented using the open-source image segmentation code ITK-SNAP (Yushkevich, Zhang et al. 2005). For the semi-automatic segmentation, ITK-SNAP's 3D active contour algorithm was used to generate a bounding surface for the vessel lumen and lipid pools. The 3D active contour is a closed surface  $C(\vec{s}, t)$  that propagates in time through the image space according to the partial differential equation

$$\frac{\partial}{\partial t} C(\vec{s}, t) = F \hat{n} \quad (2.1)$$

where  $\vec{s}$  is a vector of generalized coordinates parameterizing  $C$ ,  $t$  represents time,  $F$  is a force, and  $\hat{n}$  is the outward normal of  $C$  at every location. Thus, the closed 3D surface evolves expands or contracts in the direction of the local surface normal according to the force  $F$ .

There are different ways to compute the forcing term of eq. 2.1, depending on the nature of the images being segmented. ITK-SNAP offers an image intensity gradient method and a region competition method. Because the intensities corresponding to the various plaque and vessel materials are quite similar compared to the dynamic range of the image set, a gradient-based approach is inappropriate and a region competition method was used to determine the form of  $F$ . In the region competition approach,  $F$  is given as

$$F = \alpha(P_{obj} - P_{bg}) - \beta\kappa \quad (2.2)$$

where  $(P_{obj} - P_{bg})$  is a map of the probability that a voxel nearby the contour lies within the object of interest rather than the background (Yushkevich, Piven et al. 2006). The map is constructed by applying a smoothed threshold on the image according to the intensity range of the object.  $\kappa$  is the mean local curvature of the contour.  $-1 \leq \alpha \leq 1$  and  $0 \leq \beta \leq 1$  are user-defined constants that determine the balance between the force based on curvature and the force based on the threshold-based probability map. Note that for a negative  $\alpha$ , the contour will propagate inward, which is useful in cases where the background intensity is better known than the intensity of the object of interest. A greater value for  $\beta$  will increase the smoothness of the contour, while a value closer to 0 will allow the contour to adopt more detailed shaped.

Active contour segmentation works best when the voxels of a dataset are nearly isotropic. The original CTA acquisition gave a voxel size of 0.49mm x 0.49mm x 1.25mm. To achieve a more isotropic voxel without generating an excessively large dataset, the images were resampled by a factor of two in-plane and by a factor of 4 through-plane to give voxels of 0.245mm x 0.245mm x 0.3125mm, essentially “twice as isotropic”.

To define the lumen geometry from the CTA images, several spherical seed contours were placed within the 3D dataset so that they clearly lied within the lumen.  $\alpha = 0.5$ , and  $\beta = 0.2$  were specified, and the contour was allowed to propagate until it reached roughly 4cm proximal and 4cm distal to the bifurcation. The lipid pool is expected to be far more irregular in shape, and so  $\alpha = 0.5$ , and  $\beta = 0.05$  were specified, and the active contour was allowed to propagate until no further evolution was observed in regions with clear lipid pool boundaries. Seeds for the lipid contour were more numerous than for the

lumen, and were placed after a careful search through the 3D dataset for regions displaying lipid-like image intensities.

Manual corrections were made to the semi-automatic segmentations to eliminate artifacts such as bleed-over into a nearby vessel or bone. Corrections were based on voxel intensity as well as local vessel features (i.e. branching of the ECA into the superior thyroid artery, lipid pools must be inside the vessel wall, etc). Axial, sagittal, and coronal views of the segmented lumen and lipid pools are shown in Fig. 2.3.

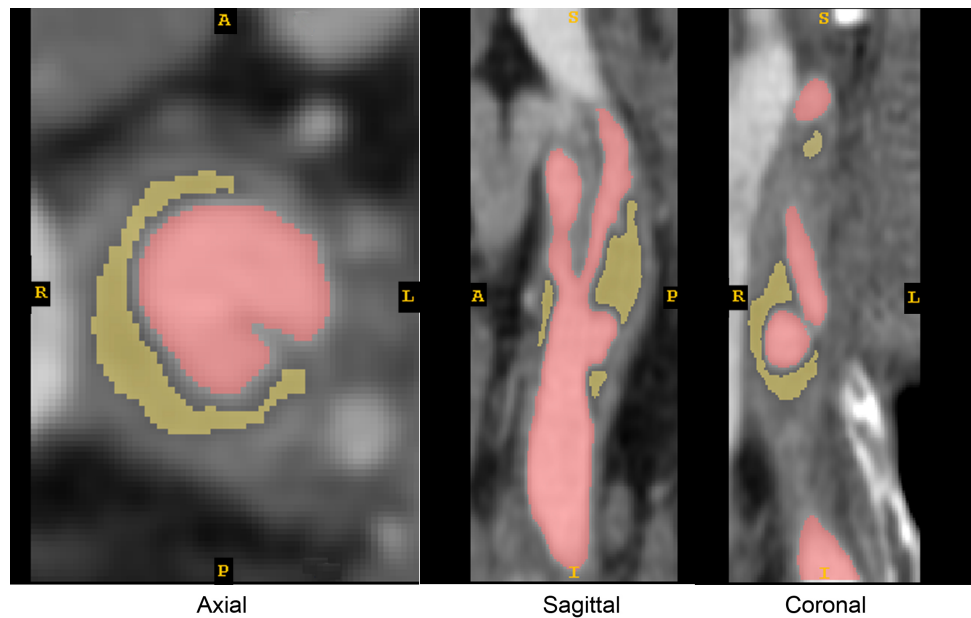


Fig. 2.3 Axial, sagittal, and coronal views presented in Fig. 2.2 with overlays of segmented lipid pool and lumen.

The manual segmentation of fibrous tissue (including healthy vessel wall and fibrous plaque) was made so that the lumen and lipid pools were always bordered by at least 2 voxels of fibrous tissue, and the vessel wall outer boundary appeared smooth in any projection. Axial, sagittal, and coronal views of the segmentation, including lumen, lipid pools, and fibrous tissue are shown in Fig. 2.4.

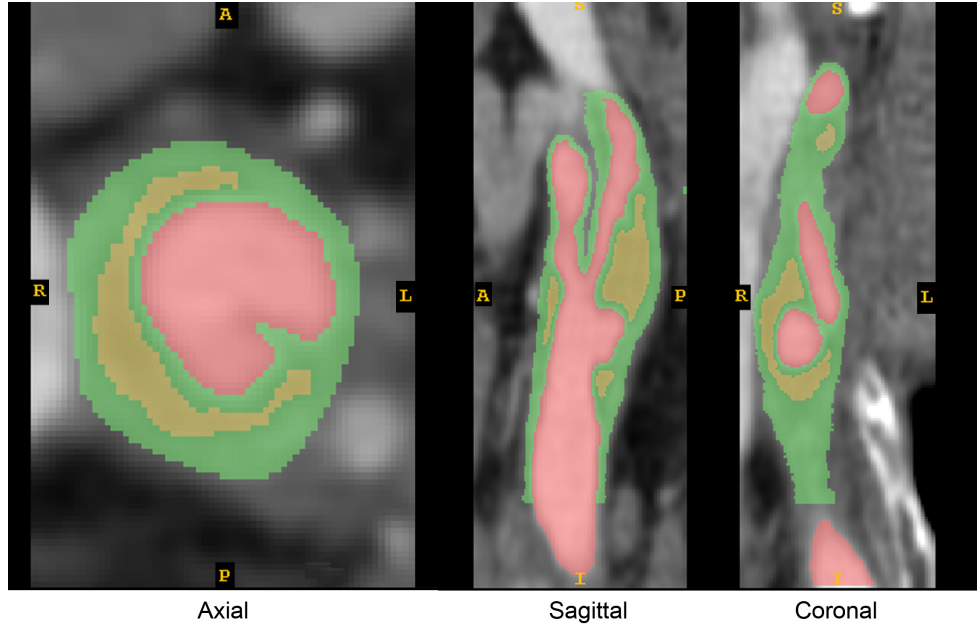


Fig. 2.4 Axial, sagittal, and coronal views presented in Fig. 2.2 with overlays of segmented lipid pool, lumen, and fibrous tissue (vessel wall and fibrous plaque).

### 2.1.4 Geometry Reconstruction from Segmented Images

Segmentation of the CTA images only labels each voxel as comprising a certain material, and an explicit geometric entity is not yet made. To construct the geometry of each plaque and vessel component, the set of each material's boundary voxels were triangulated into surface meshes. Even though the 3D active contour segmentation method produces smoother segmentations than other methods, smoothing of the triangulated meshes is still generally required to achieve biologically reasonable (i.e. smooth) geometries suitable for finite element mesh generation. In ITK-SNAP, an isotropic Gaussian kernel given by

$$k(x,y,z) = \frac{1}{(2\pi)^{3/2}\sigma^3} e^{-\frac{x^2+y^2+z^2}{2\sigma^2}} \quad (2.3)$$

was convolved with the vertex map of the original triangulated surface mesh of each material. In eq. 2.3,  $x$ ,  $y$ , and  $z$  are Cartesian distances from a particular vertex assumed to be at the origin. For each vertex, the convolution kernel establishes the weight of neighboring vertices used in a weighted average of 3-dimensional position.  $\sigma$  is the standard deviation of the Gaussian distribution and is the same in all 3 Cartesian axes. In this work,  $\sigma$  was chosen to be 0.8, and the window of the kernel was set so that vertices with a computed weight less than 0.03 were not factored into the smoothing operation. The discrete version of the Gaussian kernel was normalized by the sum of contributing weight factors. For the voxel size used in the segmentation, the convolution kernel extended 4 vertices in each Cartesian axis, and 3 vertices along main diagonals. Results of the Gaussian smoothing operation are shown for the lumen, large lipid pool and outer vessel wall in Figs. 2.5, 2.6, and 2.7, respectively. A small lipid pool at the distal ICA is not shown for brevity.



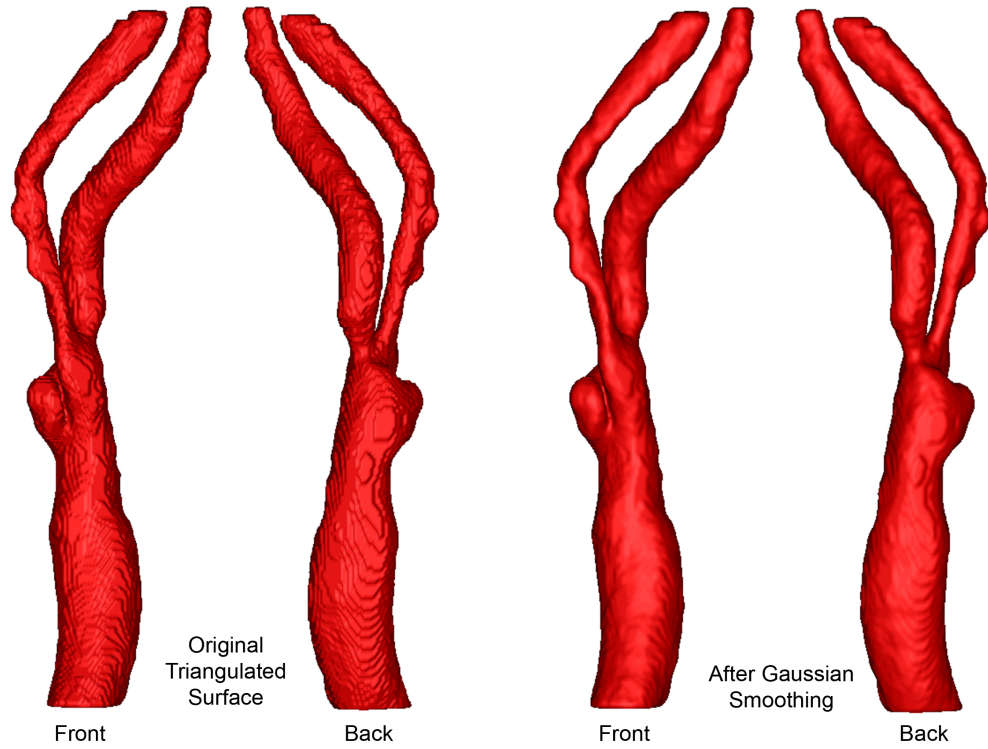


Fig. 2.5 Front and back views of the lumen surface, as originally triangulated from the segmentation and after application of Gaussian smoothing algorithm.

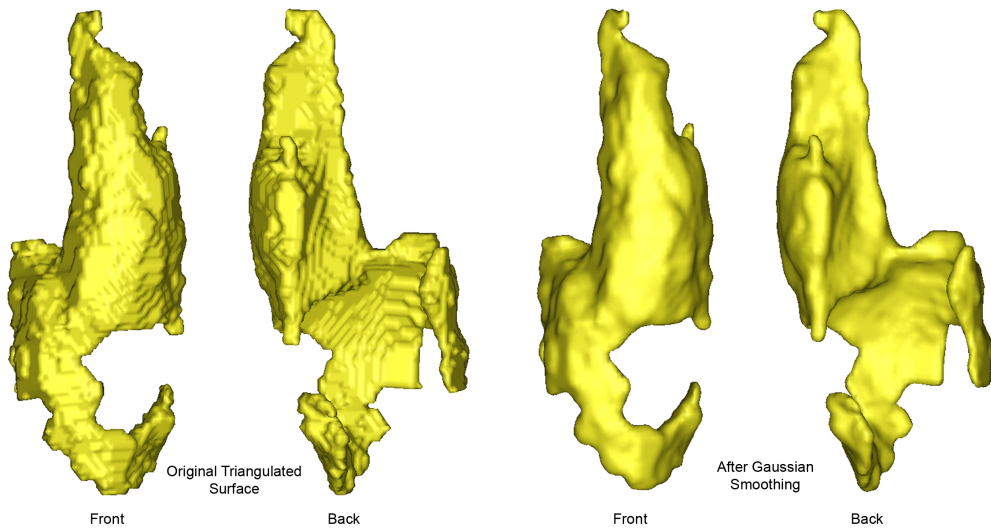


Fig. 2.6 Front and back views of the lipid pool surface, as originally triangulated from the segmentation and after application of Gaussian smoothing algorithm.

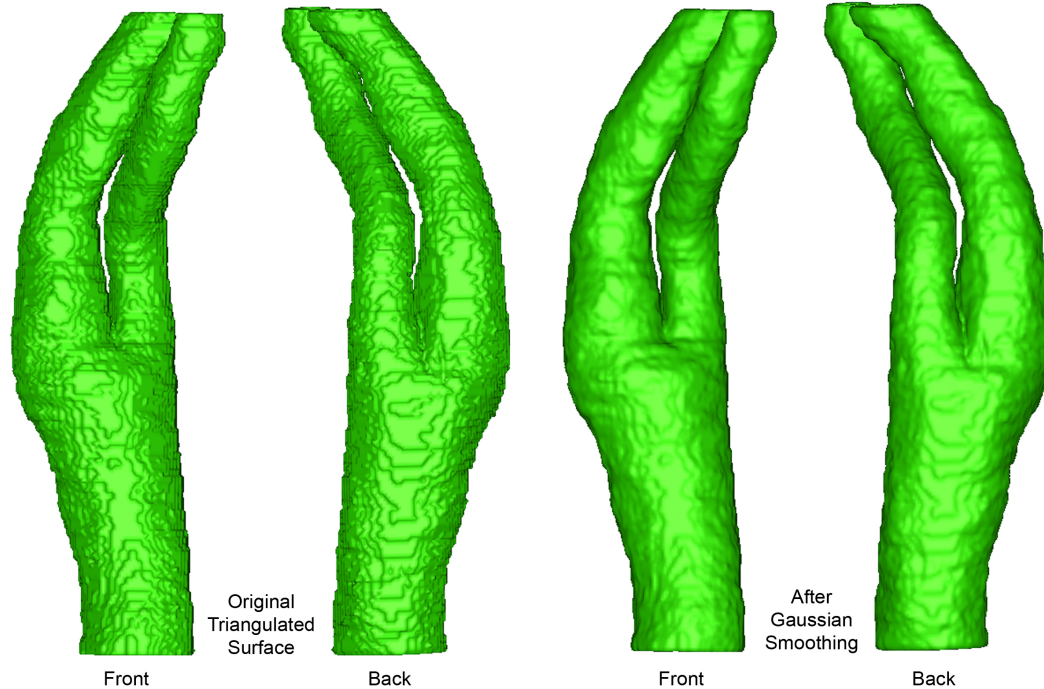


Fig. 2.7 Front and back views of the vessel wall outer surface, as originally triangulated from the segmentation and after application of Gaussian smoothing algorithm.

Smoothing the triangulated surface meshes is still not sufficient to ensure the best possible geometry on which to build a finite element mesh. To have the most user control in the finite element meshing process, it is useful to parameterize the surfaces so that they can be addressed and partitioned without referring to a set of discrete vertices. The parameterization we used is based upon non-uniform rational B-spline (NURBS) descriptions of the surface. NURBS are commonly used throughout the computer graphics and computer aided design communities and are capable of representing free-form surfaces in an accurate and efficient manner. In order to make the best NURBS representations of the vessel and plaque components, it is necessary to re-mesh the smoothed triangulated surface meshes of each component. Re-meshing is a complex operation to optimize the size and shape of mesh triangles based upon local features, and

was performed using the commercial 3D scanning software Rapidform (INUS Technology, Inc. Korea).

Unfortunately, in image-based modeling of biological tissues, we often cannot be certain that the reconstruction of the tissue geometry is accurate. This uncertainty is due primarily to inherent imprecision in the *in vivo* imaging modalities employed, but can also arise from the use of inappropriate reconstruction and modeling techniques. To ensure that the smoothing and remeshing operations did not introduce distortions to the surface reconstructions that would compromise the original segmentation, the volume enclosed by each surface was tracked during the operations. Additionally, the deviation of the final surfaces from the original, unsmoothed triangulations was measured. The target accuracy was arbitrarily set at  $\frac{1}{2}$  of the in-plane pixel width after resampling, or 0.1225mm. Fig. 2.8 shows the smoothed surface triangulation and the surface after remeshing for the large lipid pool. Similar results were achieved for the lumen and outer vessel wall surfaces. The volumes of the progressively smoother and more realistic meshes are given in Table 3, while the deviations of the final surfaces from the initial triangulations are shown in Figs. 2.9, 2.10, and 2.11.

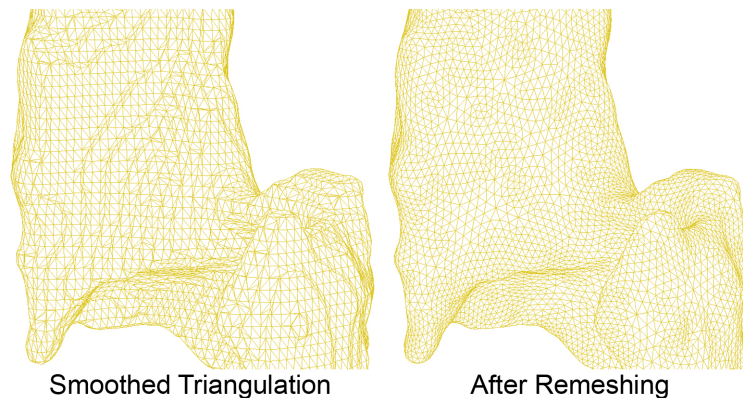


Fig. 2.8 Close-up view of the lipid pool surface after Gaussian smoothing, and after a subsequent remeshing.

Volumes enclosed by progressively smoother surfaces (mm <sup>3</sup> )	Lumen	Large Lipid Pool	Outer Vessel Wall
Original Triangulated Surface	1483.19	430.60	4369.12
Gaussian Smoothed Surface (% deviation from original)	1475.62 (0.51%)	423.93 (1.55%)	4361.42 (0.18%)
Smoothed, Remeshed Surface (% deviation from original)	1464.24 (1.28%)	422.23 (1.94%)	4350.37 (0.43%)

Table 2.2 Volumes of the triangulated surface meshes as originally segmented, after Gaussian smoothing, and after both smoothing and remeshing.

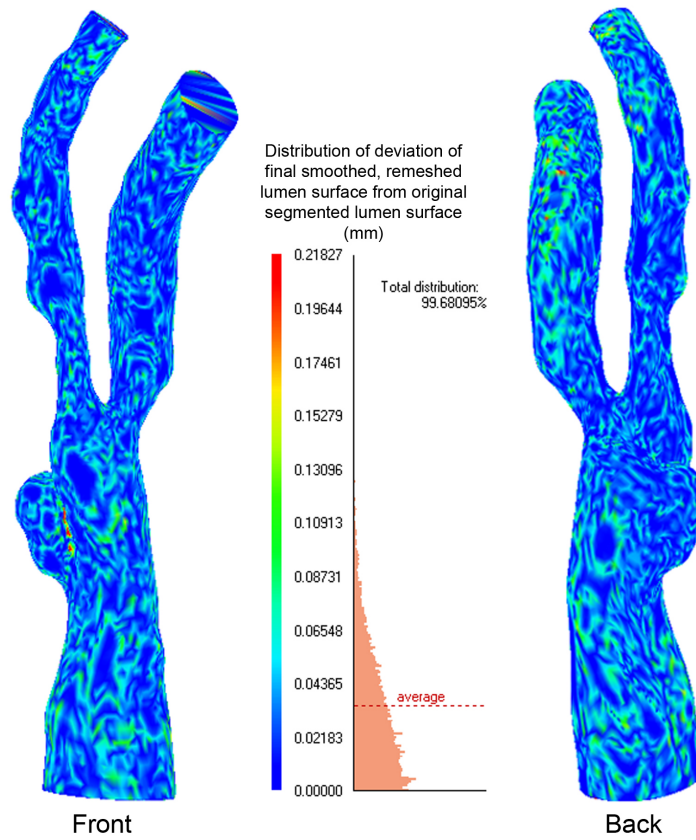


Fig. 2.9 Front and back views of deviation between original triangulation of lumen surface and final surface, after smoothing and remeshing. The magnitude of the deviation is plotted on the final surface.

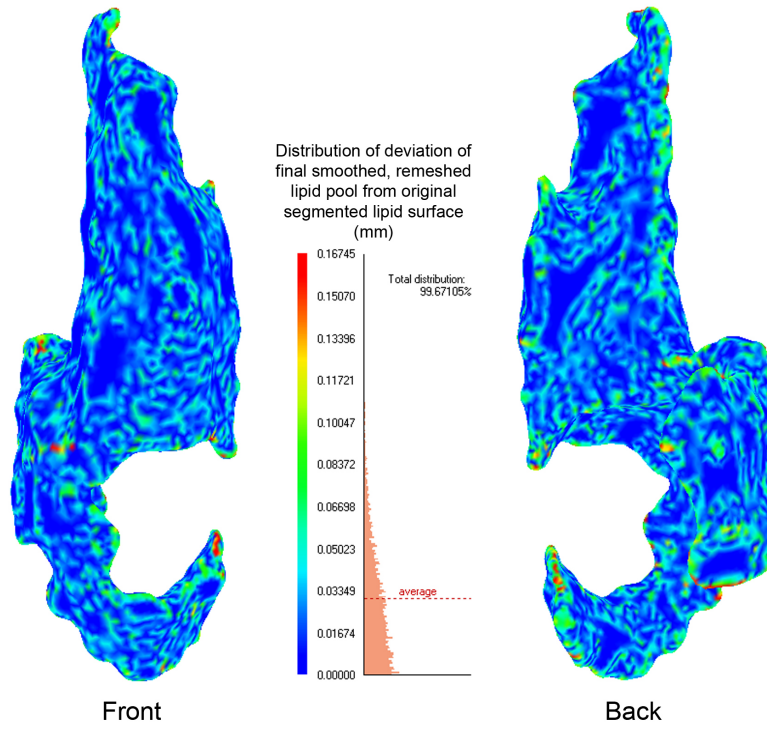


Fig. 2.10 Front and back views of deviation between original triangulation of lipid pool surface and final surface, after smoothing and remeshing. The magnitude of the deviation is plotted on the final surface.

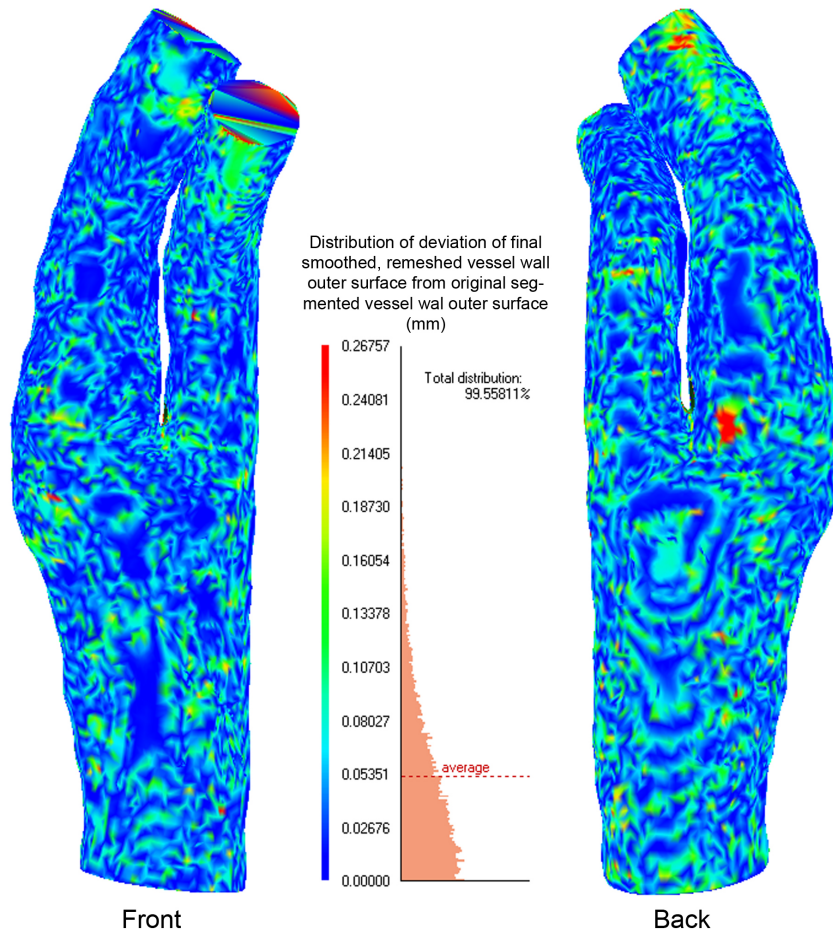


Fig. 2.11 Front and back views of deviation between original triangulation of the vessel wall outer surface and final surface, after smoothing and remeshing. The magnitude of the deviation is plotted on the final surface. The closed ends of the ICA and ECA are included in the deviation analysis, but do not factor into the reconstructed geometry and result from the need for a closed surface for the volume analysis. The small patch of higher deviation near the apex of the bifurcation will be discussed in the next section.

As shown in Table 3, smoothing and remeshing had only a small effect on the volume enclosed by the triangulated surfaces. Figs. 2.9-2.11 additionally show that the average deviations of the final surfaces from the original segmentation surfaces are 0.035mm, 0.032mm, and 0.053mm for the lumen, lipid pool, and outer vessel wall,

respectively. These average deviations are well below the target deviation of 0.1225mm. The deviation distributions and color plots of Figs. 2.9-2.11 also show that virtually no vertices deviate from their original positions by more than the target of 0.1225mm for the lumen and lipid pool surfaces. A very small fraction ( $\sim 4\%$ ) of vessel wall vertices exceeded the target deviation, although this was a result of a manual adjustment of the vessel wall outer surface that will be explained in the next section.

### **2.1.5 Fibrous Plaque Layer**

It is not currently possible to reliably distinguish between fibrous plaque and healthy vessel wall in CT imaging. We know from Fig. 1.3 that the typical wall thickness in the healthy carotid bifurcation is between 0.9mm at the CCA and 0.5mm just past the carotid bulb of the ICA. We additionally know from the histological analyses of several atherosclerotic arteries that lipid pools and calcifications generally lay within a layer of fibrous plaque. For this reason, we assumed that any region between the lumen surface and the lipid pools in our model was occupied by fibrous plaque (Loree, Kamm et al. 1992; Cheng, Loree et al. 1993; Kaazempur-Mofrad, Younis et al. 2003; Chau, Chan et al. 2004). We also assumed that in regions of the vessel where the distance between the vessel wall outer surface and lipid pool or lumen was greater than 0.5mm, the first 0.5mm inward from the vessel wall outer surface was occupied by healthy vessel wall tissue with the balance being fibrous plaque.

To construct a fibrous plaque/healthy wall tissue interface, a constant 0.5mm inward offset surface was generated from the vessel wall outer surface. The fibrous plaque was assumed to extend longitudinally such that all lipid pools were fully

contained within fibrous plaque, healthy CCA wall thickness was less than 1.0mm, and healthy ICA wall thickness did not exceed 0.5mm. The region of high surface deviation in Fig. 2.11, near the back face of the apex of the bifurcation, had an original wall thickness less than 0.5mm. This small patch of the vessel wall outer surface was artificially expanded outward to accommodate a 0.5mm wall thickness and a small thickness of fibrous plaque. In this way, the fibrous plaque layer fully encased the large lipid pool and the lumen in any region where fibrous plaque was modeled.

### **2.1.6 Final Geometry**

A geometry suitable for finite element analysis must have boundaries on which the behavior is well understood. In CFD, outlets of vessels should be in locations where secondary flow is not expected to be appreciable. Additionally, outlet surfaces should be normal to the local vessel centerline, as this will ensure that the outlet pressure is nearly uniform. It is convenient for the vessel inlet surface to also be normal to the local vessel centerline, as this will allow for the easiest assignment of inlet flow conditions. In terms of the vessel's solid mechanics, pressurization of the vessel generally causes a nearly radial expansion, and so inlet and outlet surfaces should be nearly normal to the local vessel centerline so that displacement constraints are easily prescribed. The final geometries of the vessel and plaque components, after appropriate trimming of the inlet and outlet regions, are shown as geometric solids in Fig. 2.12.



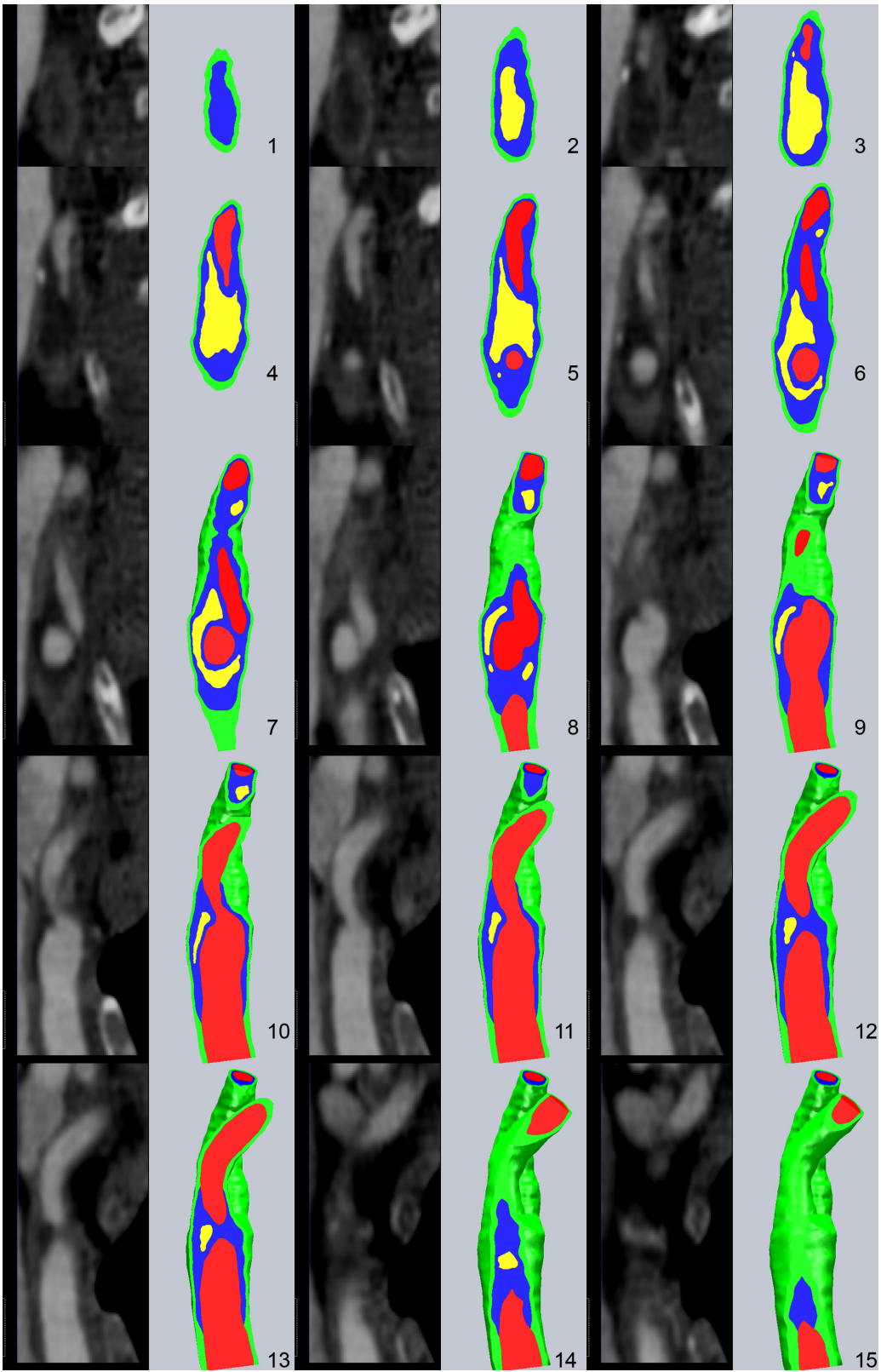


Fig. 2.12 Consecutive coronal slices from posterior (1) to anterior (15) showing vessel and plaque geometries as reconstructed from images. Red = blood, Blue = fibrous plaque, Green = healthy vessel wall, Yellow = lipid pool. Note: the small lipid pool at the distal ICA is shown here, but not elsewhere.

## 2.2 Physics

Like many other structures in the human body, blood vessels interact continuously with a fluid, in this case, blood. In order to make the most complete mechanical analysis of the blood vessel, we must properly account for the physics of not only the vessel wall, but also the flowing blood. Additionally, interactions between the fluid and solid domains must be accurately captured. Both domains are considered in the continuum approximation, and are considered to be isothermal.

### 2.2.1 Physics of the Vessel Wall

The tissues within the diseased vessel wall, save for possible calcification, generally behave according to large deformation nonlinear mechanics. Without yet committing to any particular material behavior, we can present the equation of motion for a solid continuum. Let  $B$  be a deformable continuum occupying a region  $\Omega$  bound by a closed surface  $\partial\Omega$  at time  $t$ .  $B$  is acted upon at  $\partial\Omega$  by surface traction  $\vec{t} = \vec{t}(\vec{r}, t, \hat{n})$  and throughout  $\Omega$  by the body force (e.g. gravity)  $\vec{b} = \vec{b}(\vec{r}, t)$ , as shown in Fig. 2.13.

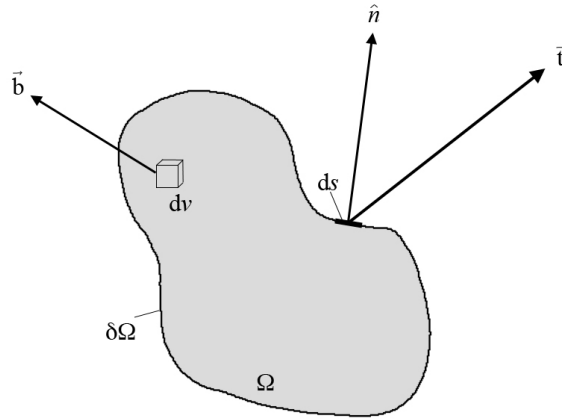


Fig. 2.13 Body  $B$  in the current, deformed configuration, under action of body force and surface traction.

We may write the balance of linear momentum within  $\Omega$  as

$$\frac{D}{Dt} \int_{\Omega} \rho \dot{\mathbf{u}} dv = \int_{\partial\Omega} \bar{\mathbf{t}} ds + \int_{\Omega} \bar{\mathbf{b}} dv \quad (2.4)$$

where  $\frac{D}{Dt}(\bullet)$  denotes the material time derivative and  $\bar{\mathbf{u}}$  is the displacement of a particle within  $B$ . Use of the Cauchy stress theorem,

$$\bar{\mathbf{t}}(\bar{\mathbf{r}}, t, \hat{\mathbf{n}}) = \boldsymbol{\sigma}(\bar{\mathbf{r}}, t) \hat{\mathbf{n}} \quad (2.5)$$

and application of the divergence theorem allows us to rewrite eqn. 2.4 as

$$\int_{\Omega} (\nabla \cdot \boldsymbol{\sigma} + \bar{\mathbf{b}} - \rho \ddot{\mathbf{u}}) dv = 0 \quad (2.6)$$

where  $\boldsymbol{\sigma}$  is the second-order Cauchy stress tensor that fully defines the state of stress at a point in the continuum. Because eqn. 2.6 holds for any partition of  $\Omega$ , the equation of motion for the solid continuum in the deformed configuration can be written simply as

$$\nabla \cdot \sigma + \vec{b} - \rho \ddot{\vec{u}} = 0 \quad (2.7)$$

### 2.2.2 Physics of Flowing Blood

Fluids are typically studied within the continuum approximation, and so eqn. 2.7 is a perfectly valid form of the equation of motion governing blood flow. This is not, however, the standard form for the fluid equation of motion. To obtain the standard form, known as the Navier-Stokes equations, we must make three modifications to eq. 2.7. To arrive at a form of the Navier-Stokes equations suited to blood flow in major arteries, two additional assumptions are made. The first is that the fluid is incompressible, and the second is that the fluid is Newtonian, that is, there is a constant viscosity relating fluid stress to the rate of strain in the flow.

As a first modification to eq. 2.7, we write the double time derivative of the displacement field  $\ddot{\vec{u}}$  in terms of the primary descriptive flow variable, velocity.

$$\ddot{\vec{u}} \equiv \dot{\vec{v}} \quad (2.8)$$

Next, we explicitly state the full form of the material time derivative of the spatial velocity field in eqn. 2.8

$$\dot{\vec{v}} \equiv \frac{D}{Dt} \vec{v} \equiv \frac{\partial}{\partial t} \vec{v} + (\vec{v} \cdot \nabla) \vec{v} \quad (2.9)$$

We also must decompose the stress tensor into its hydrostatic component which amounts to fluid pressure  $p$ , and the deviatoric component.

$$\boldsymbol{\sigma} = -p\mathbf{I} + \mathbf{T} \quad (2.10)$$

where  $\mathbf{I}$  is the 3x3 identity matrix, and  $\mathbf{T}$  is the stress tensor that causes iso-volumetric deformation of a control volume. Thus, the general form of the Navier-Stokes equations is

$$-\nabla p + \nabla \cdot \mathbf{T} + \bar{\mathbf{b}} + \rho \left( \frac{\partial \bar{\mathbf{v}}}{\partial t} + (\bar{\mathbf{v}} \cdot \nabla) \bar{\mathbf{v}} \right) = 0 \quad (2.11)$$

For Newtonian fluids, the components of the deviatoric stress tensor are

$$T_{ij} = \mu \left( \frac{\partial v_i}{\partial x_j} + \frac{\partial v_j}{\partial x_i} \right) + \delta_{ij} \lambda (\nabla \cdot \bar{\mathbf{v}}) \quad (2.12)$$

where  $\mu$  and  $\lambda$  are the fluid's viscosity and bulk viscosity.

Fluid incompressibility results in divergence-free flow fields, and can be stated as the continuity equation  $\nabla \cdot \bar{\mathbf{v}} = 0$ , so the second term in eqn. 2.12 can be neglected in blood flow. With the assumptions of incompressibility and constant viscosity, neglecting body forces, and a reordering of terms, the Navier-Stokes equations 2.11 can be written in the form commonly associated with large artery hemodynamics.

$$\rho \left( \frac{\partial \bar{\mathbf{v}}}{\partial t} + (\bar{\mathbf{v}} \cdot \nabla) \bar{\mathbf{v}} \right) = -\nabla p + \mu \nabla^2 \bar{\mathbf{v}} \quad (2.13)$$

### 2.2.3 Interactions Between the Vessel Wall and Flowing Blood

Although the vessel wall is permeable to components of circulating blood, this is typically ignored in mechanical analyses of blood vessels and blood flow. The blood

volume is assumed to not penetrate the vessel wall, and to fully occupy the lumen of the vessel at all times. With the vessel in motion during the cardiac cycle, the familiar no-slip condition of viscous flow needs to be enforced in a way that does not force the total velocity vector to zero at the vessel wall. At the interface between the fluid and solid domains with local surface normal  $\hat{n}$ , these conditions may be stated as

$$\begin{aligned}
 \bar{\mathbf{u}}_s &= \bar{\mathbf{u}}' \\
 \dot{\bar{\mathbf{u}}}_s &= \bar{\mathbf{v}} \\
 \ddot{\bar{\mathbf{u}}}_s &= \dot{\bar{\mathbf{v}}} \\
 \boldsymbol{\sigma}_s \cdot \hat{n} &= (-p\mathbf{I} + \mathbf{T}) \cdot \hat{n}
 \end{aligned} \tag{2.14a,b,c,d}$$

Where  $\bar{\mathbf{u}}_s$  is the vessel wall displacement,  $\bar{\mathbf{u}}'$  is the flow field displacement in the Arbitrary Lagrangian Eulerian (ALE) frame.  $\bar{\mathbf{v}}$  is the blood velocity,  $\boldsymbol{\sigma}_s$  is the Cauchy stress tensor for the wall tissue and  $\mathbf{I}$  and  $\mathbf{T}$  are as in eqns. 2.10, 2.12.

## 2.3 Materials

In large deformation nonlinear mechanics, the strains experienced by a material can far exceed the ~5% limit in which linear analysis will yield accurate results. Thus, approximating the current deformed configuration of a body by its initial reference configuration is no longer appropriate. Unfortunately, the current configuration of a deforming body is not generally known, and so measures of stress (force per unit area) are rarely known in the current configuration. This necessitates a way in which we can refer the mechanics of the deforming body back to the body's known reference state. The following is a very brief presentation of the measures of strain and stress that are suitable

for large deformation nonlinear mechanics and were used here to model the behavior of the diseased vessel wall. For a comprehensive review and derivation of this material the reader is referred to the seminal texts by Humphrey and Holzapfel (Holzapfel 2000; Humphrey 2002).

### 2.3.1 Large Deformation Mechanics

In nonlinear mechanics, the principal measure of deformation, which can be used to relate the current configuration back to the reference configuration, is the 2<sup>nd</sup> order deformation gradient tensor  $\mathbf{F} = \mathbf{F}(\mathbf{X},t)$ , with components given by

$$F_{ij} = \delta_{ij} + \frac{\partial u_i}{\partial X_j} \quad (2.15)$$

where  $\mathbf{X}$  denotes a position in the reference configuration, and  $u$  denotes a motion from the reference configuration to the current configuration. We can see from the Kronecker delta in eq. 2.15 that  $\mathbf{F}$  is descriptive of not only deformations, but also rigid body motion.  $\mathbf{F}$  is effectively a transformation, and maps an infinitesimal line element  $d\mathbf{X}$  in the reference configuration to the line element  $d\mathbf{x}$  in the current configuration.

$$d\mathbf{x} = \mathbf{F}(\mathbf{X},t)d\mathbf{X} \quad (2.16)$$

If we consider an infinitesimal vector of length  $d\epsilon$  at point  $\mathbf{X}$  in the direction of an arbitrary reference-configuration unit vector  $\hat{e}$ , we can write the transformation of the vector under  $\mathbf{F}$  as

$$(\lambda d\varepsilon)\hat{e}' = \mathbf{F}(X,t)d\varepsilon\hat{e} \quad (2.17)$$

where the primed unit vector resides in the current configuration. Thus, we have defined  $\lambda$  to be the amount of extension (or compression for  $\lambda < 1$ ) that the original vector experiences under the motion into the current configuration. If we make a comparison of the squared lengths of the transformed and original vector, we see

$$\begin{aligned} (\lambda d\varepsilon)^2 - d\varepsilon^2 &= (\mathbf{F}d\varepsilon\hat{e} \cdot \mathbf{F}d\varepsilon\hat{e}) - (d\varepsilon\hat{e} \cdot d\varepsilon\hat{e}) \\ &= (d\varepsilon\hat{e} \cdot \mathbf{F}^T\mathbf{F}d\varepsilon\hat{e}) - (d\varepsilon\hat{e} \cdot \mathbf{I}d\varepsilon\hat{e}) \\ &= d\varepsilon\hat{e}(\mathbf{F}^T\mathbf{F} - \mathbf{I})d\varepsilon\hat{e} \end{aligned} \quad (2.18)$$

Because this expression holds for an arbitrary vector, if we choose a measure of strain that corresponds to the difference in squared length between the reference and current configuration, we can define the strain tensor  $\mathbf{E}$  as

$$2\mathbf{E} = (\mathbf{F}^T\mathbf{F} - \mathbf{I}) \quad \text{or} \quad \mathbf{E} = \frac{1}{2}(\mathbf{F}^T\mathbf{F} - \mathbf{I}) \quad (2.19)$$

$\mathbf{E}$  is known as the Green-Lagrange strain tensor.  $\mathbf{F}^T\mathbf{F}$  is known as the right Cauchy-Green tensor  $\mathbf{C}$ , and is a symmetric, positive definite tensor related to the stretching of the material. The factor of 2 in eq. 2.19 is needed as it allows this nonlinear strain measure to reduce to the linear measure of strain in the case of small deformations.

In the small-deformation limit, the strain energy density of a deformed body as calculated with the nonlinear, large deformation theory should be equivalent to that calculated with the linear theory of elasticity. That is, we need a large-deformation measure of stress  $\mathbf{S}$  such that



$$\sigma \varepsilon = \mathbf{E} \mathbf{S} \quad (2.20)$$

where  $\sigma$  and  $\varepsilon$  are the Cauchy stress and linear strain tensors, respectively, and  $\mathbf{E}$  is the Green-Lagrange strain tensor.

The traction force acting on the current configuration, as understood from the Cauchy stress tensor and the deformed body's surface normal must be equivalent to the force calculated in the reference configuration, using a stress tensor that refers to the reference configuration. By performing an inverse transformation, using  $\mathbf{F}^{-1}$ , of the traction force and surface normal in the current configuration back to the reference configuration and equating the force to that dictated by the yet-unknown stress tensor and reference surface normal, it can be shown that the 2<sup>nd</sup> Piola-Kirchoff stress tensor  $\mathbf{S}$  is a suitable large-deformation measure of stress. The 2<sup>nd</sup> Piola-Kirchoff stress tensor expresses the current state of stress with regard to the reference configuration, and the components of  $\mathbf{S}$  can be related to the components of the Cauchy stress tensor as

$$\sigma_{jm} = \mathbf{F}_{ij} \mathbf{S}_{ik} J^{-1} \mathbf{F}_{mk} \quad (2.21)$$

$$\mathbf{S}_{jm} = \mathbf{F}_{ij}^{-1} \sigma_{ik} J \mathbf{F}_{mk}^{-1} \quad (2.22)$$

where  $J = \det(\mathbf{F})$  is the volume ratio between the current and reference configurations.

### 2.3.2 Constitutive Relation for Diseased Carotid Bifurcation Tissues

With measures of stress and strain that are suitable for large deformation mechanics, we are only left with the problem of defining a relationship between the two that is representative of the behavior of the materials we wish to study. Certain classes of

elastic materials, known as hyperelastic, may be characterized by a strain energy density function  $W$  that relates the states of strain and stress in the material. In nonlinear elasticity, the 2<sup>nd</sup> Piola-Kirchoff stress tensor may be related to the Green-Lagrange strain tensor through  $W$  as

$$\mathbf{S}_{ij} = \frac{\partial W}{\partial \mathbf{E}_{ij}} \quad (2.23)$$

$W$  is typically written as a function of components of the Green-Lagrange strain tensor  $\mathbf{E}$ , with weighting coefficients determined from material testing experiments. Because  $\mathbf{E}$  is a linear function of the symmetric, positive definite right Cauchy-Green tensor  $\mathbf{C}$ ,  $W$  may also be written in terms of the three invariants of  $\mathbf{C}$ ,  $I_n$  ( $n=1,2,3$ ), if the material is isotropic.

$$\begin{aligned} I_1 &= Tr(\mathbf{C}) \\ I_2 &= \frac{1}{2} \left( (Tr(\mathbf{C}))^2 - Tr(\mathbf{C}^2) \right) \\ I_3 &= \det(\mathbf{C}) \end{aligned} \quad (2.24)$$

The healthy arterial wall is generally heterogeneous, anisotropic, incompressible, nonlinear, and viscoelastic in its *passive* mechanical response (Bergel 1960; Carew, Vaishnav et al. 1968; Patel and Fry 1969; Holzapfel and Weizsacker 1998; Holzapfel, Gasser et al. 2000). The smooth muscle tone in arteries is regulated by several vasoactive substances and also by autonomic innervation. While a fully comprehensive mathematical representation of the artery would account for smooth muscle activity, such models are very complex and not well suited for mechanical analyses. For this reason,

nearly all characterizations of arterial tissue behavior consider arteries in their *passive* state.

Without detailed knowledge of the microstructure and anisotropy for the artery under consideration, especially if the vessel is actively remodeling, a heterogeneous and anisotropic constitutive relation is of limited use. True viscoelasticity is often not considered in the mechanical characterizations of arterial tissue, as significant preconditioning of the vessel, as would be achieved through cyclic loading *in vivo*, leads to a nearly repeatable elastic or “pseudoelastic” behavior (Fung, Fronek et al. 1979). Thus we chose to characterize the healthy portion of *passive* vessel wall in this work as an isotropic, homogeneous, incompressible, nonlinear, hyperelastic material.

In blood vessels, and many other biological tissues, collagen fibers are a primary source of material nonlinearity. In the unloaded and moderately loaded state, the collagen fibers within the artery wall are in a slightly “crimped” state, with the amount of crimping being non-uniform across fibers. A crimped collagen fiber has no appreciable stiffness in extension, and thus the early response of the artery in progressive loading is due to the elastin content of the wall. As the artery is further strained collagen fibers straighten out and, once straightened, are said to be “recruited” to the set of wall constituents providing structural stiffness. The monotonic recruitment during loading causes the strain-stiffening behavior exhibited by artery wall tissue.

In this work, we chose to model the vessel and plaque materials using the Demiray-type constitutive relation

$$W = D_1(e^{D_2(I_1-3)} - 1) \quad (2.25)$$

Because each material was assumed to be incompressible, there can be no dependence of  $W$  on  $I_3 = J^2$ , as the volume ratio is constrained to always be unity. Delfino tested seven freshly resected disease-free cadaveric common carotid artery segments, collecting pressure-internal radius and axial force-radius measurements at different axial stretches to determine  $D_1$  and  $D_2$  for the healthy carotid artery wall (Delfino 1996). Values of  $D_1$  and  $D_2$  for fibrous plaque tissue, and lipid pool, and calcification were taken from other studies (Loree, Grodzinsky et al. 1994; Loree, Tobias et al. 1994; Chau, Chan et al. 2004). Values of  $D_1$  and  $D_2$  are listed for the components of the diseased vessel wall in Table 2.3.

<b>Material</b>	<b><math>D_1</math> (Pa)</b>	<b><math>D_2</math></b>
Vessel Wall	2644.7	8.365
Fibrous Plaque	5105.3	13
Lipid Pool	50	5
Calcification	18,804.5	20

Table 2.3 Material parameters used to define vessel and plaque materials

The characterization of lipid pool and calcification as Demiray-type hyperelastic materials is artificial, but justifiable. These materials are almost fluid-like and exceedingly stiff, respectively. The product of  $D_1$  and  $D_2$  is related to the zero-strain stiffness for each material, and so we can see that calcification is about 17 times stiffer than the artery wall, which is in turn nearly 90 times stiffer than the lipid pool.

### 2.3.3 Material Properties of Blood

As already stated, this work assumes blood to be an incompressible Newtonian fluid. The assumption of constant viscosity is appropriate in many larger arteries where

regions of slow, recirculating flow are not expected to occur (Lee and Steinman 2007).

In this work,  $\rho_{\text{blood}}$  was taken to be  $1060 \text{ kg/m}^3$ , and dynamic viscosity was set at  $\mu = .0035 \text{ Pa s}$ .

## 2.4 Loading and Boundary Conditions

The artery wall is primarily loaded by the systemic pressure of circulating blood. Through the cardiac cycle, this pressure fluctuates between a systolic maximum and an end-diastolic minimum, with the fluctuation becoming less pronounced as the distance from the heart increases. A typical pressure waveform seen at the common carotid artery with a systolic peak near  $16 \text{ kPa}$  ( $120 \text{ mmHg}$ ) and an end-diastolic value near  $10 \text{ kPa}$  ( $80 \text{ kPa}$ ) is shown in Fig. 2.14.

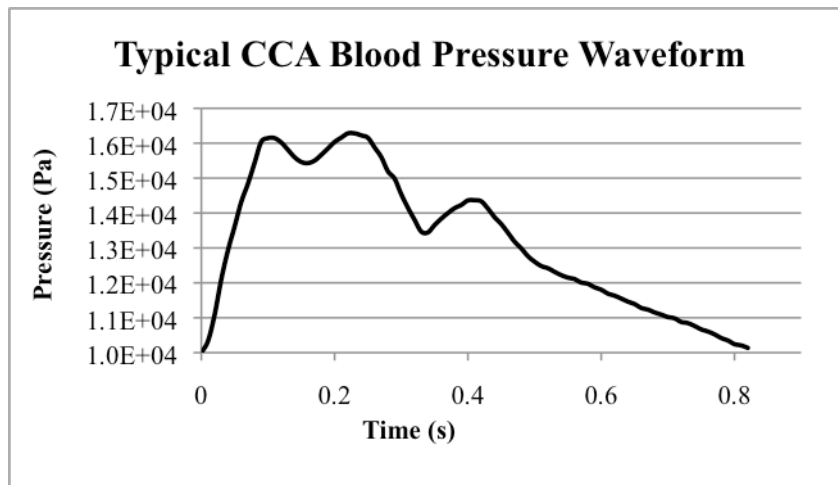


Fig. 2.14 Typical CCA pressure waveform, adapted from (Younis, Kaazempur-Mofrad et al. 2003)

Unfortunately, detailed pressure data within the vascular territory of interest is not typically available for a patient. Additionally, significant deviations from the proximal or distal systemic pressure may occur across a severe reduction in lumen area, as commonly

seen in advanced carotid disease (Tang, Yang et al. 1999; Tang, Yang et al. 2003). For this reason, a combination of pressure and flow boundary conditions were used to achieve vessel wall loading in our fluid-structure interaction models.

Flow data is usually sparse for a patient with carotid disease, often consisting of only a Doppler ultrasound study. Advanced imaging like phase-contrast MRI, while capable of measuring 2D or 3D velocity distributions in the artery with temporal resolution on the order of 30ms, is typically only done on a research-study basis for these patients. Doppler ultrasound is capable of measuring the full spectrum of flow velocities at a user-defined location within the artery throughout the cardiac cycle with 10ms time resolution. With limited assumptions on the nature of the flow field, this data can be used to construct inlet and outlet flow boundary conditions suitable for computational studies.

Doppler ultrasound data were used to construct inlet flow conditions at the CCA and outlet flow conditions at the ICA in our models. In a fluid-structure interaction model, pressure must be explicitly defined for at least one portion of the fluid boundary, and thus a pressure waveform was applied to the ECA outlet in our models.

#### **2.4.1 Construction of Patient-Specific Flow Boundary Conditions**

Doppler ultrasound can provide a velocity waveform at the location of the insonation volume with high temporal resolution. Typically, ultrasound technicians try to localize the region within the artery cross-section that demonstrates the highest peak systolic velocity. In a straight arterial segment this is the centerline velocity. If the flow were steady in the circulation, and the vessel were of constant circular cross-section, the flow profile across the artery would be parabolic, and the volume flow rate  $Q$  and

pressure drop  $\Delta P/\Delta L$  could be related to the centerline velocity  $u_{CL}$  through the Hagen-Poiseuille equation as

$$Q = \frac{u_{CL}}{2} \pi R^2 \quad (2.26)$$

$$\frac{\Delta P}{\Delta L} = \frac{4\mu u_{CL}}{R^2} \quad (2.27)$$

where  $R$  is the vessel radius, and  $\mu$  is the blood's dynamic viscosity. Blood flow is not steady, however, so reconstructing a flow-rate waveform using eq. 2.26 would introduce substantial error.

The analytical description of unsteady but periodic flow in a circular rigid-wall tube was provided by Womersley, and allows us to calculate the time dependent velocity profile across the artery given the waveform of the pressure gradient in the artery (Womersley 1955). He et al. showed that it is not necessary to know the pressure gradient waveform, and that the waveform of the flow rate or centerline velocity can also be used to calculate the flow profile (He, Ku et al. 1993). This is possible because the Fourier components that describe the periodic flow rate  $Q(t)$ , pressure gradient  $K(t)$ , and centerline velocity  $u_{CL}(t)$  are related by

$$\frac{K(\omega)\text{Re}}{i\alpha^2 J_0(i^{3/2}\alpha)} = \frac{Q(\omega)}{J_0(i^{3/2}\alpha) - \frac{2}{i^{3/2}\alpha} J_1(i^{3/2}\alpha)} = \frac{u_{CL}(\omega)}{J_0(i^{3/2}\alpha) - 1} \quad (2.28)$$

where  $\omega = 2\pi n$  is the normalized frequency at each mode  $n$ ,  $\text{Re} = \frac{2\rho u_{avg} R}{\mu}$  is the time

averaged Reynolds number of the flow,  $\alpha = \sqrt{n} R \sqrt{\frac{\rho \omega}{\mu}}$  is the Womersley number

multiplied by the square root of the Fourier mode number  $n$ ,  $i = \sqrt{-1}$ , and  $J_0$  and  $J_1$  are the zeroth and first order Bessel functions of the first kind.

Thus, if the centerline velocity waveform is known from Doppler ultrasound or the flow-rate waveform is known, we may calculate the velocity profile across the vessel by doing the following:

- 1 – Subtract the mean centerline velocity  $u_{avg}$  from  $u_{CL}(t)$  to obtain  $u'_{CL}(t)$ . If  $Q(t)$  is available, subtract the mean flow  $Q_{avg}$  from  $Q(t)$  to obtain  $Q'(t)$ .
- 2 – Perform a Fourier decomposition of  $u'_{CL}(t)$  ( $Q'(t)$ ) to obtain the complex Fourier coefficients  $u_{CL}(\omega_n)$  ( $Q(\omega_n)$ ) at a number of modes  $n=1,2,3\dots n_{max}$ .
- 3 - Use eqn. 2.28 to solve for the Fourier coefficients of the pressure gradient waveform  $K(\omega_n)$
- 4 – Calculate the time dependent portion of the velocity profile as originally shown by Womersley:



$$u(r,t) = \text{Real} \left[ \sum_{n=1}^{n_{\max}} \left( \frac{iR^2 K(\omega_n)}{\mu \alpha^2} \left[ 1 - \frac{J_0(i^{3/2} \alpha \frac{r}{R})}{J_0(i^{3/2} \alpha)} \right] e^{in\omega_0 t} \right) \right] \quad (2.29)$$

5 - Add to eq. 2.29 the steady-state velocity profile as determined by the Hagen-Poiseuille equation. The sum is the full time dependent velocity profile.

$$u_{ss}(r) = 2u_{avg} \left[ 1 - \left( \frac{r}{R} \right)^2 \right] \quad (2.30)$$

where  $u_{avg}$  is either known from the ultrasound data, or can be calculated from  $u_{avg} = Q_{avg}/(\pi R^2)$ .

Codes were written in MatLab (The Mathworks, Natick, MA) to perform steps 1-5 above, and are provided in the appendix. Of course, we should not expect that the artery is precisely circular in cross-section. A method to map the Womersley profile to a non-circular geometry will be presented in a later section. If phase contrast MRI data is available for the patient, it may be used to establish flow boundary conditions either by integrating a flow rate and constructing a Womersley profile, or by interpolating the measured velocity field so that it can be applied directly to the model geometry.

### 2.4.2 Pressure Boundary Condition

Identifying an appropriate pressure boundary condition for arterial flow problems is an immense challenge. When the distensibility of the artery is accounted for, the flow and pressure waveforms set up a propagating wave that travels down the artery. Due to changes in the geometry of distal vessels, such as bifurcations or dramatic reduction in vessel caliber, the propagating wave is partially reflected back toward the heart. The fluid-structure interaction arterial flow problem is thus one of forward and backward propagating pressure waves. Because our entire geometry lies within the conducting circulation, it is not appropriate to specify a static pressure boundary condition at the outlet of the ECA. If a blood pressure waveform is available for the patient, it may be applied at the outlet of the ECA, and the pressure at the proximal CCA will then be determined through the flow boundary conditions and the Navier-Stokes equations. In the absence of patient-specific pressure data, a realistic pressure waveform can be applied such that the peak systolic and end diastolic pressures at the proximal CCA are within the physiological range.

### 2.4.3 Vessel Displacement Boundary Conditions

In this work, cylindrical coordinate systems  $(\hat{\rho}, \hat{\phi}, \hat{z})$  were defined at the CCA inlet and ICA and ECA outlets. For each of the three reference frames, the  $\hat{z}$  axis was defined to coincide with the local lumen centerline. Because of the geometry preparation explained in section 2.1.6, the inlet and outlet surfaces lie normal to the local  $\hat{z}$  axis. Each inlet and outlet surface was constrained in the  $\hat{z}$  direction, allowing for in-plane expansion and contraction only.

## **2.5 Geometric Discretization**

In the finite element methods, a region of space is represented as a set of smaller partitions known as elements. The region of space may be fully occupied by a particular body, in which case the elements collectively represent materials in the Lagrangian frame. Alternatively, the set of elements may describe a spatial domain independent of its occupation, providing an Eulerian representation for field problems. An intermediate frame known as Arbitrary Lagrangian Eulerian (ALE) is also useful to describe an Eulerian problem with deforming boundaries.

The numerical details of geometric discretization in finite element methods are well covered in many texts, and for a comprehensive presentation the reader is referred to the works of Zienkiewicz and Taylor and Farrashkhalvat (Zienkiewicz and Taylor 2000; Farrashkhalvat and Miles 2003). For the present section, it will suffice to discuss the four main requirements of a finite element mesh suitable for image-based fluid-structure interaction models of diseased arteries.

### **2.5.1 Basic Requirements for Finite Element Mesh of Multi-Component Arterial Models**

First, just as it was important in section 2.1 to make an accurate geometric representation of the segmented image data, it is important to discretize those geometries in such a way that their size, shape, and curvature are well-preserved. Second, it is also important that the connectivity of the plaque and vessel components is maintained. As shown in Fig. 2.12, the materials of the vessel wall and plaque are form-fitting to each other, with no gaps between materials. In the finite element model, we assume that

different materials obey a “no-slip, no-penetration” condition at their shared boundaries. In terms of mesh construction, this condition is automatically fulfilled if the elements defining each material share nodes at the boundary. An example of a “node-matched” finite element mesh is shown in Fig. 2.15 for a simple 2D geometry with vessel wall (green), fibrous plaque (red), and lipid pool (purple).

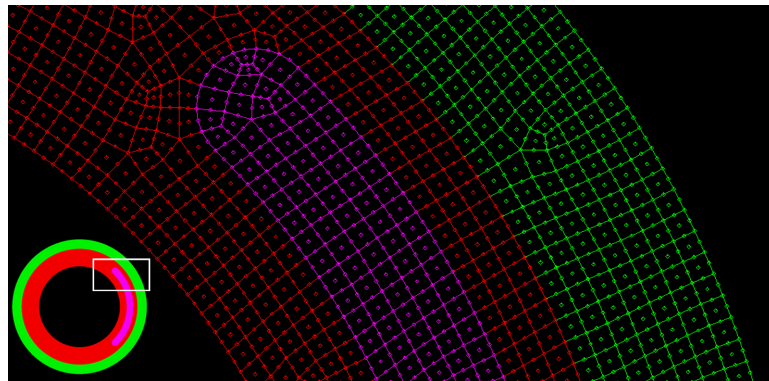


Fig. 2.15 Simple 2D geometry and zoom-in on mesh showing node matching at material interfaces. Green = vessel wall, Red = fibrous plaque, Purple = lipid pool.

Third, it is important that we have robust control over the local and global element density. Having too few elements in regions of strong stress gradients will result in a poor resolution of the local stress field, potentially altering conclusions drawn from the finite element model. Conversely, having too many elements in the finite element model can lead to a dramatic increase in computation time, and may even make the model prohibitively large given constrained computing resources. Finally, the elements themselves should be of good quality. For 3D elements, element angles should not be excessively small ( $< 20^\circ$ ) or large ( $> 145^\circ$ ), and elements should not have edge length

ratios too great, as this will lead to pronounced error in the numerical calculations within the neighborhood of the element, and could even cause a divergent calculation.

While not a strict requirement, it is helpful to be able to generate the finite element mesh quickly. In this way, alterations to the geometry, loading, or boundary conditions can be made without spending a great deal of time to adapt the mesh accordingly.

A volumetric finite element mesh can be structured, unstructured, or a combination of the two. A structured mesh consists of hexahedral “brick” elements arranged in an ordered, node matching fashion, and has clear advantages over an unstructured mesh in terms of accuracy and computational efficiency. An unstructured mesh generally consists of tetrahedral elements, and is less accurate than a structured mesh given the same number of elements. The unstructured mesh can be generated automatically for nearly any geometry with commercial meshing codes, while only the simplest shapes can be automatically meshed in a structured fashion.

The geometries shown in section 2.1.4 are not amenable to structured mesh generation. Faithful representation of the complex shapes necessitates either a great number of elements or higher order elements with curved boundaries, which would significantly increase computational cost. Node-matching must be achieved manually either through careful element design or laborious partitioning of the geometries into simple shapes. Additionally, the local avoidance of distorted elements and adjustment of local element densities requires tedious re-design of the global mesh. Thus, a structured mesh is difficult and time-intensive to construct, and is not easily modified once made.

In light of these challenges, and in consideration of the four major requirements of a suitable mesh, we have based our geometric discretization on an unstructured

tetrahedral finite element mesh. The unstructured mesh can be generated automatically, and given appropriate input, the mesh generator can directly ensure accurate representation of complex geometries, node-matching boundaries, robust element density control, and high quality elements. Furthermore, modifications to the mesh can be made locally, without effecting global discretization.

### 2.5.2 Construction of the 3D, Multi-Component Finite Element Mesh

This section will explain, in detail, how we generated the computational meshes for our 3D FSI models. All mesh generation for the work presented here was done using the commercial mesh generator HyperMesh (Altair Engineering, Troy, MI).

The goal is to create a set of node-matched volumetric meshes from the NURBS boundary surfaces of the vessel lumen, lipid pool, fibrous plaque, and outer vessel wall as constructed in section 2.1 (see Fig. 2.16). Two approaches are possible: in one, a set of intermediate solid entities is defined and then meshed; in the other, volume meshes are based on a set of “air-tight” triangular surface meshes. The second approach is used here, as it affords greater user control over local element density.

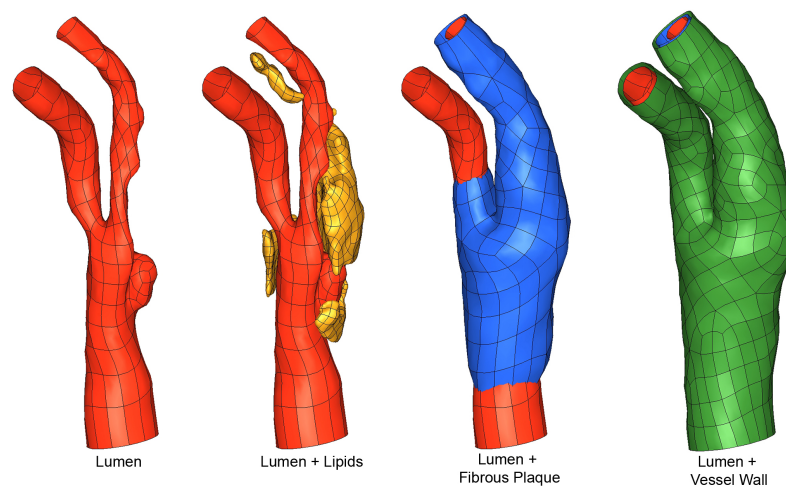


Fig. 2.16 NURBS surface representations for vessel and plaque component boundaries.

Before mesh generation was begun, a few geometric operations were made on the set of surfaces in Fig. 2.16. At the inlet and outlets of the bifurcation the lumen, fibrous plaque and outer vessel wall surfaces were used to create “end-cap” surfaces that represent the thickness of vessel wall and fibrous plaque one would observe if the real diseased artery were cut transversely at those locations. The edges these surfaces share with the lumen, plaque and wall were forced to have the same definition so that the surface junctions were sealed. The end cap surfaces for the ICA are shown, before and after forced edge sharing, in Fig. 2.17, where the names of each surface are given.

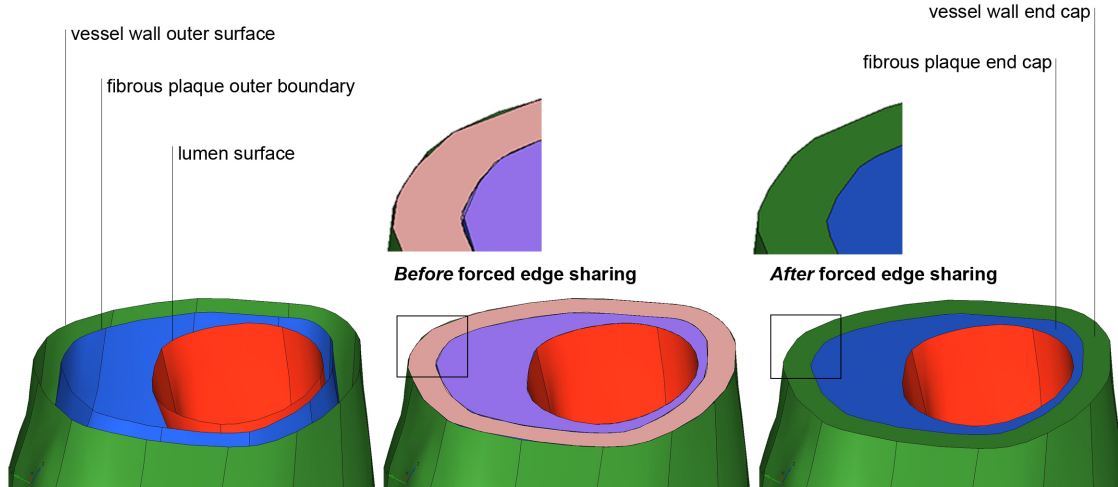


Fig. 2.17 Left to right: Surfaces from section 2.1, end cap surfaces generated to seal vessel and plaque components at vessel boundary, end caps after forced edge sharing to make geometries “air tight”.

Next, the lumen and fibrous plaque surfaces were used as cutting surfaces to trim each other in regions of the CCA and ECA where they overlap. This operation divides the original surfaces at the curves defining the surface intersection. The curves resulting from the mutual trimming were also forced to have the same definition, as shown in Fig. 2.18. Portions of the fibrous plaque surface within the lumen were discarded, and the

lumen and fibrous plaque surfaces, and the fibrous plaque end cap at the ICA outlet then defined a closed volume in which fibrous plaque and lipid pool lay.

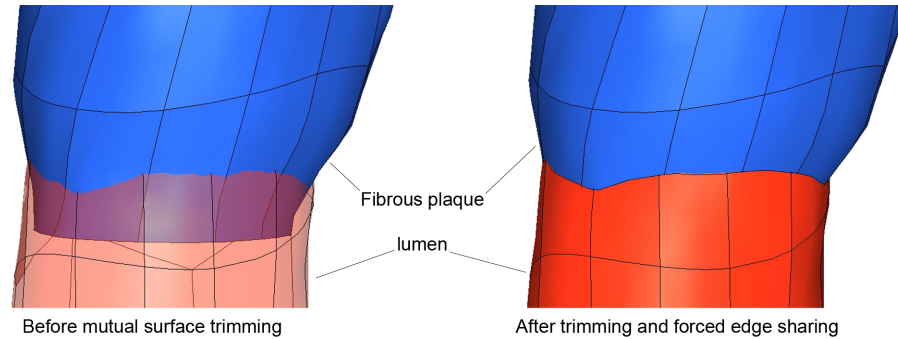


Fig. 2.18 Mutual trimming of lumen and fibrous plaque bounding surfaces. Note how the initial fibrous plaque surface is designed to cross the lumen so the trimming and forced edge sharing can create an “air tight” junction.

At this point, all the surfaces and shared edges needed to define “air-tight” geometrical bodies were available. The fibrous plaque body contains lipid pool bodies, and was thus described by external and internal bounding surfaces. The sets of surfaces defining each body are listed in Table 5.

<b>Body</b>	<b>External Bounding Surface(s)</b>	<b>Internal Bounding Surface(s)</b>
Blood Volume (fluid domain for FSI)	Lumen, lumen cut planes at ECA, ICA, and CCA	none
Fibrous Plaque	Fibrous Plaque, Lumen Internal to Fibrous Plaque, Fibrous Plaque cut plane at ICA	Large Lipid Pool, Small Lipid Pool
Vessel Wall	Lumen not Internal to Fibrous Plaque, Fibrous Plaque, Vessel Wall cut planes at CCA, ICA, and ECA	none
Large Lipid Pool	Large Lipid Pool	none
Small Lipid Pool	Small Lipid Pool	none

Table 2.4 Bounding surfaces for each solid material in vessel wall



As shown in Fig. 2.16, the NURBS representation of each bounding surface consists of a set of quadrilateral “patches” with shared edges. If the surfaces are left as is, automatic mesh generators will use these patches as seed points for the mesh, ensuring that finite element nodes are placed at each vertex and along each edge. It is preferable to force the mesh generator to place nodes at locations that support an ideal mesh density distribution. For instance, in plaque mechanics the stress field within the thickness of the fibrous plaque overlying a lipid pool is of primary interest. As compared to regions that are of no particular interest, the fibrous plaque overlying the lipid pool should be discretized using a larger number of elements to give more accurate stress predictions. To achieve this, the patches of each NURBS surface were all joined into one surface that was then partitioned according to our desired mesh density scheme. Partitioning of the unabridged surface was achieved by defining curves that were used in a trimming operation on the surface. With respect to the fibrous plaque layer, both external and internal bounding surfaces needed to be properly partitioned. As the partitioned surfaces were to be used for mesh generation, border zone partitions were defined surrounding each region of interest so that mesh density would be smoothly varying across the surfaces and distorted elements would be avoided. 3-node triangular surface meshes were generated on the partitioned surfaces with local density reflecting the accuracy required in the predicted stress field. A representative surface meshing procedure is shown in Fig. 2.19. Higher order elements with mid-side nodes could be used in surface mesh generation, allowing an exact curvature match between geometry and element. The reason for using linear elements will be discussed in the explanation of our volume meshing procedure.

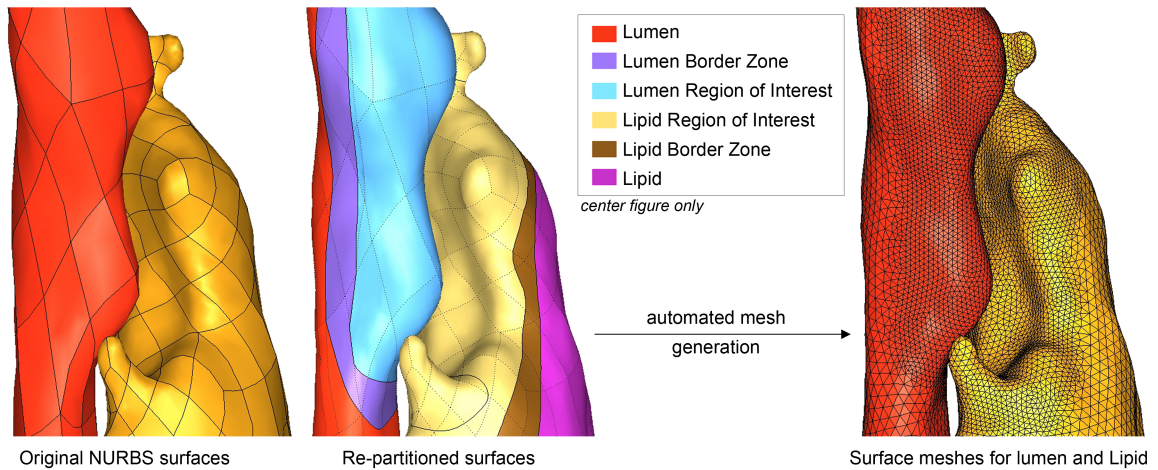


Fig. 2.19 Re-partitioning of NUBRS surfaces and surface meshes for lumen and lipid pool.

Because contacting surfaces meet at shared edges in these models, the discretization of each surface naturally conforms to that of the other. This allows easy generation of closed surface meshes of the internal and external boundaries of each body. To create a volume mesh for a particular body the bounding triangular surface mesh(es) of the body, as listed in Table 5, were selected as input for tetrahedral mesh generation. The space-filling tetrahedral mesh adopts a local density based on an interpolation of nearby surface mesh densities. By forcing the volume mesh to conform to all of the surface meshes previously generated, volume meshes of abutting bodies necessarily shared their boundary nodes. 4-node tetrahedral meshes were constructed for the vessel wall, fibrous plaque, and lipid pools. The 4-node tetrahedral meshes were then converted to 10-node tetrahedral meshes, constraining mid-side nodes to lie precisely at the edge midpoint and edges to remain straight upon conversion.

The volume meshes were initially formed from linear tetrahedra to ensure that the Jacobian ratio of each element was 1.0. The Jacobian ratio is a measure of element distortion, and if it becomes too small, will cause numerical error and terminate a finite

element calculation. By starting with the best possible Jacobian ratio, the likelihood of calculation-terminating element distortion is greatly reduced.

A representative multi-component volume mesh, cut open for visualization purposes, is shown in Fig. 2.20.

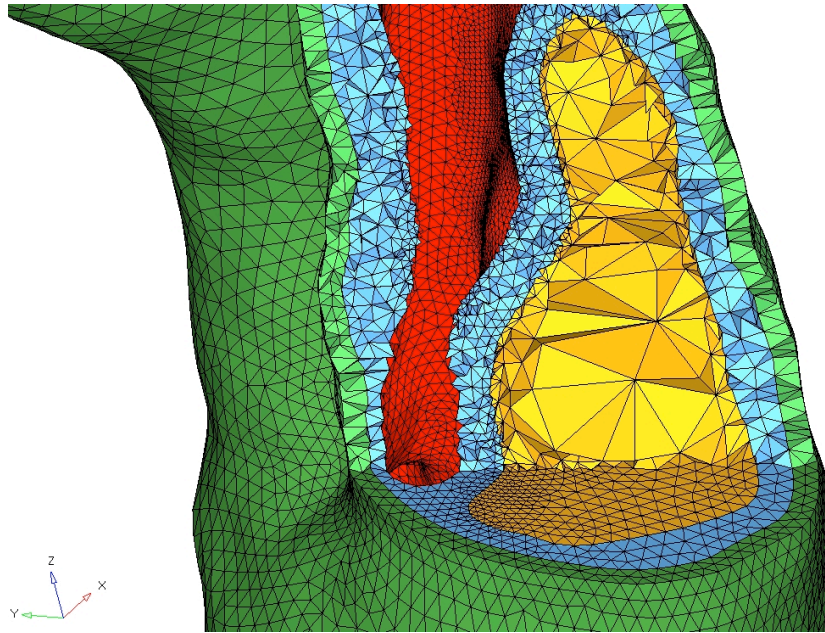


Fig. 2.20 Cut-open view of multi-component volume mesh. Green = vessel wall, Blue = fibrous plaque, Yellow = lipid pool, Red = lumen surface. Note the large elements within the lipid pool. The stress gradients in this material are extremely small, and thus do not warrant high element density.

A linear tetrahedral mesh of the fluid domain was made using the same procedures outlined above, without the constraint of a node-matching lumen surface boundary.

## 2.6 Finite Element Representation of Physics

### 2.6.1 Solid Domain FEM

The equation of motion for the solid domain, eq. 2.7, is nonlinear due to the material response and large deformation of the vessel wall. In order to accommodate these nonlinearities, as well as the structure-following loads (the systemic pressure always acts *normal* to the deforming wall) an incremental finite element method must be used. In this class of methods, the primary variables are increments in the nodal displacements of the discretized bodies, and equilibrium iterations are performed to achieve the cumulative nodal displacements. This makes our analysis lengthier and more demanding than a linear analysis, in which nodal displacements may be solved for without iteration. The assumption of material incompressibility further complicates the analysis, as robust and well-characterized displacement-based finite element methods cannot provide accurate stress predictions. Thus, a multi-field finite element formulation, in which the primary variables include stress and/or strain in addition to the standard displacements, must be employed. In this work, the commercial finite element code ADINA (ADINA R&D, Inc. Watertown, MA) was used to solve the equation of motion for the solid domain, using an incremental, mixed u/p finite element formulation.

In the mixed u/p finite element formulation, primary variables are the increments of both nodal displacements and element pressures, which are interpolated separately. The finite element equations can be derived starting from a variational statement of eqn. 2.7 that exploits the principle of virtual work,

$$\delta \left[ \int_V (\bar{W} + Q) dV \right] = R \quad (2.31)$$

where  $R$  is the external virtual work, and  $\bar{W}$  is the strain energy density function of eq. 2.25 written in terms of the reduced invariant  $J_1 = I_1 I_3^{-1/3}$  so that  $\bar{W}$  is strictly deviatoric.  $Q$  is an additional potential that accounts for the internal energy due to the interpolated pressure  $\tilde{p}$ , and for an isotropic material,

$$Q = \frac{-1}{2\kappa} (\bar{p} - \tilde{p})^2 \quad (2.32)$$

where  $\bar{p} = -\kappa(J_3 - 1)$ , with  $J_3 = \det(\mathbf{F})$ , is the element pressure computed directly from nodal displacements.

$\bar{W}$  can be written as the product of the 2<sup>nd</sup> Piola-Kirchoff stress tensor and the Green-Lagrange strain tensor (see (Bathe 1996)), thus framing eq. 2.31 in terms of material strains. Identification of appropriate interpolation functions for the element incremental displacement allows us to construct the governing incremental equations for each element of the discretization given in section 2.5. For each element, we have

$$\begin{bmatrix} {}^t K_{UU} & {}^t K_{UP} \\ {}^t K_{PU} & {}^t K_{PP} \end{bmatrix} \begin{bmatrix} \hat{u} \\ \hat{p} \end{bmatrix} = \begin{bmatrix} {}^{t+\Delta t} R \\ 0 \end{bmatrix} - \begin{bmatrix} {}^t F_U \\ {}^t F_P \end{bmatrix} \quad (2.33)$$

where  $\hat{u}$  and  $\hat{p}$  are the incremental displacements and pressures at the element's nodes.  $R$  is the vector of nodal point forces on the element. The full form of each contribution to the stiffness matrix, and the forms of  ${}^tF_U$  and  ${}^tF_P$  can be found in (Bathe 1996).

Because eq. 2.32 applies at an elemental level, the pressure  $\hat{p}$  are condensed out of the global equation system at an elemental level, and the global finite element equations resulting from assembly of eq. 2.33 were solved incrementally using Newton iteration in the following way

1 – Solve for  $\hat{p}$  in terms of  $\hat{u}$  using

$$\hat{p} = K_{PP}^{-1} (-F_P - K_{UP}^T \hat{u}) \quad (2.34)$$

2 – Substitute eq. 2.34 for  $\hat{p}$  in

$$K_{UU} \hat{u} + K_{UP} \hat{p} = R - F_U \quad (2.35)$$

3 – Assemble element-level equations of the form given in eq. 2.35, and solve global system for  $\hat{u}$ .

4 – Use eq. 2.34 and solution of  $\hat{u}$  from step 3 to solve for  $\hat{p}$  at the element level.

5 – Check for convergence using energy or displacement increment tolerances. If converged, end calculation. If not converged, update stiffness and force terms in eq. 2.33 and iterate again, starting at step 1.

In the dynamic analyses performed in this work, eq. 2.33 is modified to contain the inertial terms associated with the element mass matrix, and the dynamic system is solved by embedding steps 1-5 above in an outer iteration for implicit time integration. The time integration was handled using the backward Euler method with  $\alpha = 1$ , and nonlinearity was handled using full Newton iterations with update of the tangent stiffness matrix at each iteration. The use of the first-order time accurate backward Euler method was motivated by the fact that the dynamic analyses performed were FSI simulations. The standard Newmark method with  $\delta = \frac{1}{2}$  and  $\alpha = \frac{1}{4}$  is second order accurate in time, but is unstable for the velocities encountered in the fluid system. 10- and 11-node isoparametric tetrahedra were used to discretize the solid domain, allowing quadratic interpolation of displacement and piecewise constant pressure  $\hat{p}$  on each element.

## 2.6.2 Fluid Domain FEM

The coupling of the pressure field and flow field dictates that in the numerical representation of the flow problem, pressure conditions cannot be explicitly stated. The relative magnitudes of the normal viscous stresses and pressure make it appropriate to state our pressure boundary condition as a normal stress condition. Thus, in the numerical statement of the flow problem, the fluid stress tensor of eq. 2.10 is substituted back into eq. 2.11 so that the Navier Stokes equations for incompressible, isothermal blood flow in the absence of body forces read

$$\begin{aligned} \rho \left[ \frac{\partial \vec{v}}{\partial t} + (\vec{v} \cdot \nabla) \vec{v} \right] - \nabla \cdot \sigma &= 0 \\ \nabla \cdot \vec{v} &= 0 \end{aligned} \tag{2.36a,b}$$

The flow boundary conditions employed, as described in section 2.4 are

$$\begin{aligned} \bar{v} &= \bar{y} \text{ for } x \in \{CCA_{Inlet}, ICA_{Outlet}\} \\ \sigma_{nt} &= 0, \sigma_{mn} = s \text{ for } x \in \{ECA_{Outlet}\} \end{aligned} \quad (2.37)$$

where  $\bar{y}$  is the prescribed velocity field,  $\sigma_{nt}$  and  $\sigma_{mn}$  are shear and normal components of the fluid stress tensor, and  $s$  is the prescribed normal traction approximated to be the prescribed pressure boundary condition. As mentioned in section 2.2.3, there are additional boundary conditions that must be satisfied in the ALE formulation of the FSI problem. For the present explanation of the numerical approach to solution of the Navier-Stokes equations, we may simply consider a no-slip condition at the vessel wall, which can be absorbed into 2.37 as  $\bar{v} = \bar{y}$  for  $x \in \{CCA_{Inlet}, ICA_{Outlet}, vessel\ wall\}$ .

The weak formulation of eqs. 2.36a,b used in ADINA is obtained using the standard Galerkin approach. First, eqs. 2.36a and 2.36b are multiplied by test functions  $\bar{u} = (u_1, u_2, u_3)^T$  and  $q$ , respectively, which are virtual velocities and pressure, and the products are integrated over the fluid domain  $\Omega$ . The resulting integral term containing  $(\nabla \cdot \sigma)$  is then integrated by parts to obtain an integral term over the fluid domain boundary and an integral over the domain volume requiring weaker continuity of  $\sigma$ . After application of our boundary conditions 2.37, we arrive at the weak form of the Navier-Stokes equations for the blood flow problem:

*Find  $\bar{v}$  and  $p$ , with  $\bar{v} = \bar{y}$  for  $x \in \{CCA_{Inlet}, ICA_{Outlet}, vessel\ wall\}$ , such that*



$$\begin{aligned}
& \int_{\Omega} \rho \frac{\partial \bar{\mathbf{v}}}{\partial t} \cdot \bar{\mathbf{u}} d\Omega + \int_{\Omega} \mathbf{T} \cdot \nabla \bar{\mathbf{u}} d\Omega + \int_{\Omega} \rho (\bar{\mathbf{v}} \cdot \nabla \bar{\mathbf{v}}) \bar{\mathbf{u}} d\Omega - \int_{\Omega} p (\nabla \cdot \bar{\mathbf{u}}) d\Omega = \int_{ECA_{Outlet}} s(\bar{\mathbf{u}} \cdot \hat{\mathbf{n}}) dECA_{Outlet} \\
& \int_{\Omega} q (\nabla \cdot \bar{\mathbf{v}}) d\Omega = 0
\end{aligned} \tag{2.38a,b}$$

for all  $\bar{\mathbf{v}}$  such that  $\bar{\mathbf{v}} = 0$  for  $x \in \{CCA_{Inlet}, ICA_{Outlet}, vessel\ wall\}$ ,  $\mathbf{T}$  given by eq. 2.12, and  $\hat{\mathbf{n}}$  is the unit vector normal to the ECA outlet surface.

After identification of appropriate interpolation functions for the element velocities and pressure and the test functions of eq. 2.38, the finite element equations for nodal velocities  $\hat{\mathbf{v}}$  and pressures  $\hat{p}$  at the element level are given by

$$\begin{aligned}
\mathbf{M}_v \hat{\mathbf{v}} + (\mathbf{K}_{mvv} + \mathbf{K}_{vv}) \hat{\mathbf{v}} + \mathbf{K}_{vp} \hat{p} &= \mathbf{R}_S \\
\mathbf{K}_{vp}^T \hat{\mathbf{v}} &= 0
\end{aligned} \tag{2.39}$$

where the components of the element mass and stiffness matrices,  $\mathbf{M}$  and  $\mathbf{K}$  and the element load vector,  $\mathbf{R}$ , are given in (Bathe and Dong 1987). In ADINA, the finite element equations are constructed at the element level using the standard Galerkin formulation. After analytical integration of the terms in eq. 2.39, the test functions  $\bar{\mathbf{u}} = (u_1, u_2, u_3)^T$  are modified at an element level based on the local Peclet number as evaluated along the streamlines within the element. This is similar to the Petrov-Galerkin approach, and amounts to the imposition of an artificial diffusion in the flow direction.

The global system of equations resulting from assembly of element equations of the form given in eq. 2.39 is inherently nonlinear due to the convective term in the Navier-Stokes equations. The linearized global system is solved using a direct sparse solver, and the solution of the nonlinear system is reached through Newton-Raphson

iteration. As mentioned in section 2.6.1, time integration is performed using the backward Euler method. 4-node tetrahedra were used to discretize the fluid domain in our work, providing a linear interpolation of velocity over the element, and piecewise constant pressure.

### 2.6.3 Fluid-Structure Interaction

The fluid-structure interaction in our models was handled using a partitioned method, in which the fluid and solid domains are solved independently and FSI boundary conditions of section 2.2.3 are enforced in an outer iteration. The fluid and solid meshes are not required to match at the FSI boundary, and determination of appropriate fluid mesh displacements is accomplished by interpolation of solid mesh displacements  $\mathbf{d}_s$ . The fluid stresses  $\sigma_f$  are integrated on the solid domain FSI interface to provide the fluid force  $F(t)$  loading the solid

$$F(t) = \int \sigma_f \cdot dS \quad (2.40)$$

The finite element equations of the coupled system are written as

$$\begin{bmatrix} A(\mathbf{X}_f, \mathbf{d}_s(\mathbf{X}_s)) \\ A(\mathbf{X}_s, \sigma_f(\mathbf{X}_f)) \end{bmatrix} = 0$$

where  $A(\mathbf{X}_f, \mathbf{d}_s(\mathbf{X}_s))$  are the fluid equations based on fluid solution vector  $\mathbf{X}_f$  and displacements of the solid domain  $\mathbf{d}_s(\mathbf{X}_s)$ .  $A(\mathbf{X}_s, \sigma_f(\mathbf{X}_f))$  are the solid equations based on solid solution vector  $\mathbf{X}_s$  and fluid stresses  $\sigma_f(\mathbf{X}_f)$ . In practice, to reliably achieve

convergence in large displacement dynamic systems, the passage of displacements and loads between domains is relaxed by  $\lambda_s$  and  $\lambda_f$ , respectively.

In the partitioned method, strong coupling between the fluid and solid domains is accomplished by iterating the following scheme

For FSI iteration  $n=1,2,3\dots$

1.) Solve  $A(\mathbf{X}_f^n, \lambda_s \mathbf{d}_s^{n-1} + (1 - \lambda_s) \mathbf{d}_s^{n-2}) = 0$

2.) Compute fluid forces using eq. 2.4

3.) Solve  $A(\mathbf{X}_s^n, \lambda_f \sigma_f^n + (1 - \lambda_f) \sigma_f^{n-1}) = 0$

4.) Interpolate solid mesh displacement to evaluate fluid mesh displacement, using

relaxed displacement  $\mathbf{d}_f^n = \lambda_s \mathbf{d}_s^n + (1 - \lambda_s) \mathbf{d}_s^{n-1}$

5.) Check convergence of FSI iterations using both stress and displacement

convergence criteria

$$\frac{\|\sigma_f^n - \sigma_f^{n-1}\|}{\max\{\|\sigma_f^n\|, 10^{-8}\}} \leq \varepsilon_\sigma \quad (2.41a,b)$$

$$\frac{\|\mathbf{d}_s^n - \mathbf{d}_s^{n-1}\|}{\max\{\|\mathbf{d}_s^n\|, 10^{-8}\}} \leq \varepsilon_d$$

if convergence is achieved, save results and move to the next time step of the problem. If convergence is not met, go back to step 1

In this work, relaxation parameters of  $\lambda_s = 0.85$  and  $\lambda_f = 0.85$  were chosen to ensure easy convergence without performing unnecessary FSI iterations. The values were selected on the basis of smaller-scale FSI simulations using similar geometries, loads, and material formulations. The convergence criteria  $\epsilon_\sigma$  and  $\epsilon_d$ , were both chosen to be 0.1.

## 2.7 Finite Element Representation of Flow Boundary

### Conditions

Prescription of a Womersley flow profile at the inlet of the CCA is helpful to establish realistic boundary conditions in flow simulations of truncated portions of the carotid bifurcation (Moyle, Antiga et al. 2006). The strategy presented in section 2.4.1 allows us to generate a Womersley profile for a circular artery based on Doppler US measurements of the centerline velocity, or phase contrast MRI data integrated to provide a flow rate waveform. The typical arterial cross-section is not precisely circular, although it is often a reasonable approximation. Rather than extend the fluid domain of our models to a circular cross-section, which would be artificial and increase computational effort, we have chosen to linearly map a Womersley profile to the lumen inlet geometry measured *in vivo*. In the discretized representation of the flow domain, this amounts to prescribing a velocity waveform to each CCA inlet node consistent with the Womersley profile of a circular artery with the same cross-sectional area.

The following is a brief description of the process by which we mapped Womersley profiles to the CCA inlet nodes. The procedure and the computer programs written to perform the mapping were constructed with no restrictions on the flow domain

of the problem. In this way, any lumen shape positioned at any orientation in the global reference frame may be assigned a Womersley velocity profile with minimal user input. Additionally, the method and computer programs are insensitive to the design of the computational mesh employed. For the remainder of this section a representative CCA inlet mesh, as shown in Fig. 2.21, will be used to explain the mapping procedure.

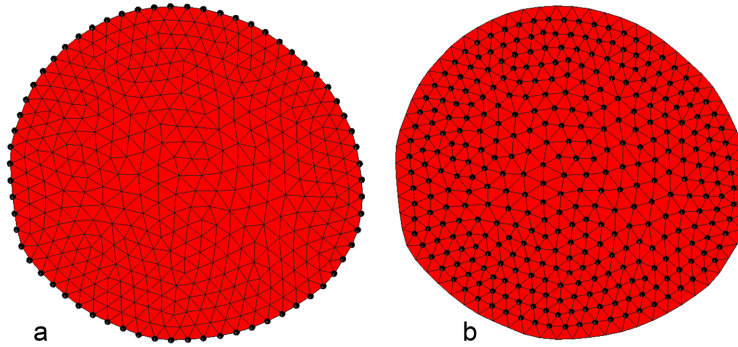


Fig. 2.21 Example of mesh used at CCA inlet. a.) boundary nodes b.) nodes for mapping

The mesh information required is the following: the position of each node in the global reference frame, the position of the inlet centroid in 3-dimensions  $(x_c, y_c, z_c)$ , the node numbers identifying boundary nodes. The vector  $\hat{n}$  normal to the inlet mesh

(pointing into the lumen), and the equivalent circular radius  $r_C = \left( \frac{Area_{inlet}}{\pi} \right)^{1/2}$  are also

needed, and are easily determined during the geometrical modeling of section 2.1.6.

First, the nodes are translated in 3 dimensions so that  $(x_c, y_c, z_c) = (0, 0, 0)$  in the global reference frame. Next, using  $\hat{n}$  and the vector  $\vec{v}_1$  from the centroid to any of the boundary nodes, the Euler angles  $(\alpha, \beta, \gamma)$  describing the inlet mesh orientation in the global frame are identified. Choice of this boundary node determines the set of Euler angles derived, but different descriptions of orientation are of no consequence. The Euler

angles are then used to construct the transformation matrix  $\mathbf{R}(\alpha, \beta, \gamma)$  that rotates the mesh so that  $\hat{n}$  is aligned to the global  $\hat{z}$  axis (see Fig. 2.22). With the mesh transformed into the global  $x$ - $y$  plane, the remaining mapping problem is 2-dimensional.

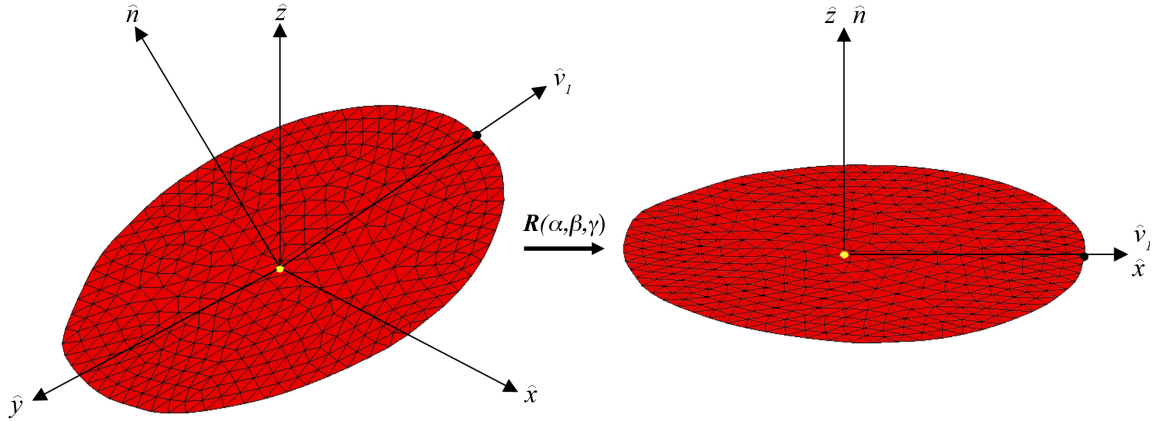


Fig. 2.22 Inlet mesh before and after transformation to align surface normal to global  $\hat{z}$  axis. The yellow point is the mesh centroid.

For each node  $i$ , its transformed  $(x_i, y_i)$  position in the global  $x$ - $y$  plane determines its angular position with respect to the global  $x$  axis, and allows us to construct a 2D rotation matrix that places it at  $y = 0$  in the  $+x$  direction. The same rotation matrix is applied to all boundary nodes, and the boundary nodes are sorted according to their distance from the  $x$ -axis in the rotated frame. The two boundary nodes closest to the  $x$ -axis, lying in the  $+x$  half of the plane are determined, and the average of their distances from the centroid is recorded as the “equivalent radius”,  $r_E$ , for node  $i$ . Node  $i$  is then

assigned the velocity waveform corresponding to radius  $r = \frac{d_i}{r_E} r_C$  in the axisymmetric

Womersley profile, where  $d_i$  is the distance from node  $i$  to the mesh centroid (see Fig.

2.23). Boundary nodes are assigned a zero velocity, consistent with the no-slip condition.

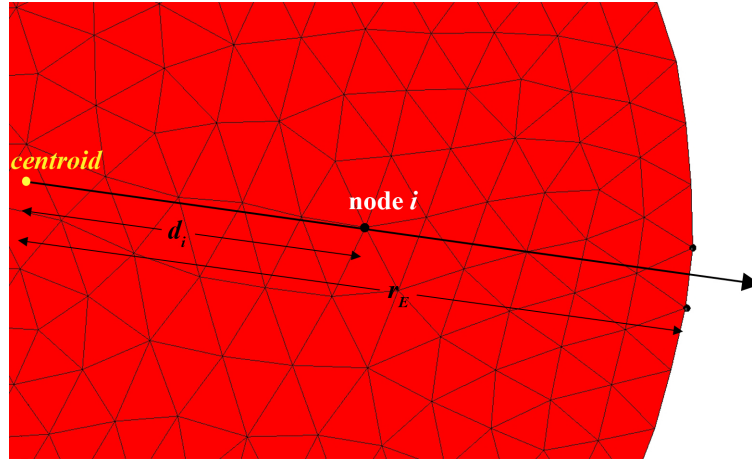


Fig. 2.23 Equivalent radius  $r_E$ , and distance from centroid  $d_i$  for node  $i$ . The two boundary nodes closest to the  $+x$  axis in the rotated frame are shown highlighted in black.

Mapping the Womersley profile is an approximation, and the accuracy with which the profile represents the desired flow rates depends on the mesh density at the inlet plane. If the mesh is too coarse, the flow profile will not be resolved well enough to be accurate. To understand this dependence on mesh density, a series of three flow simulations was performed on a circular cylinder, where the error in numerically measured flowrates should approach zero as mesh density increases. The test cylinder was 0.4 cm in radius and 3cm long. The flow rate waveform and inlet meshes used in this sensitivity analysis are shown in Figs. 2.24 and 2.25, respectively. The flow-rate waveform was measured for a patient with slight internal carotid artery stenosis (estimated to be 20%) using phase contrast MRI. There were 8 elements in the flow direction for each simulation. To limit the influence of initial transients in the simulated flows, each simulation was initialized with the solution of a steady-state flow simulation corresponding to the Womersley velocity profile at the beginning of the full time-dependent waveform.

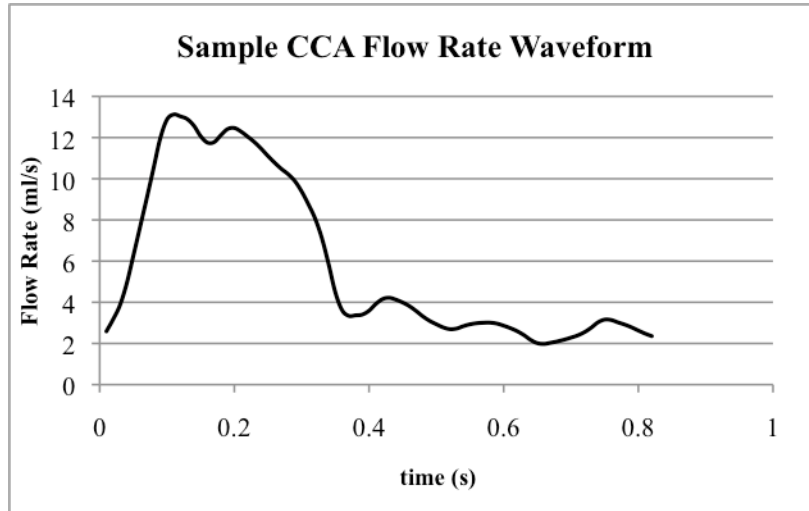


Fig. 2.24 Flow rate waveform used in mesh sensitivity test of Womersley mapping.

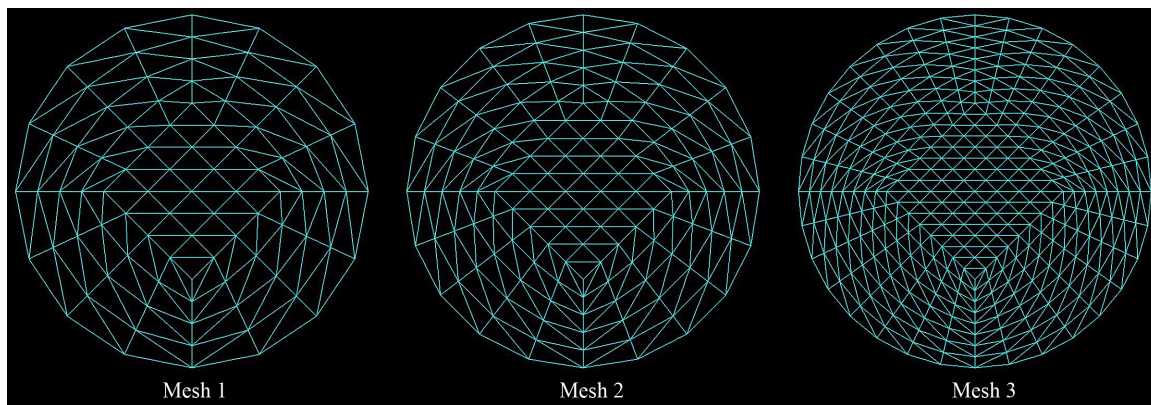


Fig. 2.25 Computational meshes used at the inlet to the flow tube for Womersley mapping sensitivity analysis. Mesh 1 has 160 elements at the inlet surface, mesh 2 has 250 elements, mesh 3 has 640 elements.

The flow rate was measured halfway through the fluid mesh in the flow direction for each simulation. The relative error in time dependent flow rate is shown for the three mesh densities in Fig. 2.26. A fourth-order polynomial fit was made for each flowrate error curve to show the trend of error more clearly through the cardiac cycle. At periods of high flow and accelerating flow, the error is highest for all three mesh densities. This is because the first-order elements used in these simulations only interpolate velocity



linearly, and flow near the wall is underestimated. As mesh density is increased, resolution of the Womersley profile near the wall is enhanced and the error is significantly reduced. At around 45ms, the Womersley profile near the wall is almost zero velocity, and thus the error is at its lowest through the cardiac cycle. The oscillation in error is due to truncation of the Fourier representation of the target flowrate at 20 modes.

The programs performing the mapping operations described above are provided in the appendix as:

Rotator\_tester – provided with  $(x_c, y_c, z_c)$ ,  $\hat{n}$ , and  $\vec{v}_1$ , determines  $\mathbf{R}(\alpha, \beta, \gamma)$ .

Node\_transformer – applies  $\mathbf{R}(\alpha, \beta, \gamma)$  to all inlet mesh nodes.

Womersley\_transformed – provided with fluid viscosity and density, nodal coordinates,  $r_C$ , boundary node numbers, and the Fourier components of either centerline velocity or flow rate waveform, linearly maps time-dependent Womersley profile to lumen inlet nodes.

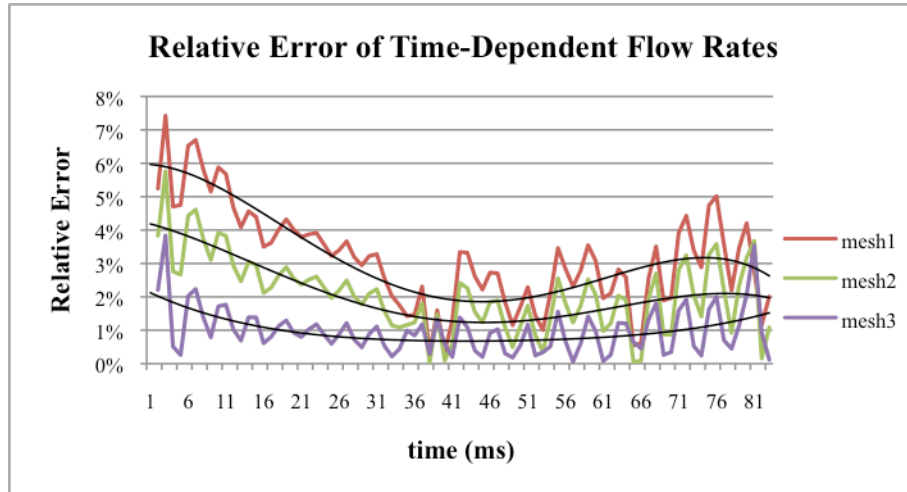


Fig. 2.26 Relative error in flow rates measured in FEM flow models with progressively refined meshes.

## Chapter 3 – Two-Stage Solution

Currently, patient-specific 3D FSI simulations suffer from two major bottlenecks in terms of the time required to get from medical images to mechanical stress and strain predictions. The first challenge is the generation of a suitable computational mesh that can accurately represent the components of the diseased artery wall and can provide meaningful numerical results. The second challenge relates to the time and computational resources required to solve realistic finite element models on a patient-specific basis. The two challenges are inter-related, and reduction of one generally means an increase in the other. For example, calculation time and computer resource requirements can be greatly reduced if a structured computational mesh of brick elements is used to represent the diseased vessel. Such a mesh can be very difficult to construct, and would not easily capture the complex geometrical features of the diseased artery. Structured mesh generation could take days or weeks if at all possible.

Section 2.5.2 of the previous chapter presented the methods used to construct a highly detailed and accurate computational mesh of an atherosclerotic artery from medical images. Re-partitioning of the NURBS descriptions of material boundaries allowed us to specify the local mesh density with great control, ensuring that the 3D multi-component mesh would be capable of resolving plaque and vessel stress fields with acceptable accuracy. The use of an unstructured mesh allowed us to accommodate the complex material distributions and geometries with ease, and user-controlled semi-automatic mesh generation permitted meshes to be constructed within a few hours of beginning the image segmentation.

The advantages of an unstructured mesh, namely ease of construction and faithful representation of complex shapes, come with the drawback that the model's element and equation counts rise sharply as greater accuracy in stress predictions is desired. Simultaneously representing a portion of artery suitable for FSI analysis *and* accurately predicting plaque stresses over a large region using an unstructured mesh can easily require element counts in the several hundred thousands.

An element count this high can lead to extreme computation demands for even a relatively simple linear analysis, and the problem is much more severe for arterial mechanics simulations. Material incompressibility necessitates the use of a mixed formulation finite element method, adding extra pressure degrees of freedom to the computation. Nonlinear material response is accounted for by solving the linearized equations in an incremental iterative manner, requiring repetitive solution of a large system of equations. Fluid-structure interaction only compounds the problem by requiring additional outer iterations to bring the fluid and structural mechanics systems into a converged equilibrium. Consideration of multiple phases of the cardiac cycle adds time to the computation not only in the sense that multiple loads steps must be simulated, but also because a great number of additional numerical integrations must be made to evaluate the system mass matrix and inertial terms in the element force vector. Meaningful FSI simulations of the diseased carotid bifurcation are thus computationally very demanding and require a computer cluster with ample memory for reasonable runtimes.

In many cases, accurate stress field predictions are required only over a portion of the full domain. For instance, a study may be interested in the strain field near the apex of the carotid bifurcation, or the stress field at the distal shoulder of a plaque lesion. Alternatively, a coarsely meshed model of an extended segment of artery may indicate a region that is a candidate for further, more accurate study. In these cases, it is helpful to use a coarse grained solution over the entire domain to guide the detailed modeling of the region of interest. Such a strategy can achieve realistic and accurate loading in a detailed model otherwise too small for meaningful FSI analysis. Additionally, this strategy can provide realistic boundary conditions for the detailed model, which becomes increasingly essential as the region of interest becomes more limited in extent.

In this chapter, we present a modeling strategy for efficiently and accurately computing highly realistic models of atherosclerotic carotid bifurcations based on medical imaging. This strategy addresses the overwhelming computational time and resource demand inherent to the use of an unstructured grid capable of accurate stress predictions in FSI simulations. This is achieved by using a two-stage approach, in which the fluid and solid dynamics of the full arterial domain are solved in a first stage on a relatively coarse computational mesh. The solutions from the full domain are subsequently used as boundary conditions on a refined-mesh model in a second stage, where stresses may be accurately computed within a sub-domain of interest. Computational time requirements of the approach will be compared to the time requirement of a more traditional, one-stage model. Effects of domain truncation on the fluid and solid solutions will be investigated by comparing the results of two-stage models to those of full-domain models.

### 3.1 Geometry Partitioning

Because the two-stage technique relies on the passage of nodal solution data from the coarse-mesh model to the refined-mesh model, it is desirable to have a robust and easy way to address the locations of data passage. To this end, we construct a set of truncation planes bounding the region of interest (Fig. 3.1). It is at these planes where coarse mesh solutions are used as boundary conditions in the truncated, fine-mesh model. For cases in which the region of interest is unknown, multiple planes may be placed to bound several distinct regions.

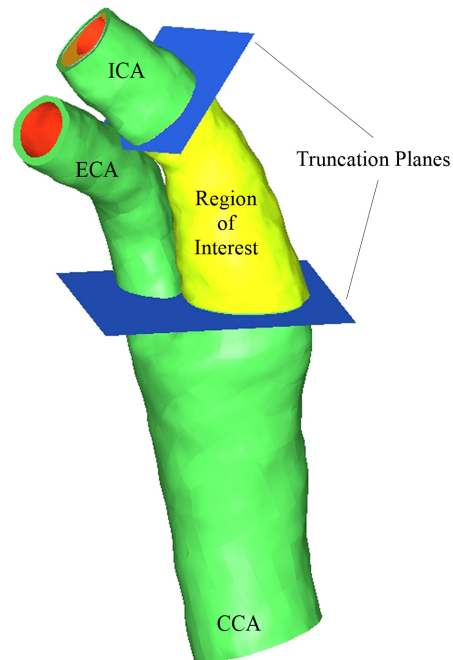


Fig. 3.1 Truncation planes defined to bound the region of interest, on which accurate stress calculations are desired.

Before mesh generation, the truncation planes are used to cut the bounding surfaces of each plaque component and of the vessel lumen and wall. This generates a series of spline curves that bound the now-cut surfaces. The spline curves are used to

create a set of conforming end caps that close the plaque component bounding surfaces at the truncation planes (Fig. 3.2). Formation of the truncation plane end caps is achieved in the same manner as in section 2.5.2, where end caps were made at the vessel inlet and outlets. The plaque component bounding surfaces above and below the truncation plane, and the end cap between them meet at a single, shared spline curve such that the geometries are “air-tight”.

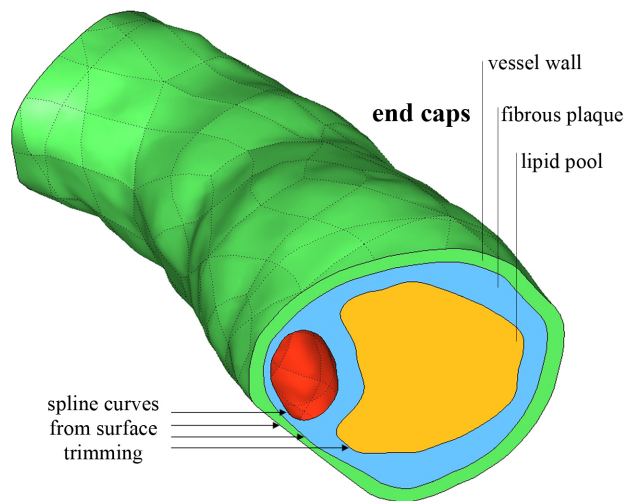


Fig. 3.2 End caps constructed to seal the plaque and vessel bounding surfaces at the truncation planes.

### 3.2 Mesh Generation – Fine Model

In the event that there are only two truncation planes, the plaque and vessel component surfaces between the planes are copied so that two different surface meshes can be made, one for the coarse model and one for the fine-mesh model. Because of the shared curves at the truncation planes, creating surface meshes for each plaque component in the region of interest is sufficient input to create the surface mesh on the end caps. We first create surface meshes, with the methods of section 2.5.2, that will be

used in the fine-mesh model. A mesh is made on each plaque component surface and also for the lumen and outer wall surfaces, defining the edge divisions for each end cap surface mesh (Fig. 3.3a). After generation of the end cap meshes, volume meshes are made using the appropriate sets of surface meshes as input (Fig. 3.3b).

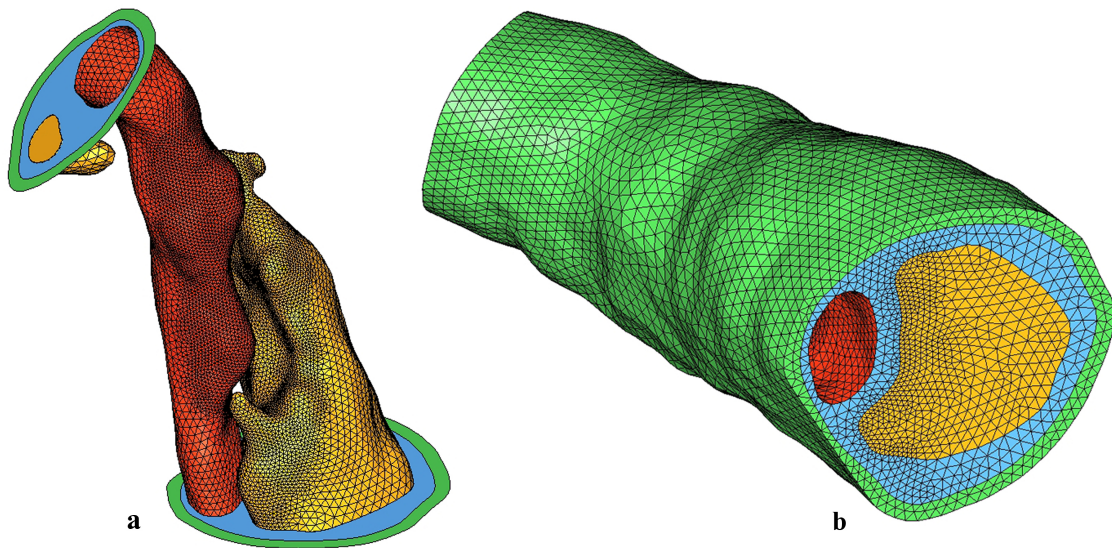


Fig. 3.3 a) Surface meshes for lumen and lipid pool in context of truncation planes b) conforming volume meshes for all components, shown at truncation plane. Meshes are for use in the fine-mesh model of the region of interest.

### 3.3 Mesh Generation – Coarse Model

Once surface meshes are defined on the end caps, the shared spline curves enforce a conforming discretization at the truncation planes for bounding surfaces of each plaque and vessel component. Volume meshes are then made for each material over the entire domain using an element density just fine enough to accurately resolve surface geometry and calculate displacements (Fig. 3.4a). The surfaces defining the vessel lumen are cut in



the same way as for the plaque components, and end caps are also created. As a result, the fluid domain for the entire vessel comprises sub-domains either within or outside of the region of interest (not shown). Examples of conformity between the finely-meshed end caps and coarsely meshed domain at the lower truncation plane from Fig. 3.1 are shown in Fig. 3.4b.

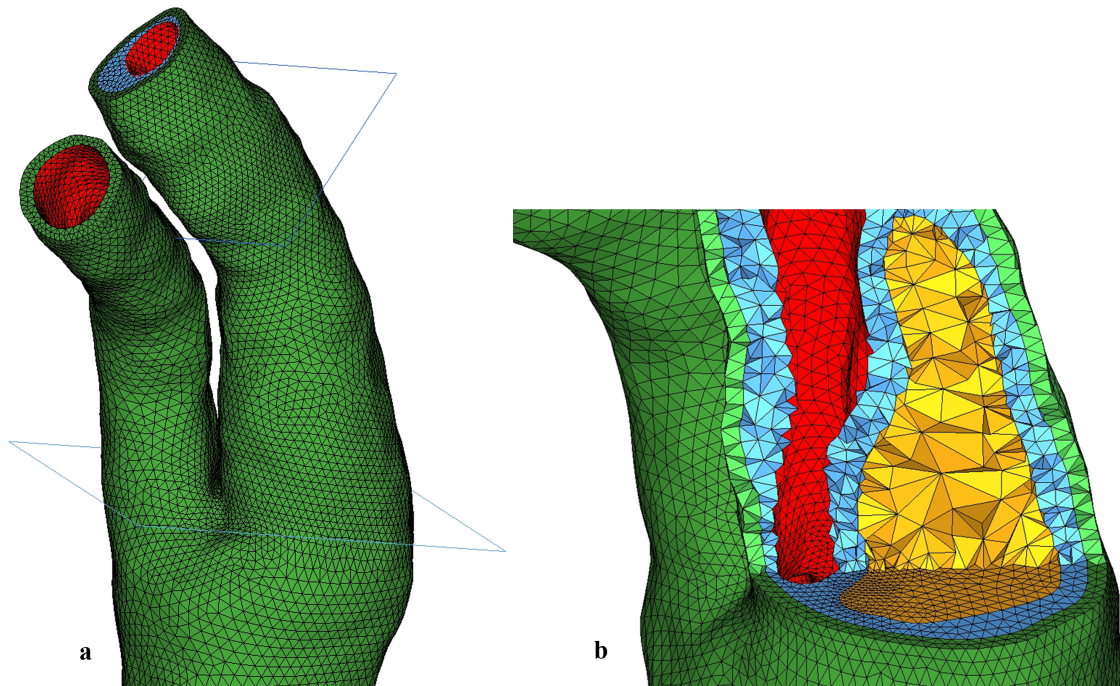


Fig. 3.4 a) Volume mesh on full domain b) Conformity between finely-meshed end caps and coarsely meshed region of interest. Good element quality can be maintained using the border zone technique of section 2.5.2. Note the dramatic reduction in fibrous plaque elements compared to the mesh shown in Fig. 2.20.

### 3.4 Solution Strategy

With all volume meshes constructed, the time dependent 3D FSI simulation is run on the coarse solid grid and the full fluid grid. After solution of the coarse grid FSI

model, nodal displacements for the solid at the truncation planes are saved during post-processing. The fluid velocities and nodal pressures are saved at the inlet and outlet of the region of interest, respectively. Using in-house post processing tools developed in MatLab (The MathWorks, Natick, MA), the nodal results are passed from the coarse model nodes to the fine model nodes to be used as the sole boundary conditions in the fine-mesh simulation. This can be done in a time dependent fashion, or to solve a steady-state problem. The use of the coarse model's nodal displacements at the truncation planes allows the fine-mesh model to be of quite limited extent without introducing artificial restrictions on motion at the truncation surfaces. Assumptions of in-plane motion on the end planes of a truncated model, common in the literature, can lead to stress fields that are significantly tainted by the unrealistic boundary conditions. So as to not over-constrain the problem or apply incompatible boundary conditions, displacements are not applied to nodes on the FSI interface, where loading conditions may not be exactly the same as in the full domain simulation.

### **3.5 Computational Time Reduction Test**

Using a direct solver with physical memory can greatly enhance the speed of a simulation, especially if multiple processors are utilized. Unfortunately, the memory requirement for such solvers quickly becomes severe with increasing model size and iterative solvers or out-of-core solutions are then necessary. The benefit of using the two-stage technique is that both the coarse mesh over the full domain and the truncated fine mesh can be built to take full advantage of all the physical memory available, allowing use of a direct solver for each stage.

To benchmark the reduction in computation time possible using the two-stage approach, a series of four simulations were run. The first three simulations were used to calculate the stress distribution in the region of interest at the point in the cardiac cycle at which stresses are highest. First, a steady-state simulation was used to achieve end-diastolic conditions of pressure and flow in the coarse mesh model of the carotid bifurcation. Second, a transient simulation was run on the same computational mesh to solve for the flow dynamics and displacements at the truncation planes through the cardiac cycle. The third, steady-state, simulation used the nodal solutions of the second simulation at the truncation planes to solve for the stress distribution in the region of interest. The fourth simulation used the exact same loading and boundary conditions as the first simulation, but is run on a computational mesh consisting of the coarse mesh outside the region of interest, and the fine-mesh within the region of interest. Such a locally refined mesh would be used in a traditional, single-stage simulation. The mesh size of the fourth model resulted in a large number of equations that could not be solved using direct, in-core methods. For the fourth model, ADINA's efficient 3D-Iterative solver was used for the solid system of equations. Models 3 and 4 employ 11-node tetrahedra in the region of interest, while models 1 and 2 use only 10-node tetrahedra. Element count, finite element equation count, and run times were collected for each simulation for comparison.

### **3.5.1 Computational Time Results**

Using a rough element count of 200,000 10- or 11-node solid tetrahedra and 300,000 4-node fluid tetrahedra, the entire FSI model can be solved using in-core direct

sparse solvers on a multi-core workstation with around 12 GB of memory. Example runtimes are shown in Table 6.

<b>Model</b>	<b>Element Count</b>	<b>Equation #</b>	<b>Run Time</b>
1 - Full domain, coarse mesh, steady state solution at end-diastole, 10 load steps.	Solid – 216,076 Fluid – 300,215	Solid – 984,241 Fluid – 230,996 FSI – 57,950	15 hours
2 - Full domain, coarse mesh, transient solution with 26 cardiac phases	Solid – 216,076 Fluid – 300,215	Solid – 984,241 Fluid – 230,996 FSI – 57,950	27 hours
3 - Truncated model, fine mesh, steady state solution at peak stress state	Solid – 187,086 Fluid – 30,887	Solid – 1,213,644 Fluid – 26,212 FSI – 6,553	9 hours
4 - Full domain model capable of resolving stresses in region of interest. Steady-state solution at end-diastole, 10 load steps.	Solid – 343,227 Fluid – 300,215	Solid – 2,180,749 Fluid – 230,996 FSI – 57,950	125 hours*

Table 3.1 List of simulation run times for two-stage approach and full-domain, fine-mesh model. CFD boundary conditions, material description, and meshes were the same for models 1, 2, and 4. Solids were Demiray-type, as presented in section 2.3.2. \*Run time for model 4 is estimated from solution time for load steps 1-5, in comparison to same load steps for model 1.

As shown in Table 6, the runtime savings can be quite large using the two-stage strategy. We were able to accurately solve for the dynamics of the full vessel, and resolve peak stresses in the region of interest in less than half the time it takes to reach end-diastolic conditions using a traditional, single stage simulation with a stress-resolving mesh

## **3.6 Accuracy of Two-Stage Approach**

### **3.6.1 Effects of Solid Domain Truncation**

An essential component of our two-stage scheme is the use of a coarse-mesh model that accurately solves for the solid displacements at the truncation planes. If this is satisfied, then applying these displacements as boundary conditions in the fine-mesh

model will not lead to appreciable stress artifacts at the truncation planes. If the loading remains the same for the coarse and fine-mesh models, the stresses calculated with the two-stage approach should be nearly equivalent to those that would be calculated if the entire domain were finely meshed. To test this, a further region of interest was specified within the truncated model as shown in Fig. 3.5. A solid-only stress analysis, with a lumen pressure of 100mmHg, was made on region A in Fig. 3.5 using both the two-stage approach and also by employing a stress-resolving mesh over regions A, B, and C.

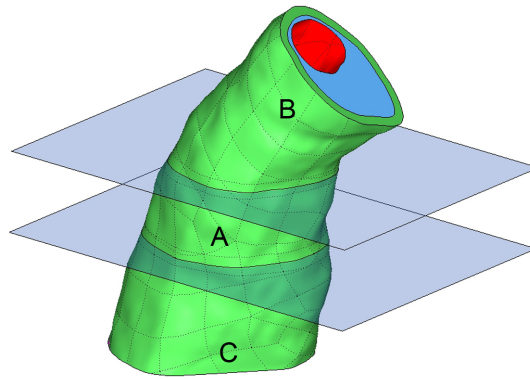


Fig. 3.5 Region of interest from Figure 3.1 (A,B, and C), with further region of interest (A) specified.

First principal stresses are shown in Fig. 3.6 for the four cut planes in region A of Fig. 3.5. Stresses were calculated using both the two-stage (ts) approach and also using the full-domain, fine-mesh (ff) model. Because the stresses calculated with each model are displayed using one color scale for each cut plane, it can be visually verified that the stress patterns and magnitudes are nearly identical. Taking the full-domain, fine-mesh model results to be truth, the peak stresses calculated using the two-stage approach have a percent error of 1.4%, 1.4%, 5.4%, and 3.5% at cuts 1-4, respectively.

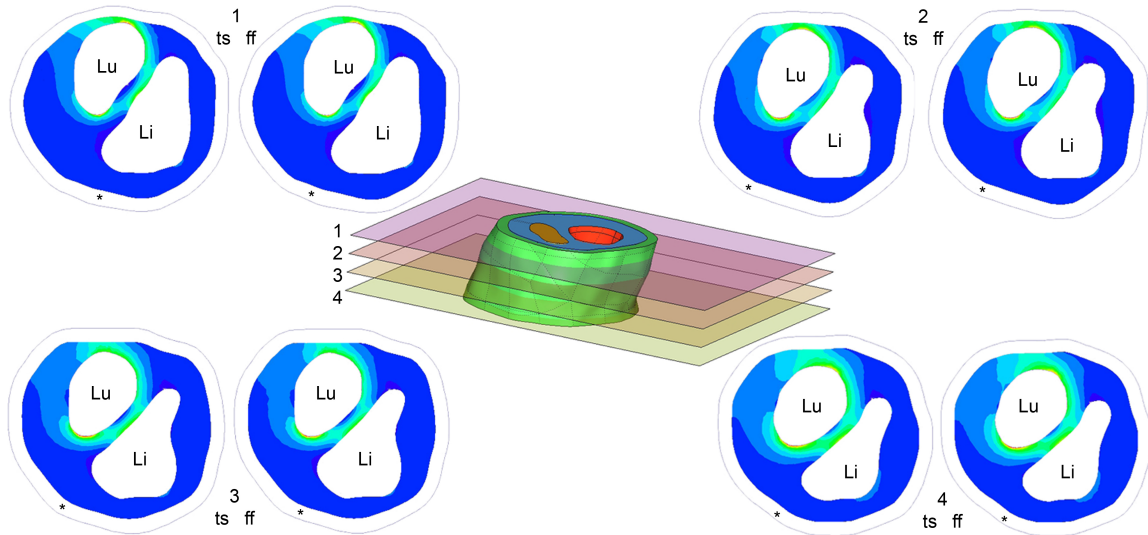


Fig. 3.6 Comparison of two-stage (ts) model stresses and full-domain, fine-mesh (ff) model stresses on cut planes indicated in center figure. First principle stresses are shown for fibrous plaque layer only. “Li” denotes lipid pool position, “Lu” indicates the lumen, and “\*” shows the boundary of the vessel wall. Use of the same color scale for ts and ff results allows easy visual inspection, revealing very close agreement between ts and ff stresses. Color scale is determined independently for each cut plane so that images can most clearly show stress patterns. Stresses calculated using the two-stage approach are within 5.4% of those calculated with the computationally intense full-domain, fine-mesh model.

### 3.6.2 Effects of Fluid Domain Truncation

Avoidance of stress artifacts near the truncation planes, and proper loading of the region of interest is also dependent on the loading conditions remaining the same between the full-domain simulation and the truncated model. This has largely to do with selecting truncation planes on which flow solutions would make reasonable flow boundary conditions. In our example of a stenotic artery, flow is unidirectional near the stenotic throat and so the lower truncation plane was placed there. The upper truncation plane was placed to bound the region of interest and avoid an intersection with any

appreciable secondary flow. To test whether or not the loading would remain the same in the fine-mesh model, the pressure field solution from the full-domain model was saved in the region of interest for nodal pressure comparison with the pressure field solution of the truncated model.

The pressure field solutions for the full-domain model and the truncated model are shown in Fig. 3.7a and 3.7b, respectively. Because the pressure distribution at the lumen surface is what imparts a load to the vessel wall, only those nodes on the FSI interface were used for the comparison.

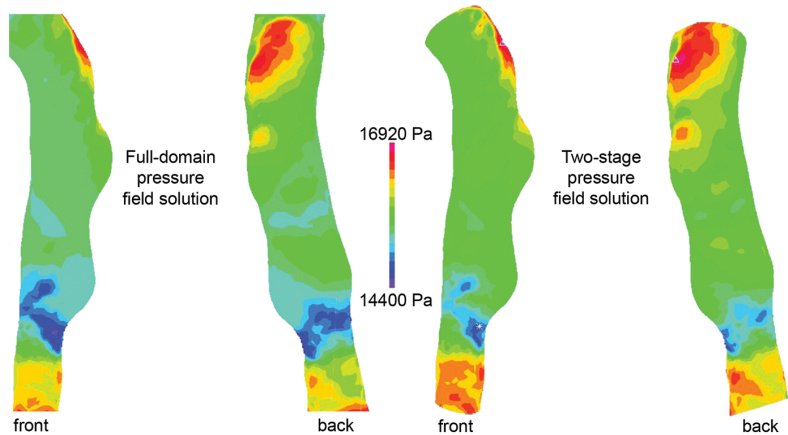


Fig. 3.7 a) Pressure field solution from full-domain model b) Pressure field solution from truncated model. Peak pressure at the top of the domain corresponds to a flow impingement zone near peak systole.

Of course, one should not expect the fluid pressure field to be exactly the same from the time-dependent full-domain simulation and the truncated steady state model, but the approximation can be good, as shown in Fig. 3.7. For this geometry, the average pressure difference at the FSI interface between the full-domain solution and the truncated solution is 217 Pa, or about 1.5% of the average pressure at the FSI interface. More important than capturing the exact same pressure magnitudes in the truncated model is the resolution of a similar pressure pattern (Fig. 3.8a), as this will determine the

nature of the solid deformation field. Comparison of the nodal pressures calculated in each model revealed that the truncated model had a nearly uniform increase in pressure of  $\sim 200$  Pa from the pressure field calculated in the full-domain model. As shown in Fig. 3.8b, this is equivalent to approximately 10% of the pressure range within the region of interest.

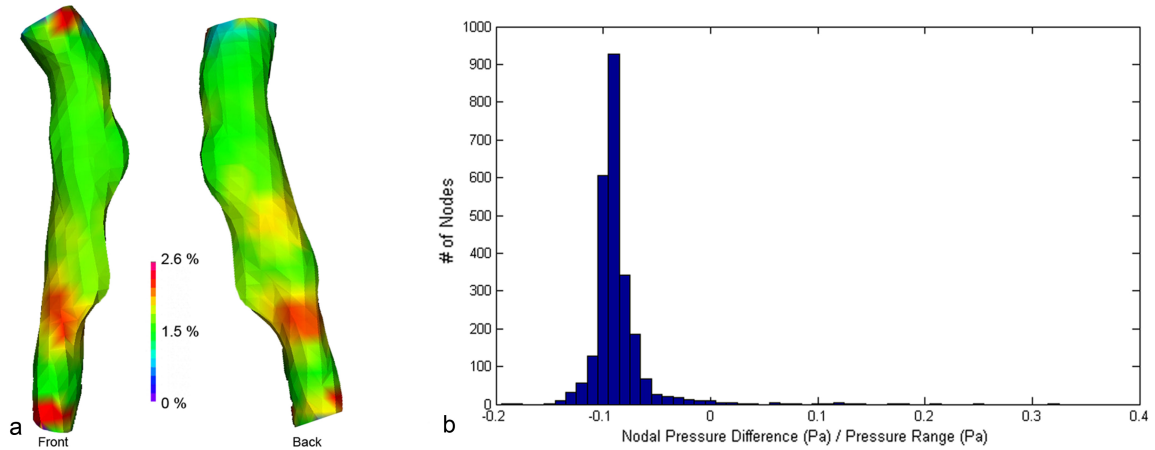


Fig. 3.8 Pressure difference between full-domain fluid solution and truncated domain solution. a) Difference between two models shown as a percent difference with regard to the full-domain solution. b) Nodal distribution of pressure differences, showing a nearly constant offset of +200 Pa in the truncated model's pressure field.

There are a very limited number of nodes exhibiting a greater pressure difference, with the maximum difference being 20% of the pressure range within the region of interest after accounting for the uniform offset. Although a 20% deviation with regard to range seems large, one must remember that it is only a 2.6% difference in absolute pressure, and the sparsity of errant nodes limits their effect on the overall stress patterns within the vessel wall. The nearly constant offset in the truncated model is likely a result of using a uniform pressure, the average nodal pressure from the full-scale simulation, at



the truncated model's outlet boundary. During the cardiac phase used for the second stage solution, the flow in the region of interest was nearly unidirectional, but minor secondary flow causes a non-uniform pressure at the outlet of the region of interest. Although stenotic arteries like the one investigated here generally experience flow shear stresses much greater than those in healthy arteries, the shear stress is still orders of magnitude smaller than the systemic pressure loading. For this reason, the accuracy of the truncated model's velocity field was not investigated.

# Chapter 4 – FSI Analysis of Carotid Plaque

## Rupture

In chapter 2, we presented methods by which highly detailed and realistic fluid-structure interaction models can be made for atherosclerotic arteries. Chapter 3 introduced a strategy that allows timely yet accurate solution of sophisticated and computationally demanding fluid-structure interaction simulations. In this chapter, we revisit a point made in chapter 1, that data on plaque rupture *in vivo* is unfortunately sparse. Here, we present an FSI stress analysis of an atherosclerotic carotid bifurcation where plaque rupture is known to have occurred. The analysis is based on pre-rupture medical imaging, with post-rupture imaging data available for comparison of rupture site and extent to the stress field within the plaque.

### 4.1 Patient Data

The analysis presented here is of a carotid bifurcation of an 83 year old male admitted to the hospital for a suspected transient ischemic attack (TIA). Multidetector CTA was performed using the following acquisition protocol: Spiral mode; collimation, 16 x 1.25mm; 240 kVp/350 mA; 70 mL at 4mL/sec power injection in antecubital vein, Omnipaque contrast. Images were acquired caudocranial, covering from the vertex to the heart with an in-plane resolution of .49 mm x .49 mm.

8 months after the initial CT scan, the patient was brought to the emergency room after an episode of syncope, and another CT study was performed in the workup for

suspected TIA. Selected images from the initial imaging study, and the later study are shown in Fig. 4.1.

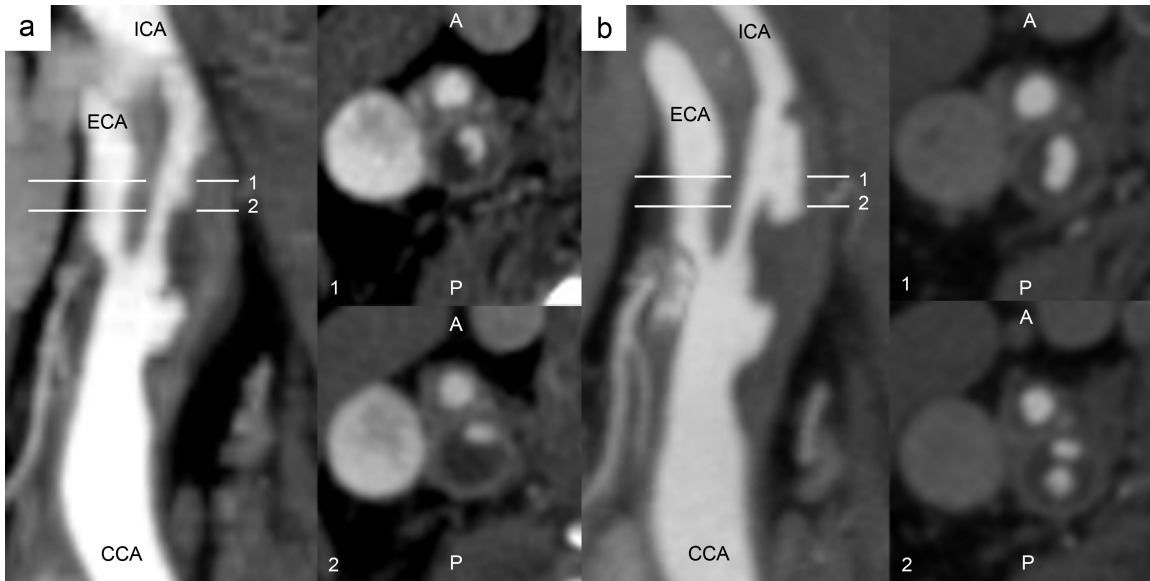


Fig. 4.1 CTA studies at a) baseline and b) 8 months later. a) luminal geometry in the longitudinal plane (left) and transverse to the lumen for slices 1 and 2 (right). Note the irregular luminal geometry proximal to the bifurcation, suggesting existing ulceration of common carotid artery plaque. b) Slice 1 shows increased lumen area in the internal carotid artery consistent with plaque rupture, while slice 2 shows that a portion of the plaque core inferior to the rupture location has emptied after fibrous cap failure.

As seen in Fig. 4.1a, the ICA had a large plaque burden at baseline, with the image intensities suggesting that the plaque contains a large lipid core. At baseline, the ICA was roughly 80% stenotic by area at slice 2 in Fig. 4.1a. The images in Fig. 4.1b reveal that a portion of the ICA plaque ruptured in the 8 months since the baseline scan, and plaque contents had emptied into the circulation. From the CTA images, it is determined that the plaque ruptured over a segment of ICA 6.25 mm in length located 6.25 mm superior to the bifurcation. The rupture was located on the posterior aspect of

the lumen surface, and circulating blood “tunneled” into the plaque core about 3.75 mm inferior to the first imaging slice demonstrating plaque failure.

## **4.2 Construction of the Geometric Model**

Before implementation of the active contour algorithm, pre-rupture images were re-sampled from 512x512 to 1024x1024 in-plane, and from a slice thickness of 1.25mm to a thickness of 0.3125mm. In this way, the image series was represented in 3-dimensions as a set of voxels far more isotropic than the original acquisition, allowing for a more accurate segmentation with the 3D snake algorithm. The geometric model of the diseased bifurcation was constructed according to the methods presented in chapter 2, and the final geometry was shown in Fig. 2.12. Surface representations of the plaque and vessel components were presented in Fig. 2.16.

## **4.3 Computational Mesh**

The two-stage solution method of chapter 3 was implemented to achieve an accurate and timely solution of the detailed FSI problem. The region of interest was designated to include the region of plaque rupture, and was shown in Fig. 3.1. The accuracy of the two-stage method relies on the preservation of loading features between the first-stage full-domain solution and the second-stage truncated solution. It is also imperative that the coarse mesh accurately captures displacement solutions, and the second-stage fine mesh adequately resolves stresses. Chapter 3 showed that the main features of the pressure field are well preserved during the two-stage solution method, and that an average error of  $\sim 1.5\%$  was introduced during the truncation of the fluid

domain. Numerical experiments were conducted to ensure that the solid meshes employed during the first stage of the simulation could accurately resolve displacement solutions. Additional numerical tests were made to characterize the dependence on mesh density of the solid stress field and fluid pressure field predictions.

#### **4.3.1 Mesh Dependence of Displacement Solution**

It is a challenge to verify the adequacy of a computational mesh when the geometries and material distributions modeled are irregular and complex. With unstructured computational meshes, it is difficult or impossible to simultaneously track solutions at a consistent geometrical point and ensure that all loading and fixation boundary conditions of the model remain identical. Additionally, tracking solutions at one point provides very limited information about the full behavior of the structure modeled. With this in mind, we constructed a test model that is representative of the entire solid domain. The test model is a portion of the longitudinal extent of the ICA in the image-based geometry, and consists of a layer of vessel wall surrounding a layer of fibrous plaque, in which a longitudinally-heterogeneous lipid pool is present. The surfaces of the model were divided such that automatic mesh generation would lay nodes along unchanging circumferential curves at the lumen surface and outer wall surface, no matter what mesh density was specified. In this way, we could address these nodes in a robust way, and track the inner and outer circumference of the vessel wall under load at various mesh densities. The test model, meshed with two different element densities, is shown in Fig. 4.2.

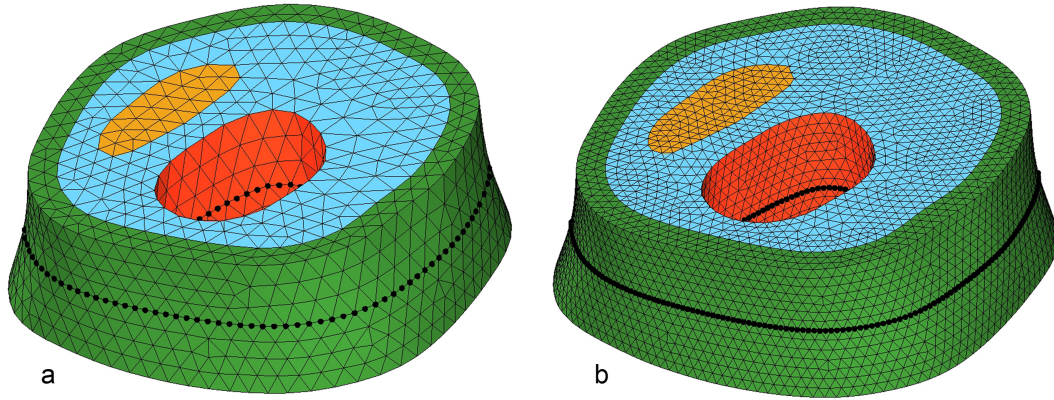


Fig. 4.2 Test model meshed with a) 8956 11-node tetrahedra b) 52,590 11-node tetrahedra. The nodes highlighted in black at the lumen surface and outer wall surface were tracked for comparison.

Each test mesh was pressurized at the lumen surface to 100 mmHg, and the inner and outer circumferential nodal positions were tracked for comparison. The top and bottom surfaces and the circumferential tracking curve all lie in the global x-y plane, and the top and bottom surfaces are constrained to in-plane motion only. The initial, no-load positions of the lumen nodes for each mesh are plotted together in Fig. 4.3. It can be seen that although the mesh densities differ by almost a factor of two in each Cartesian direction, the representations of the lumen boundary are virtually identical across meshes.

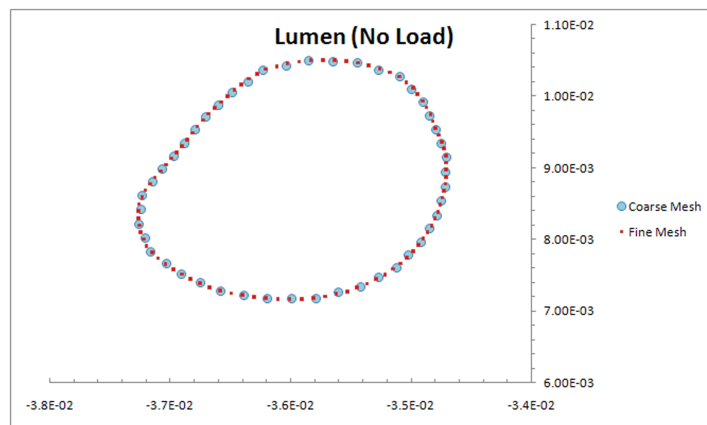


Fig. 4.3 Nodal positions along curve encircling the unpressurized lumen for test model with two mesh densities.

The positions of the nodes encircling the lumen are shown after pressurization in Fig. 4.4. It is clear that the coarse mesh does an adequate job solving for displacements at the lumen surface. Positions along the z-axis are not shown, as the nodes started out coplanar, and the out-of-plane displacements were at least one order of magnitude smaller than the in-plane motions. Viewing the nodal positions in 3 dimensions revealed that the out-of-plane motions were also indistinguishable.

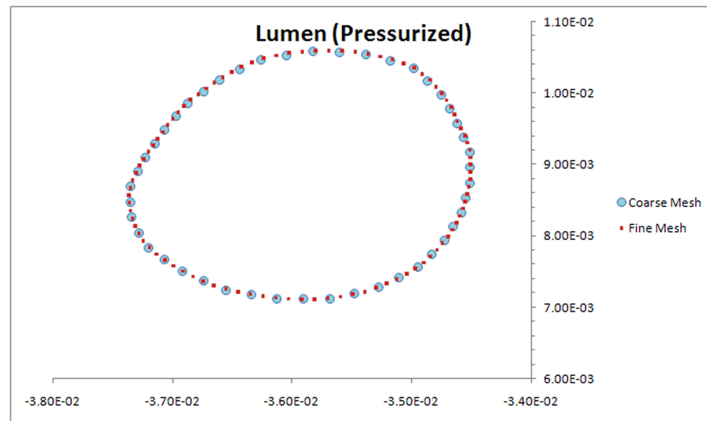


Fig. 4.4 Nodal positions along the curve encircling the pressurized lumen for test model with two mesh densities.

As the outer wall is of larger circumference than the lumen, it is clear that the coarse discretization will accurately represent the unloaded geometry. The positions of wall circumference nodes for the two test meshes are shown in Fig. 4.5.

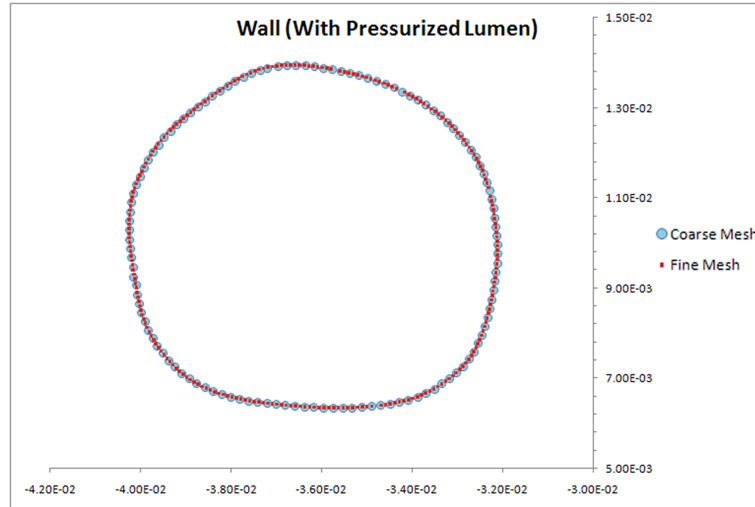


Fig. 4.5 Nodal positions along the curve encircling outer wall for pressurized test model with two mesh densities.

Again, the out-of-plane motions were at least an order of magnitude smaller than those in the x-y plane, and are not shown here. It is clear that the coarse mesh can accurately solve for displacements in our multicomponent models. The coarse mesh element length of 0.4mm was utilized for the entirety of the first stage of the two-stage analysis, unless a finer mesh was used to accurately represent complex geometries. In the neighborhood of the truncation planes, mesh side length was an interpolation between 0.4mm and a smaller value used to resolve stress fields (discussed in the next section).

#### 4.3.2 Mesh Dependence of Stress Field Predictions

Displacements are the primary variables solved in structural finite element methods, and so they are accurately resolved with even a relatively coarse mesh. Stress is the result of gradients in the displacement field, and thus a finer mesh is generally needed to resolve stresses well. This is analogous to computational fluid dynamics, in which flow fields may be accurately solved using a relatively coarse mesh, but a 2-10



fold increase in mesh resolution may be needed to accurately resolve the wall shear stress distribution. In the mixed formulation finite element method we have used here, the hydrostatic stress is interpolated separately, which helps to accurately solve for stresses, but an increased mesh density is still needed to resolve deviatoric contributions to element stress.

The finite element method only assures convergence in a global sense as mesh density is increased, and so it is not sensible to track stress solutions at distinct points. To characterize the mesh dependence of the stress field within the fibrous plaque player in the region of interest (see Fig. 3.1), three simulations were run at progressively finer mesh density. Referring to Fig. 2.19, the following surface mesh density scheme was used to construct the volume meshes for the test models.

Lumen Region of Interest	x
Lumen Border Zone	1.25x
Lumen	2x
Lipid Region of Interest	x
Lipid Border Zone	1.5x
Lipid	max{2x or 0.4mm}

Table 4.1 Mesh density scheme used to construct volume meshes for test models.

For the coarse mesh,  $x = 0.2\text{mm}$ ; for the medium mesh,  $x = 0.15\text{mm}$ ; for the fine mesh,  $x = 0.1\text{mm}$ . The mesh densities of the fibrous plaque bounding surface and the outer wall surface were set at a consistent  $0.4\text{mm}$ , unless smaller to preserve element quality, as the stress magnitudes and gradients in the healthy vessel wall were small. The final element counts of each model are listed in Table 4.2.

Test Mesh	Total Element Count	Fibrous Plaque Elements
Coarse Mesh ( $x=0.2\text{mm}$ )	103,148	67,191
Medium Mesh ( $x =0.15\text{mm}$ )	173,570	123,594
Fine Mesh ( $x=0.1\text{mm}$ )	305,580	219,116

Table 4.2 Element counts for meshes used in stress resolution tests.

The lumen surface of each test model was pressurized to 100mmHg, and the end planes of the region of interest were constrained to in-plane motion only. Predicted first principal stresses within the fibrous plaque layer were divided into quartiles Q1-Q4, with Q1 being the smallest stresses. Stress behavior (in units of Pa) under mesh refinement is shown in Table. 4.3.

Parameter	Coarse Mesh	Medium Mesh (% deviation from Coarse Mesh)	Fine Mesh (% deviation from Medium Mesh)
Average(Q1)	1,483.44	1,513.00 (1.95)	1,528.36 (1.01)
Average(Q2)	4,600.66	5,529.59 (16.80)	6,024.94 (8.22)
Average(Q3)	13,047.50	16,179.17 (19.36)	17,203.49 (5.95)
Average(Q4)	39,075.51	43,267.80 (9.69)	45,428.21 (4.76)
Min(Q1)	-11,688.30	-12,352.80 (5.38)	-11,965.60 (-3.24)
Min(Q2)	2,880.39	3,095.43 (6.95)	3,304.59 (6.33)
Min(Q3)	7,438.43	9,946.37 (25.21)	10,486.10 (5.15)
Min(Q4)	20,061.20	23,533.90 (14.76)	24,726.6 (4.82)
Max(Q1)	2,880.36	3,095.43 (6.95)	3,304.58 (6.33)
Max(Q2)	7,438.43	9,946.32 (25.21)	10,486.00 (5.15)
Max(Q3)	20,061.20	23,533.60 (14.76)	24,726.10 (4.82)
Max(Q4)	187,231.0	243,576.00 (23.13)	249,716.20 (2.46)

Table 4.3 First principal stress predictions within fibrous plaque layer for progressively refined meshes.

Stresses are listed in units of Pa.

The stresses predicted using the finest mesh deviate from those predicted by the medium density mesh by around 5%, and thus the medium mesh design was deemed to be sufficient for our stress analysis. The computational mesh used for the solid domain in the first solution stage was shown in Fig. 3.4, while the stress-resolving mesh used for the second solution stage was shown in Figs. 2.20 and 3.3.

#### 4.3.3 Mesh Dependence of Pressure Field Predictions

The distribution of loads on the diseased vessel wall results from fluid pressure and shear stress fields. It is therefore important to assess the dependence of the flow solution on the computational mesh representing the fluid domain. Although stenotic

arteries like the one considered here generally experience flow shear stresses much greater than those in healthy arteries, the shear stress is still orders of magnitude lower than the systemic pressure loading. For this reason, the mesh dependence of the truncated model's pressure field was investigated, while the velocity field was not.

To investigate mesh dependence, the lumen shown in Fig. 2.16 was discretized using five different mesh densities. For each mesh, the CCA was assigned a flow rate of 6.5 ml/sec, and the ICA outlet was assigned a velocity corresponding to a 55-45% ECA-ICA flow division; the ECA outlet was specified to have zero-traction. This flow rate and division are a reasonable estimate of the average flow behavior in a stenotic carotid bifurcation. A steady-state CFD simulation was performed on each mesh, and the pressure fields were visually examined. The pressure fields, and element counts, for each mesh are shown in Fig. 4.6. The average pressures at the ICA outlet and CCA inlet, and the maximum pressure predicted at the apex of the bifurcation were compared quantitatively, as shown in Fig. 4.7.

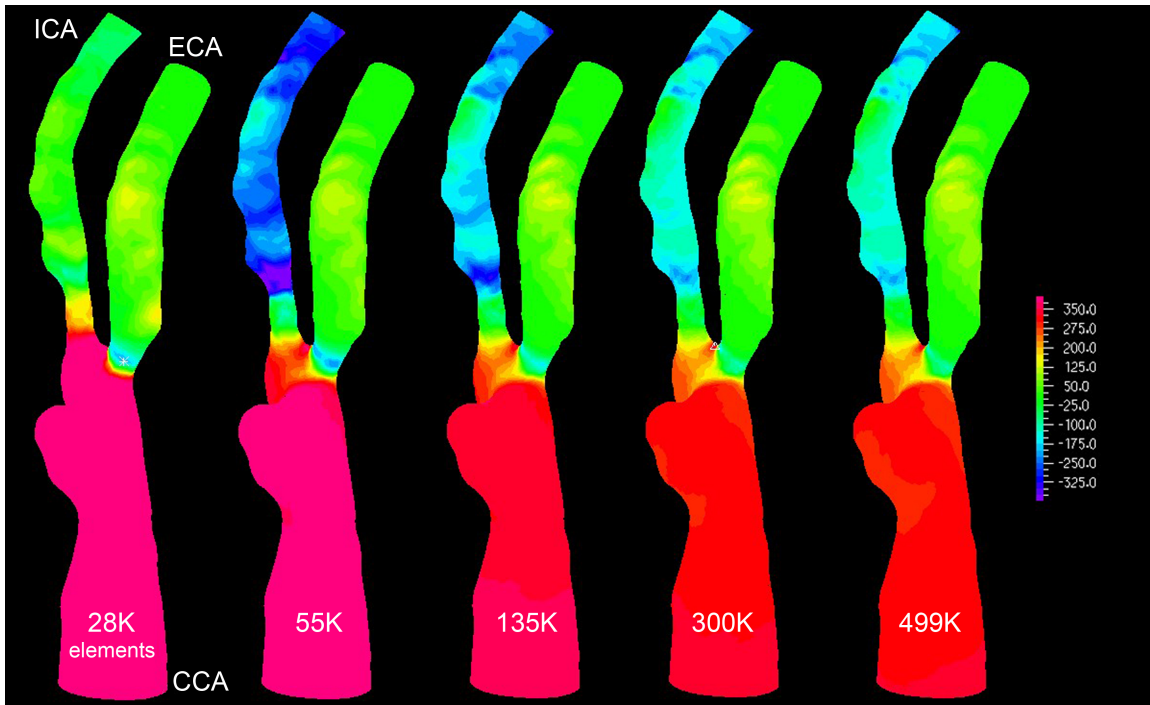


Fig. 4.6 Steady-state pressure distributions on 5 progressively finer CFD meshes using average flow boundary conditions. The flow rates in the ICA, ECA, and CCA were constrained to remain the same between meshes.

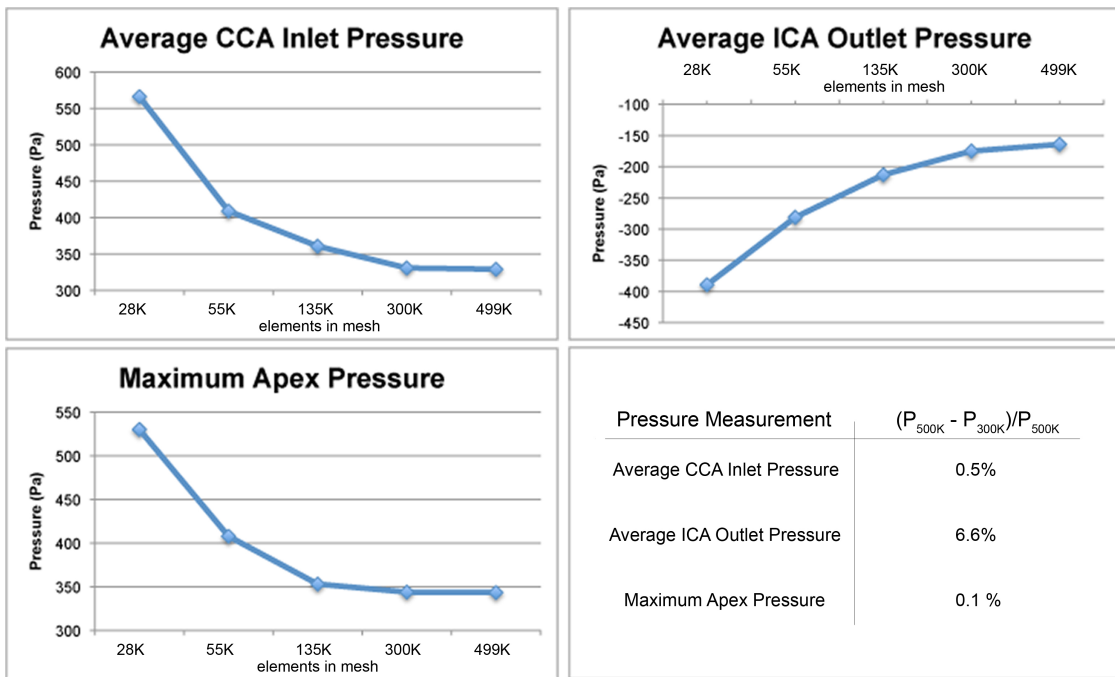


Fig. 4.7 Mesh dependence of selected pressure measurements, deviation of measurements from 300K element mesh from measurements from 500K element mesh.

From Figs. 4.6 and 4.7, it is clear that the mesh with 300,000 elements provides a nearly mesh-independent pressure prediction, at 60% of the computational cost of the finest mesh tested. For this reason, we used a fluid mesh of 300,000 elements in our stress analysis of the geometry shown in Figs. 2.12 and 2.16. The CCA inlet and ICA outlet meshes were prescribed element densities high enough to resolve the Womersley profiles mapped to them within 5% error, using guidance from the tests performed in section 2.7. The final mesh used for the fluid domain of our FSI stress analysis is shown in Fig. 4.8.

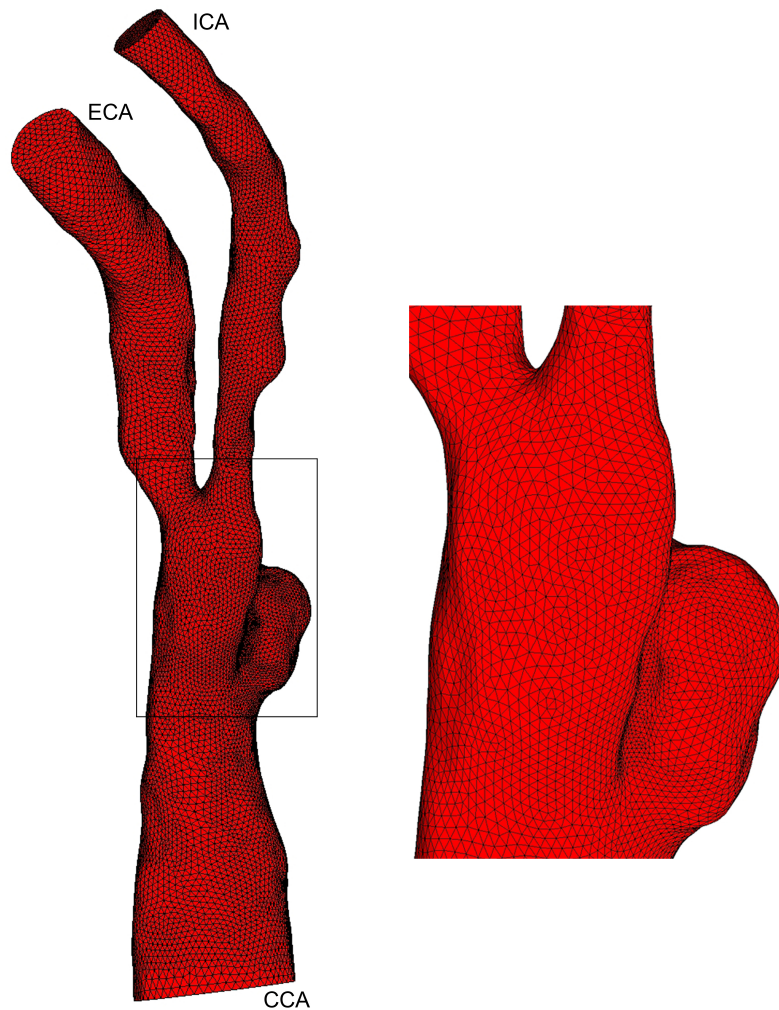


Fig. 4.8 Mesh used for fluid domain during FSI stress analysis. Note the finer mesh in the highly curved region of the CCA, a lumen shape consistent with prior plaque ulceration.

## 4.4 Loading, Boundary Conditions, and Materials

Unfortunately, no comprehensive flow information was available for the patient. A Doppler US study was made the same day as the baseline CTA study, but only screenshots of the US scan were saved, providing peak systolic and end diastolic velocities at the proximal CCA and distal ICA. Under the assumption of a parabolic velocity profile at peak systole, the limited velocity information was used to scale another patient's flow rate waveforms as measured with phase contrast MRI. The phase contrast MRI study was chosen based on the similarity of the patients' arterial diameters at the proximal CCA and stenotic throat of the ICA. The flow conditions imposed on the finite element model are shown in Fig. 4.9.

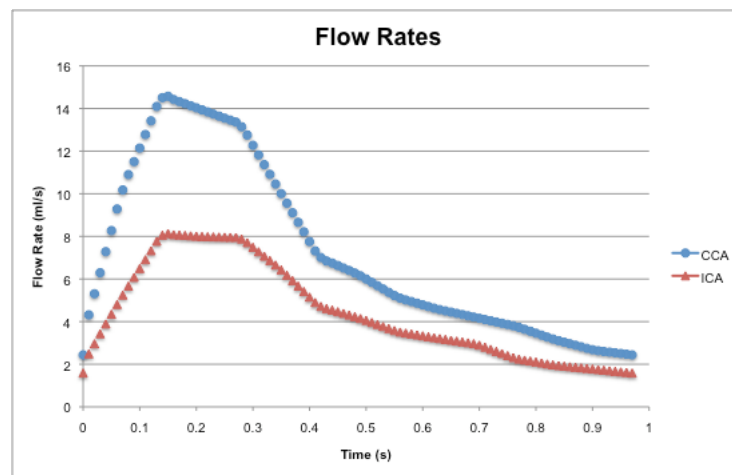


Fig. 4.9 Flow rates used to construct Womersley profiles to be assigned to the ICA outlet and CCA inlet.

As discussed in section 2.4.2, pressure boundary conditions are often the most difficult to obtain. A blood pressure waveform was not recorded for the patient, and thus an artificial pressure (actually a traction) was specified at the ECA outlet.

The outlet of the ECA in our model is still within the conducting circulation, and the pressure therefore fluctuates significantly throughout the cardiac cycle. The fluctuation is only greatly reduced much further downstream in the vasculature. Specifying a static traction at the ECA is therefore not appropriate. The simplest assumption to make without introducing retrograde flow or spurious oscillations in CCA flow was to assign a traction waveform of the same shape as the CCA flow waveform. The waveform was scaled so that the end diastolic pressure at the ECA outlet was 80 mmHg, while the maximum pressure there was 120 mmHg. This traction condition, and the flow rates specified at the CCA and ICA, resulted in a CCA inlet pressure that varied from 85 mmHg at end diastole to 136 mmHg at peak systole. As this is within normal range, no further modifications to the fluid boundary conditions were made. Although the traction waveform has the same shape as the CCA flow waveform, no assumptions were made of the pressure waveform at the CCA, and the pressure-flow phase relationship was dictated entirely by the solution of the Navier-Stokes equations.

No loads were applied to the solid domain, and the inlet and outlets of the model were constrained to move in-plane only. To prevent possible rotation of the entire model, which could increase convergence time, one edge of one element was fully constrained at the inlet and outlets. Vessel and plaque materials were implemented into the stress analysis as Demiray-type solids, as presented in section 2.3.2.

## 4.5 FSI Stress Analysis

The fluid-structure interaction stress analysis was performed in three distinct steps. The first step was a preparatory step in the two-stage analysis method of chapter 3. In this first step, a steady-state simulation was made so that the fluid and solid models could reach equilibrium at end-diastolic pressure, flow, and displacements conditions. Once end-diastolic conditions were reached, the two-stage method of chapter 3 was used to make the stress analysis. Because the FSI simulation was initialized using end-diastolic pressure and Womersley flow profiles, transients in the pressure field solution were negligible and only the first half of one cardiac cycle was simulated. Using two 0.01 second time steps, and twenty-five 0.015 second time steps, the first 0.395 seconds of the cardiac cycle were simulated so that accelerative and decelerative behavior could be observed. It was not known beforehand what cardiac phase would yield the greatest plaque stresses.

After identification of the cardiac phase at which plaque stresses were greatest, the flow and displacement solutions at the truncation planes were saved for use during the second stage of the analysis. A steady-state FSI analysis of this cardiac phase ( $t = 0.17$  seconds) was then performed on the refined mesh of the region of interest and the truncated fluid domain.

## 4.6 Results

### 4.6.1 First Stage Flow Results

The pressure distribution in the deformed carotid bifurcation is shown for  $t = 0.17$  s in Fig. 4.10a. Note that these results come from the first stage of the two-stage solution



method. Maximum pressure is seen at the apex of the bifurcation, where the kinetic energy of flowing blood is fully converted into stagnation pressure and strain energy within the deformable vessel wall. Just past the bifurcation, the pressure drops significantly in both the internal and external carotid artery. A further drop in pressure is seen at the narrowest part of the internal carotid artery, as a result of conservation of flow and conservation of energy.

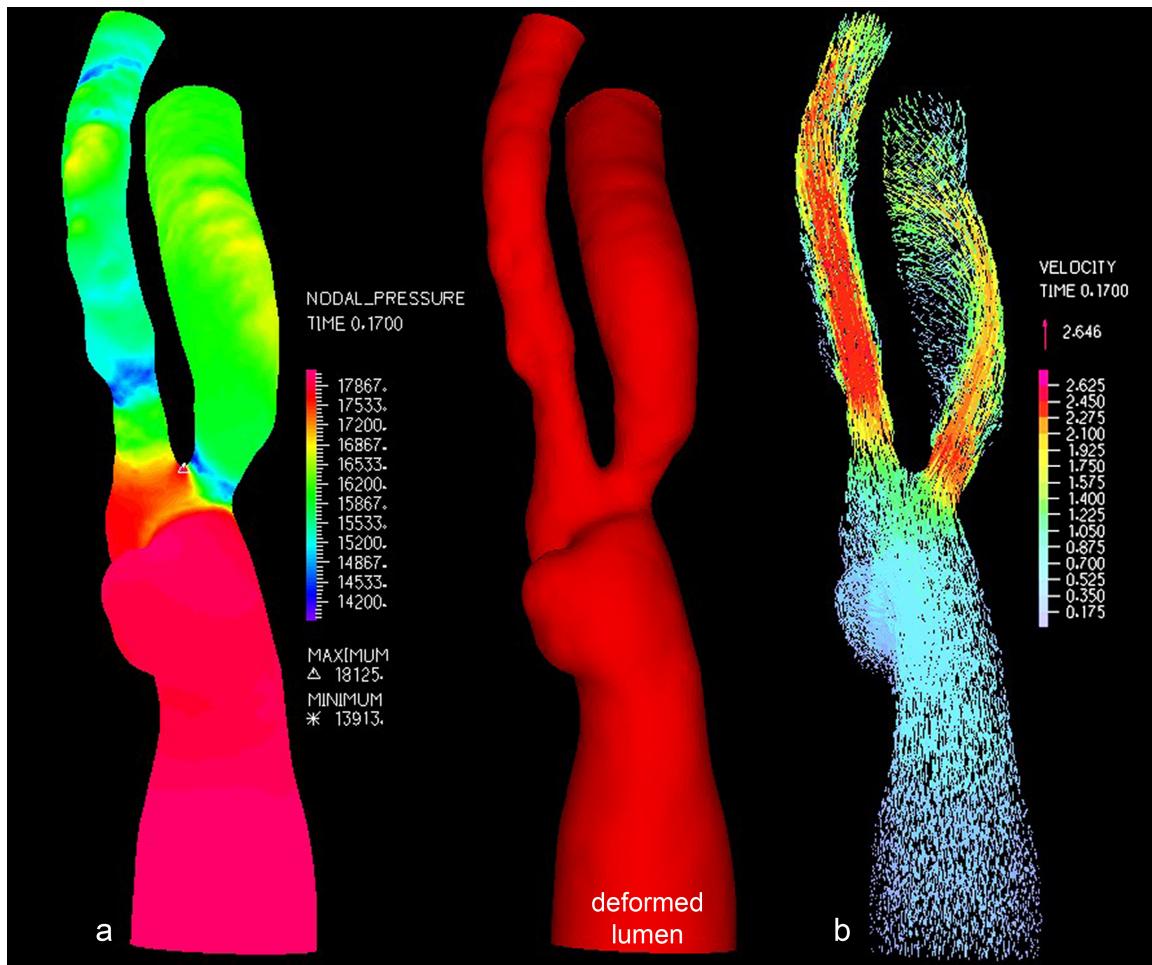


Fig. 4.10 a) Pressure field at  $t = 0.17$ s. Note the 2 kPa pressure drop at the stenotic throat of the ICA. b) Velocity field in the carotid bifurcation.

The velocity field is shown in Fig. 4.10b. Because of the severe lumen diameter reduction, the velocity of flowing blood rises sharply at the stenotic throat of the ICA, forming a pronounced jet structure. Another jet is formed at the proximal narrowing of the ECA, and it enters into a helical flow structure centered on the ECA lumen axis. At the impingement zones of each jet there are focal pressure increases nearing 1 kPa. A detailed view of some of the more prominent flow features is provided in Fig. 4.11. In the region of the ICA where plaque rupture occurred, there is flow recirculation in the focal enlargements of the lumen. There is an even stronger recirculation just proximal to the bifurcation, within the “pocket” formed by prior plaque ulceration. The recirculation in this pocket is fed by flow from the lateral aspect of the CCA, and the exiting flow is central to the CCA and feeds both the ICA and ECA. Fig. 4.11 also shows the complex multi-vortical structure of flow in the ECA.

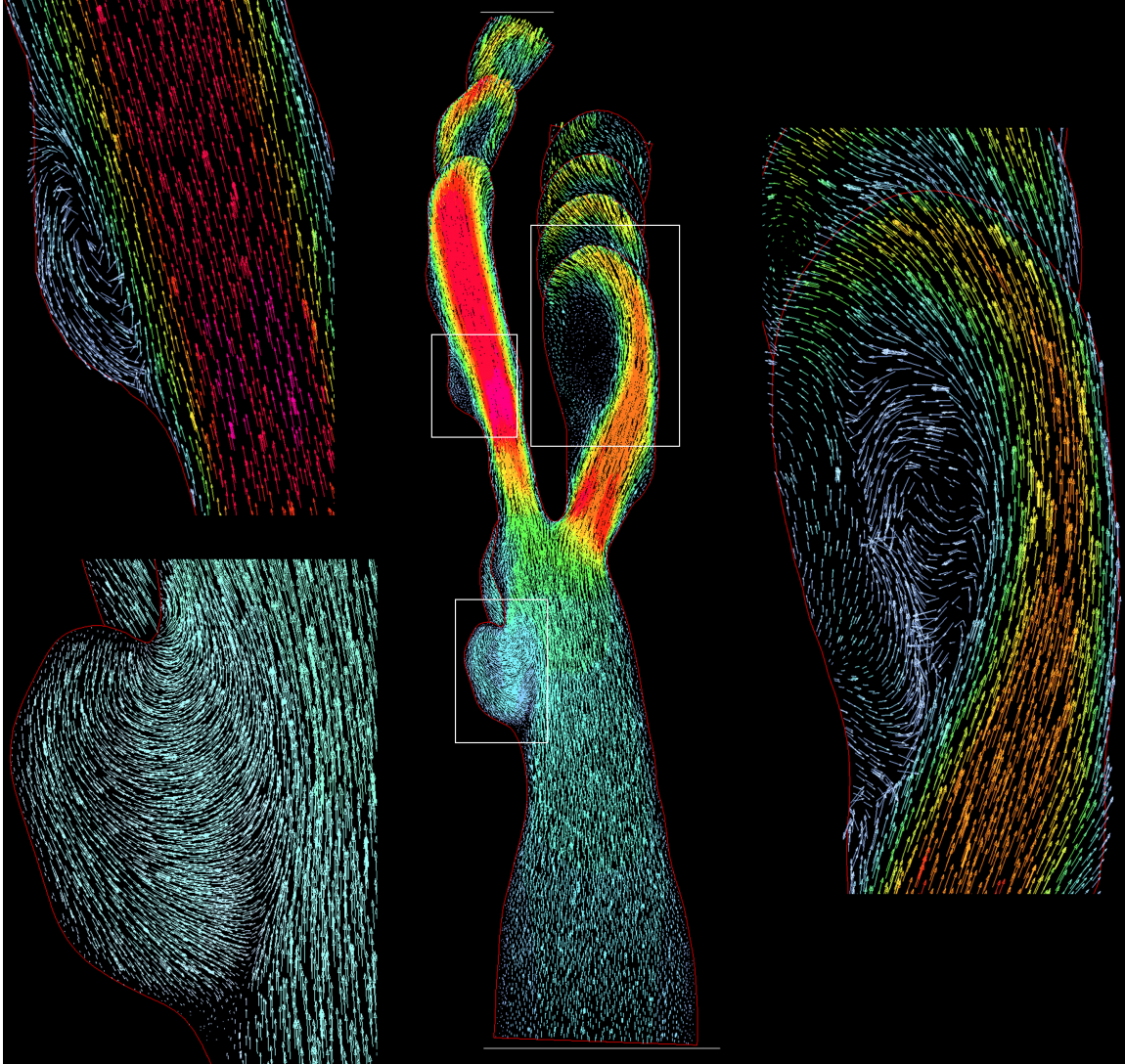


Fig. 4.11 Prominent features of the flow field shown on cut-planes through finite element mesh.

#### 4.6.2 Second-Stage Flow Results

The velocity and pressure solutions from  $t = 0.17$  s were saved during post-processing, and then assigned as flow boundary conditions in a truncated FSI simulation over the region of interest. The first stage's displacement solutions at the truncation planes were the sole boundary conditions on the truncated solid domain. A steady-state

simulation using these boundary conditions was run so that the stress field in the region of rupture could be calculated.

The pressure solution over the truncated fluid domain deviated by an average of 1.5% from the full-domain solution, and a detailed account of the deviation was provided in section 3.6.2. The accuracy of the second-stage's velocity field solution was not quantitatively investigated, although it is shown in Fig. 4.12 to be in close qualitative agreement with the first-stage solution.

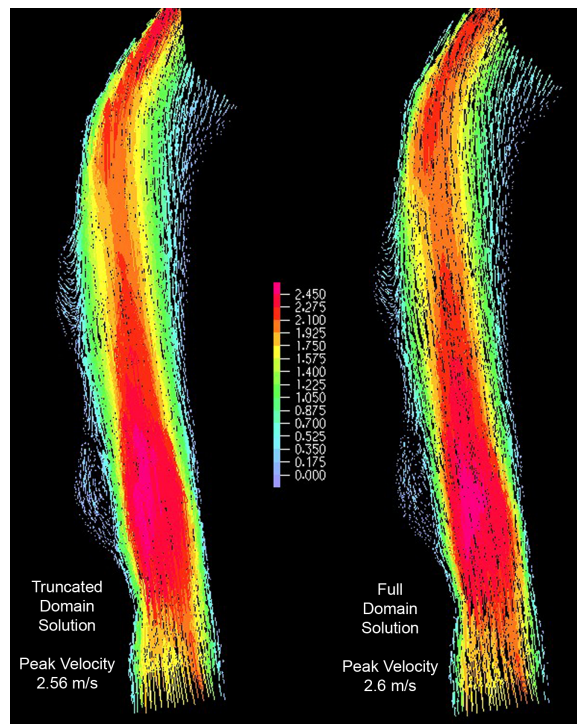


Fig. 4.12 Velocity field solutions shown on cut plane through region of interest. The second-stage solution agrees qualitatively with the accurate first-stage velocity field.

#### 4.6.3 Second-Stage Stress Results

Three-dimensional finite element analyses provide a wealth of information about the deformation and stresses experienced by a solid, and it is difficult to parse from the rich datasets the information of core relevance. Here, we are primarily interested in the

stress field within the region where plaque rupture occurred. Stresses were initially examined on several planes through the geometry, both axially and longitudinally oriented. After a thorough survey of the data, it was decided that the clearest simultaneous presentation of plaque stresses and plaque structure could be made using several axial cut-plane slices. A 14 mm spline curve of the ICA lumen centerline was constructed and used to define 15 planar slices, each normal to the local vessel axis, spanning the region where plaque rupture occurred. First principal stresses were examined on these slices to assess the mechanical environment of the pre-rupture lesion. First principal stress, the maximum value of normal stress obtained through coordinate transformation, was examined rather than the von Mises stress that is commonly used in the literature. Circumferential tensile stress is thought to be the predominant mechanical factor associated with fibrous plaque rupture, and in this geometry, the principle stress direction is tensile and primarily circumferential with regard to the lumen surface (Loree, Kamm et al. 1992; Loree, Grodzinsky et al. 1994; Holzapfel and Sommer 2004). The cut-plane slices for which stresses are presented are shown in Fig. 4.13 with respect to both the pre- and post-rupture lumina, which have been co-registered.

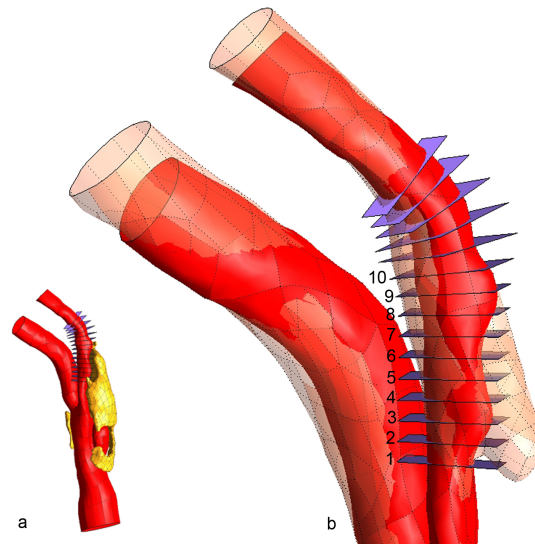


Fig. 4.13 Cut-plane slices on which stresses are presented. a) Slices shown with respect to full bifurcation and major lipid pool. b) Zoomed view of slices on pre-rupture lumen, shown with respect to post-rupture lumen (transparent peach color). Slices 1-6 span the region where rupture occurred.

It was found that slices 7-10 consistently experienced the lowest stresses in the region of plaque rupture, and slices 11-15 displayed no interesting stress patterns. For this reason, stress results are only discussed for slices 1-6. These stresses are shown in Fig. 4.14. The vessel wall outer boundary is drawn, and “w” denoted the healthy wall tissue, “Li” indicates regions of lipid pool at the slice level, “Lu” indicates the lumen. Many finite element studies of atherosclerotic vessels have revealed that plaque lipids do not support a great deal of stress due to their relative compliance. Our results showed this as well, with lipid stresses being compressive and within the range 500-2500 Pa. Stress patterns in the vessel wall were unremarkable, with tensile stresses in the range of 0-40 kPa, and a few very small regions of weakly compressive stress. For these reasons, stresses are only displayed for the fibrous plaque layer, allowing for the widest dynamic range to be used in the color plots. Additionally, stress within the fibrous plaque layer is the only stress of interest in this study of plaque rupture.

The stress fields reveal two strong stress concentrations at the intersections of the “major axis” of the roughly elliptical lumen and the fibrous plaque. In an idealized geometry with an elliptical lumen this is easily understood by considering the force balance of blood pressure and circumferential stress (Kumar and Balakrishnan 2005). In this case, where the lumen shape and fibrous plaque thickness are very irregular, the stress field is not symmetrical across the lumen and peak stress locations are influenced substantially by local fibrous plaque thickness, lipid pool volume and proximity, and lumen curvature.

A third stress concentration is also present on each slice, in the fibrous plaque contacting the lipid pool, directly over the portion of lipid pool closest to the lumen. The lipid pool is extremely compliant and the location of minimal fibrous plaque thickness overlying lipid pool experiences the most deformation. The deformation follows the pressure field, and is outward from the lumen, normal to the lumen surface. The focal (along the lumen circumference) outward deformation causes a bending mode of deformation, and is what gives rise to the characteristic stress pattern with three concentrations. A result of the bending mode is the concentration of compressive stress often seen at the lumen surface overlying the location of maximum lipid pool – lumen proximity. This pattern can be seen throughout the literature in plaque morphologies that are “one-sided” in the sense that the lipid pool is located approximately within a 180° span about the lumen centroid.

With the exception of slices 3 and 4, first principal (in this geometry, very nearly equivalent to circumferential) stress peaks are located in the region of plaque rupture. At slices 3 and 4, the fibrous plaque thickness at the location of peak stress is much smaller

than elsewhere in the geometry and this dominates over the effects of the lipid pool. The fibrous plaque stresses at the lumen surface are plotted on the lumen geometry and are shown in Fig. 4.15.



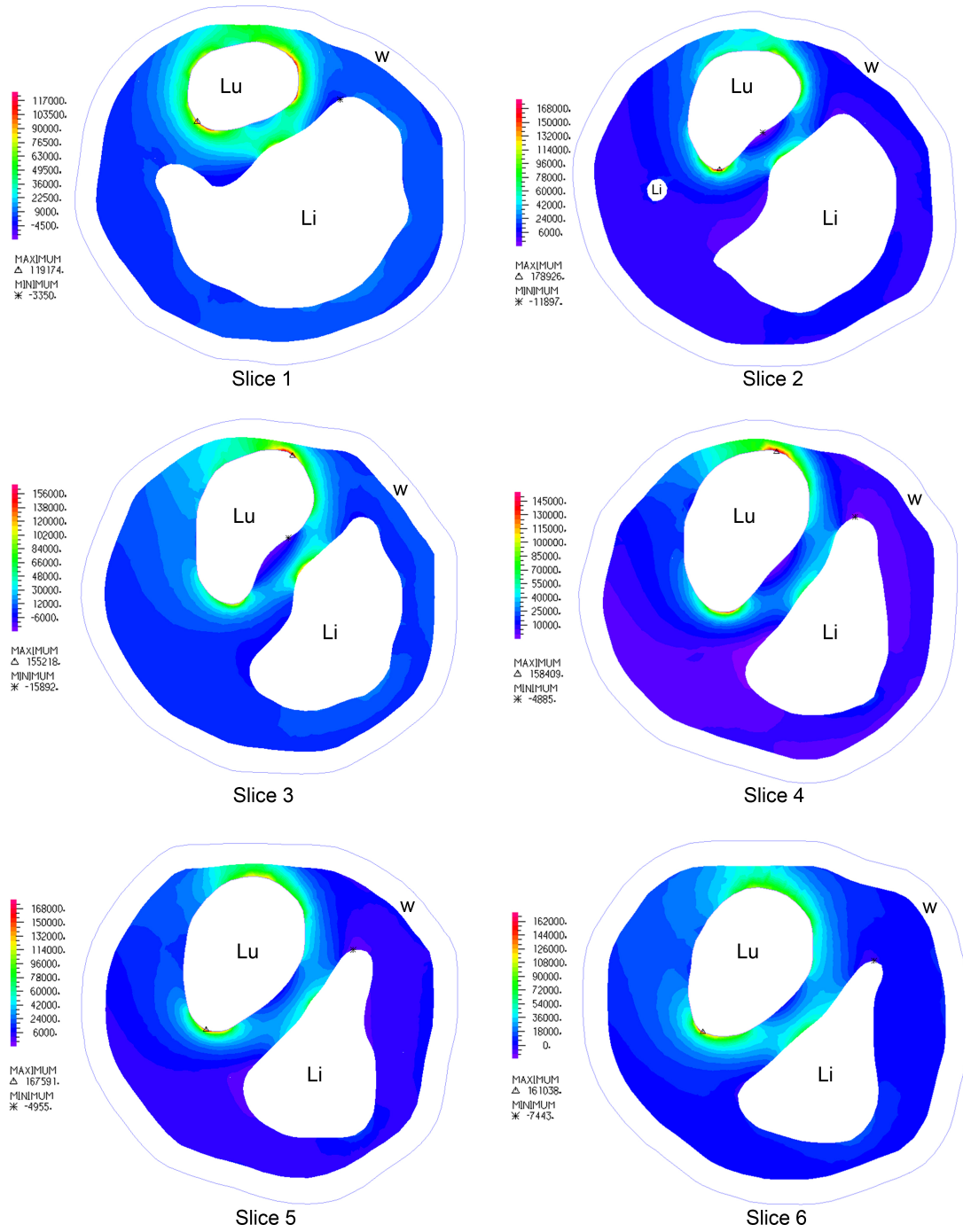


Fig. 4.14 First principal stress plotted for the fibrous plaque layer on slices 1-6. A separate scale is used for each slice to permit the best visualization of stress patterns. “w” indicates the vessel wall, “Li” indicates lipid pool, and “Lu” identifies the lumen at each slice.

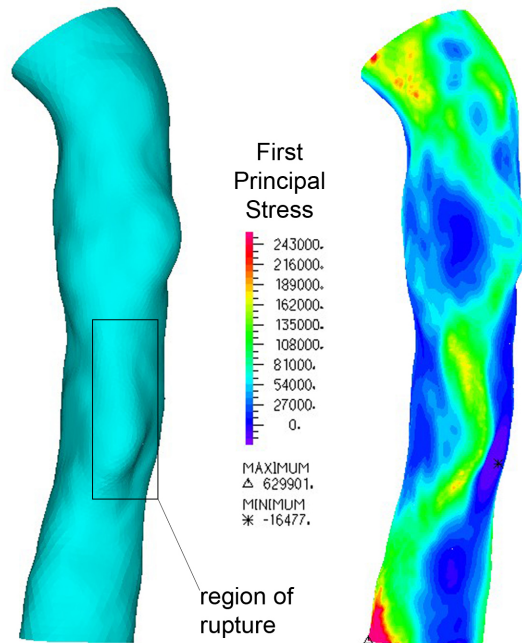


Fig. 4.15 Fibrous plaque stresses at the lumen surface, plotted on the lumen geometry. A modest elevation of stress is seen within the region where plaque rupture occurred.

A slight elevation of first principal stress is seen within the region of rupture at the lumen surface, however a much more prominent stress peak lies at the bottom of domain shown in Fig. 4.15. At this location, as shown in Fig. 2.20, the fibrous plaque layer is at least twice as thin as anywhere else in the geometry, and stresses are substantially higher.

Although four out of six slices demonstrate stress fields with maxima in the region of rupture, two slices do not. Furthermore, the predicted stress magnitudes are far below the often-cited fibrous plaque ultimate tensile strength of 300 kPa. While it is unlikely that 300 kPa is the absolute criterion for stress-based plaque rupture, several studies suggest that this is a reasonable estimate of rupture strength. Thus, the stresses

predicted by the FSI analysis do not clearly suggest that stress concentration was responsible for plaque rupture in this case.

## **4.7 Effects of Imaging Imprecision**

The primary structural features that correspond to increased plaque stresses are a large lipid core and a thin fibrous cap overlying the lipid core (Loree, Kamm et al. 1992; Cheng, Loree et al. 1993; Richardson 2002). Intra-plaque lipids are much less stiff than fibrous plaque, vessel wall, and calcification and are incapable of supporting the load imposed by systemic blood pressure. As a result of this stiffness mismatch, the fibrous cap carries a larger fraction of the systemic load and thus material stresses are greater. For this reason, an important determinant of a predictive model's utility is the accuracy of the geometry used. To better understand the effects of an improper representation of the plaque components several additional simulations were run, in which the geometry of the large lipid pool of Fig. 2.16 was modified in a manner consistent with imaging imprecision.

In CT and MR imaging, 3D datasets are built up from a set of discrete voxels, the image intensities of which are related to the nature of the material shown in each voxel. Because of the voxel's finite extent in each Cartesian direction, it is possible that more than one material is contained therein. In this case, the image intensity is a volume fraction-weighted average of each constituent's intensity. This effect is known as partial voluming, and it can lead to feature misinterpretation or inaccurate segmentation of a medical image. With in-plane resolutions on the order of 0.25 - 0.5 mm, current imaging modalities are susceptible to partial volume effects that could seriously alter an image-

based finite element model. An additional challenge in CT imaging is incomplete discrimination of lipid and fibrous plaque tissue. If the features are sufficiently large, a reasonable segmentation can be made, but errors can remain near the boundaries of lipid pools. This would affect the perceived fibrous cap thickness to lipid pool volume ratio, and could have an impact on model predictions.

To study the effects of imaging imprecision, the luminal face of a large lipid pool (the side of the pool closest to the lumen) was modified in this model. An adjusted luminal face of the lipid pool was generated as a constant offset surface from the original face in the direction of the local surface normal, using offsets of 0.2, 0.4, and 0.5 mm. In this way, lipid features were essentially preserved, and fibrous cap thickness was varied accordingly. The lipid pool geometry was only modified in the segment of the ICA containing the region of plaque rupture, as this would by far have the greatest impact on stresses there. In an effort to isolate the effects of reduced fibrous cap thickness from those of increased total lipid pool volume, only the surface of the lipid pool facing the lumen was modified. Thus, lipid volume was modestly increased without changing the entire lipid pool geometry. The dilated lipid pools are shown along with the lipid pool from the original segmentation in Fig. 4.16. The volumes of the baseline and modified lipid pools within the region of interest are listed in Table 4.4.

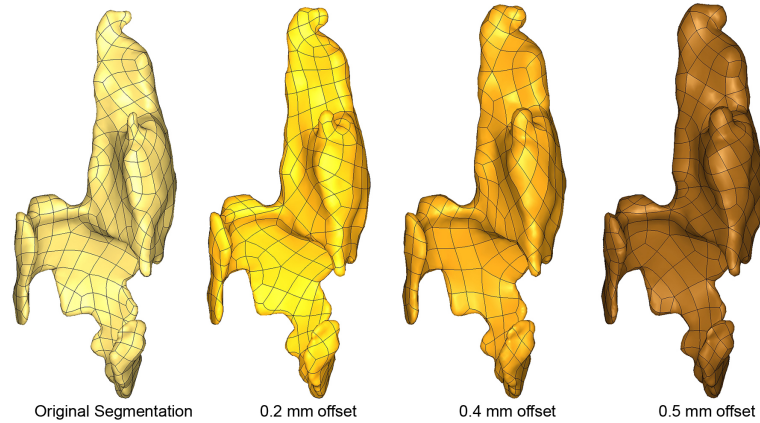


Fig. 4.16 Original and modified lipid pools. Note, only the upper half of the pool has been modified.

Surface Offset for Lipid Pool (mm)	Volume of Lipid Pool Contained in Region of Interest (mm <sup>3</sup> )
0 (baseline geometry)	150.19
0.2	171.07
0.4	194.09
0.5	206.5

Table 4.4 Volumes of original and modified lipid pools within region of interest.

The additional FSI simulations were run with the same boundary conditions and loading as the baseline simulation, and the two-stage solution method was again used. Due to a change in the stiffness of the diseased artery wall with different lipid pool boundaries, the pressurized lumen geometry varied slightly between different models. The effect of this difference on the converged pressure field solution was minimal, with maximum deviations from the baseline pressure field of 1.5% for the 0.2 mm offset case, 3% for the 0.4 mm offset case, and 5.4% for the 0.5 mm offset case. In each case, the largest deviations were near the boundary of the model and would not affect the wall stresses in the region of rupture appreciably. Stress predictions from the simulations with the progressively dilated lipid pool are shown in Figs. 4.17 (slices 1-3) and 4.18 (slices 4-

6). The results on each slice are shown on a color scale that most clearly shows the stress pattern in the 0.4 mm offset case.

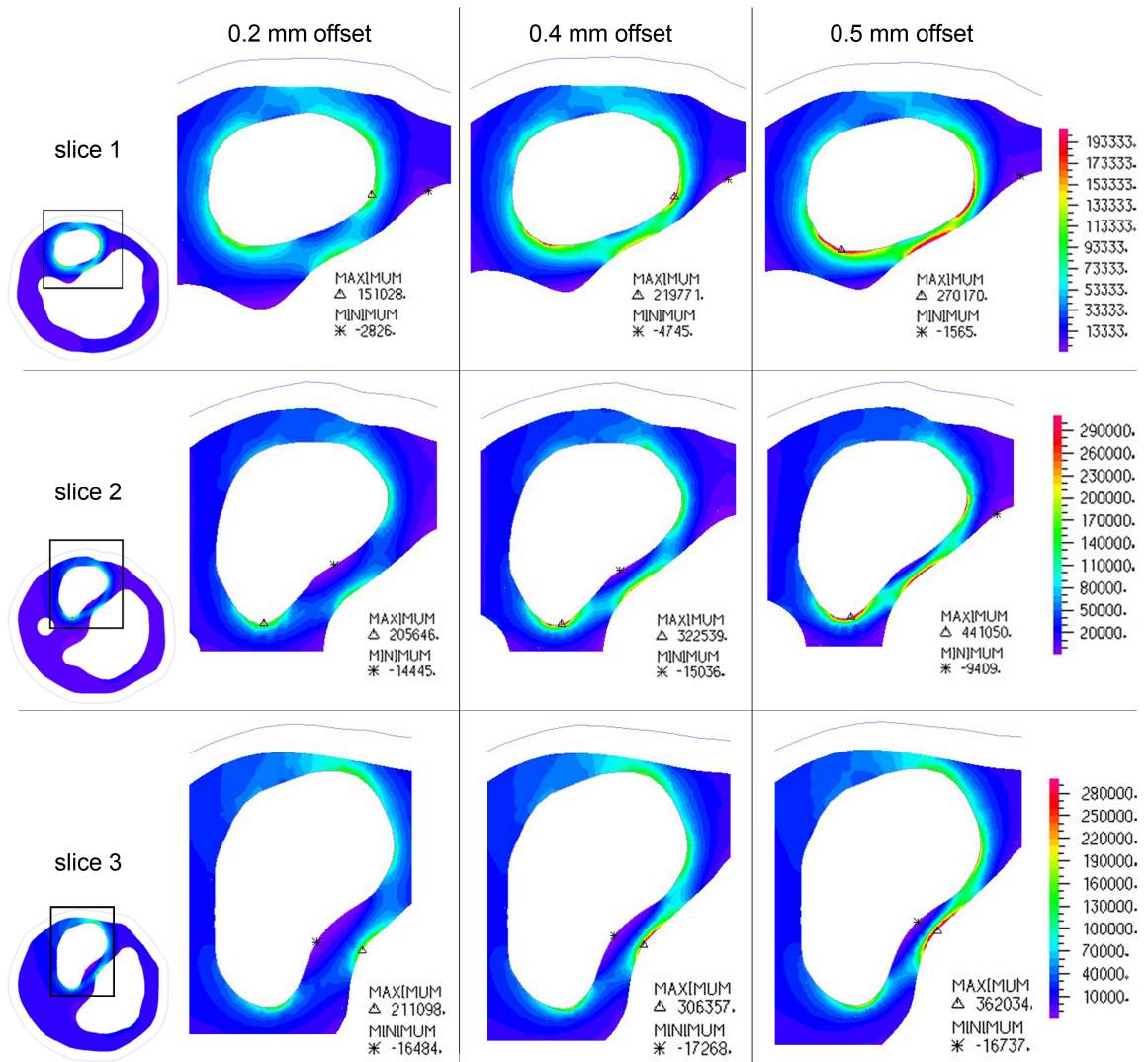


Fig. 4.17 Fibrous plaque stresses for slices 1-3. Stresses are shown for models with progressively dilated lipid pool. All three plots per slice use the same color scale for visualization of stress pattern changes.

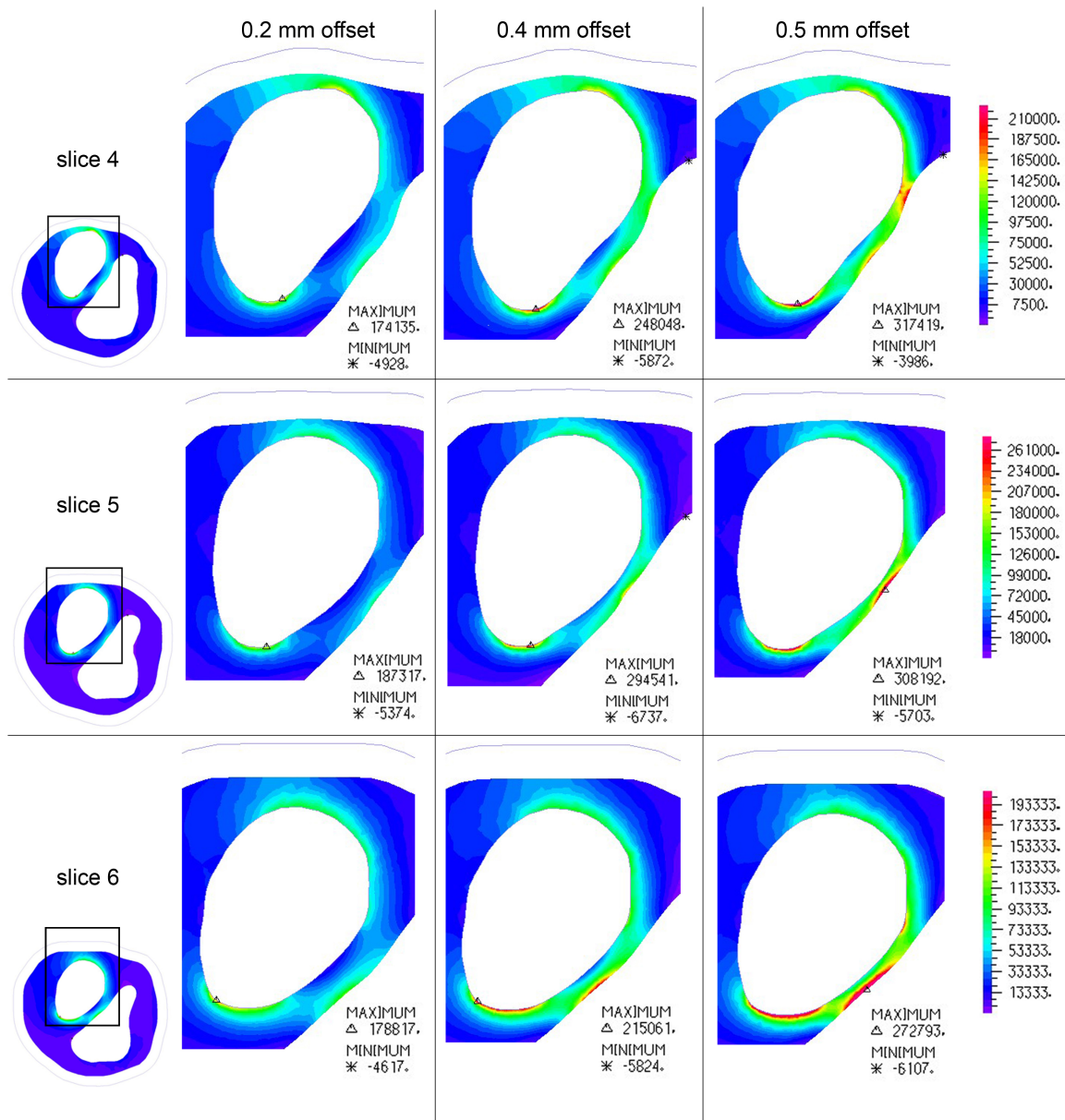


Fig. 4.18 Fibrous plaque stresses for slices 1-3. Stresses are shown for models with progressively dilated lipid pool. All three plots per slice use the same color scale for visualization of stress pattern changes.

As the large lipid pool is progressively dilated, the three-concentration pattern seen in the baseline model strengthens on all slices. Eventually the fibrous cap reaches a critical thickness, however, and acts more like a membrane. At this critical thickness, the bending mode that gives rise to compressive stress is no longer supported, and the entire

cap thickness is in a tensile stress state. It is possible that this transition plays a critical role in plaque stability for arteries with an eccentric lumen. Before this state, there is little communication of tensile stress around the circumference of the lumen, with stress concentrations being caused independently by both hoop stresses and bending deformation. Certain angular positions are effectively shielded from sharing the systemic pressure load. After the critical thickness is reached, the entire cap experiences a hoop stress and the destabilizing effects of reduced tissue integrity or increased load would be readily communicated throughout the fibrous cap. This is seen especially well in slices 1, 5, and 6, where the stress concentration in the fibrous plaque layer in contact with the lipid pool becomes contiguous with the concentrations at the lumen eccentricities. It is worth mentioning that this stress concentration, even at severely reduced fibrous cap thickness, is often not shown in the literature. In complex 3D finite element models, it is common to smooth element stresses at nodes so that a continuous stress field is displayed. Such smoothing makes data interpretation easier, and often increases the accuracy of stress predictions. Although often done in the literature, smoothing stress results across material boundaries is inappropriate, as only the strains must be consistent. Smoothing at the lipid pool boundary effectively masks stress concentrations in the fibrous plaque layer at the material interface, because the lipids support virtually no stress. This is shown in Fig. 4.19 for slice 5 in the model with a 0.5 mm lipid surface offset. Conclusions drawn from these inappropriately smoothed results can be dramatically different than those drawn from non-smoothed or properly smoothed nodal results.



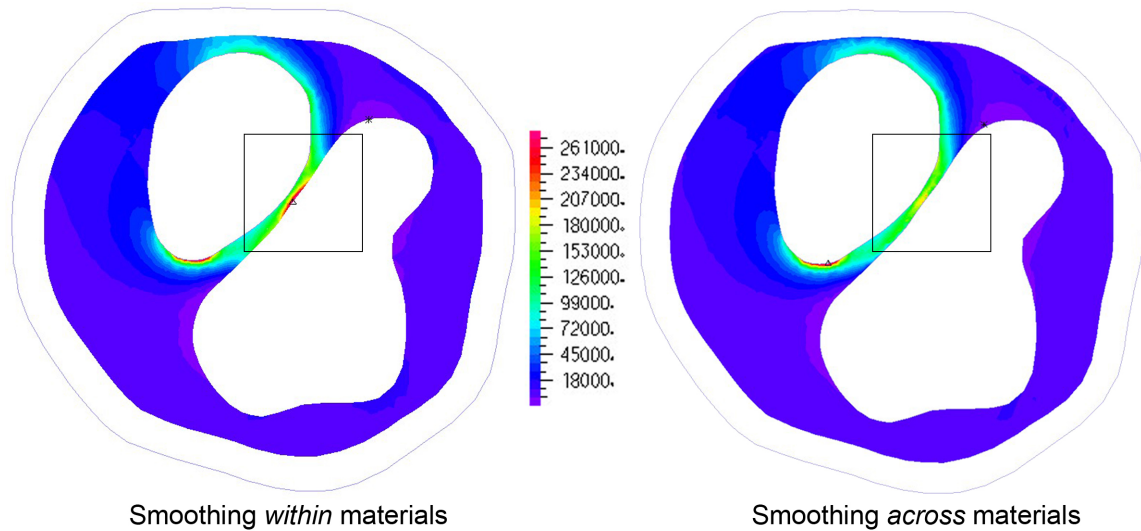


Fig. 4.19 (Left) Proper smoothing of element stress results, respecting material boundaries. (Right) Smoothing across material boundaries can be deleterious to critical stress features and is not appropriate. Note that the location of maximum stress changes considerably with different smoothing technique.

The effects of imprecision in imaging, segmentation, or geometric reconstruction on the predicted stress field within the region of rupture are reflected in the change in peak stress magnitude as the lipid pool is dilated. A small dilation of 0.2 mm causes the peak stress on all slices to lie within the region of rupture with an average magnitude increase of 18.4% (std. dev. 10.6%). A further dilation to a 0.4 mm offset, still less than a typical clinical imaging pixel width, causes an additional average peak stress magnitude increase of 44.6% (std. dev. 13.5%). The last 0.1 mm offset, to a total of 0.5 mm, causes a final 22.9% average increase (std. dev. 10.8%) in peak stress magnitude. When referenced to the baseline model, the 0.4 mm dilation causes an average increase in peak stress magnitude of 71.3% (std. dev. 22.8%), and the 0.5 mm dilation results in an average increase of 110% (std. dev. 30.2%). We must always keep this sensitivity in mind when using image-based biomechanical modeling for predictive purposes. The

trends in peak stress magnitude as a function of lipid pool dilation are shown for slices 1-10 in Fig. 4.20. Most slices examined show an exponential increase in peak stress with decreasing fibrous cap thickness.

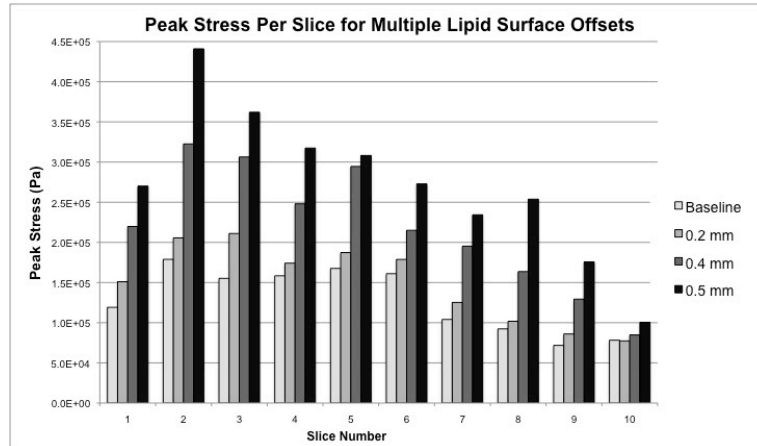


Fig. 4.20 Peak stress magnitude trends as a function of lipid dilation. Most slices show an exponential increase in peak stress with decreasing fibrous cap thickness.

The fibrous plaque stresses at the luminal surface are shown as a function of lipid pool dilation in Fig. 4.21. Although the global maximum stress is always located at the bottom of the domain shown, there is a band of elevated stress spanning the region of rupture. As the lipid pool is progressively dilated, there is a preferential increase in stress within the region of rupture, and the remaining geometry either remains unaffected or sees a modest increase in stress. At the small lipid dilation of 0.2 mm, there is a clear stress concentration within the region of rupture, isolated from the surrounding lumen surface, supporting the role of mechanical stress in plaque rupture. The local stress elevation becomes more obvious when the lipid pool is dilated by 0.4 mm, and the co-localization of stress and rupture location is shown in Fig. 4.22.

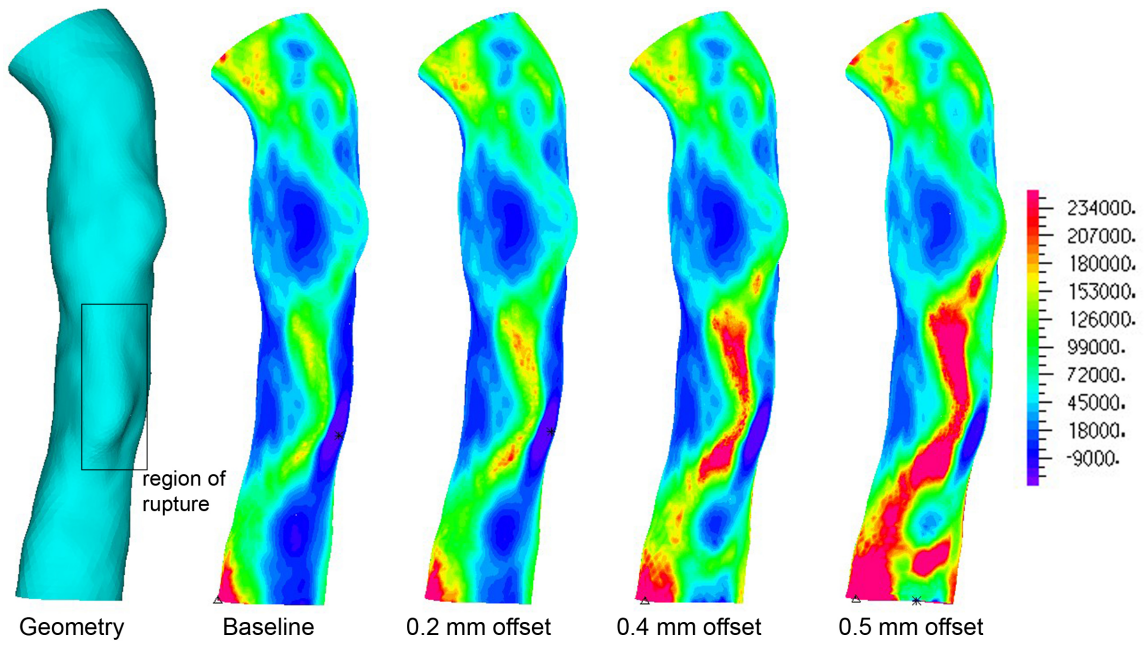


Fig. 4.21 Fibrous plaque stresses at lumen surface as a function of lipid pool dilation.

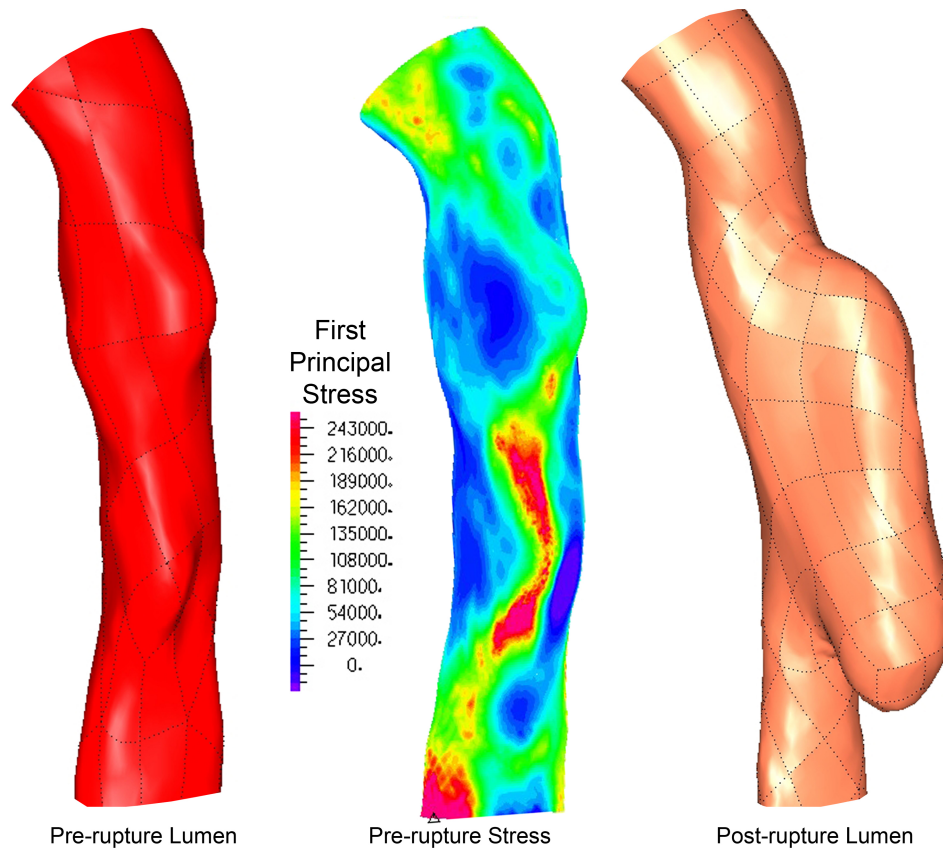


Fig. 4.22 Fibrous plaque stresses at the lumen surface for 0.4 mm lipid surface offset.

## Chapter 5 – Discussion and Future Work

### 5.1 Geometric Modeling and Two-Stage Solution

There are significant hurdles to be overcome before 3D FSI modeling of atherosclerotic carotid arteries can be done on a patient specific basis with the robustness, accuracy, ease and speed required for large scale investigations or clinical use. Two of the biggest procedural challenges are mesh generation and computation time. A computational mesh of brick elements, 8-node or higher order, generally provides more accurate stress results than a mesh of tetrahedral elements when the overall finite element system matrix is constrained to be of similar size. The morphology of the diseased vessel, with resolved plaque components, is not amenable to structured meshes, and unstructured meshes of tetrahedra become preferable for ease of mesh generation. Additionally, because it is difficult to assess *a priori* which region(s) of a diseased vessel might be of interest from a mechanics standpoint, it is important that the finite element model be able to consider highly complex shapes, something unstructured meshes are well suited for.

Simultaneously representing a portion of artery suitable for FSI analysis *and* accurately predicting plaque stresses over a large region using an unstructured mesh can easily require element counts in the several hundred thousands. To make matters worse, finite element codes employ special mixed-formulation tetrahedral elements to better handle material incompressibility. Such elements offer greatly enhanced stress predictions at the cost of an even larger system matrix than that obtained with standard displacement-formulation elements. FSI simulations of such large systems are

computationally very demanding and require a cluster with ample memory for reasonable run-times. For this reason, we have developed a two-stage approach that both eliminates the difficulty of structured mesh generation and significantly reduces the computation time associated with accurate unstructured meshes.

To facilitate unstructured mesh generation with the greatest amount of user control, an intermediate set of geometrical surfaces representing the boundaries of various vessel and plaque components was constructed from medical imaging data. By referencing a continuous surface rather than discrete image pixels, mesh generation is more flexible and better suited to complex geometries. Although multi-sequence black-blood MRI studies have excellent soft tissue contrast and are often used to study carotid plaques *in vivo* (Yuan and Kerwin 2004; Saam, Hatsukami et al. 2007), we have used CT-Angiography data for boundary surface extraction as it has an inherently smaller slice thickness. In principle, the same methods could be applied to MR data following appropriate re-sampling or interpolation of bounding curves, allowing surface generation via lofting to be avoided.

After a segmentation of the imaging study is achieved, an experienced user can generate the coarse and fine mesh models for both solid and fluid domains within a few hours. The surface meshes for each model can be constrained to lie within a user-defined tolerance in most unstructured mesh generators, ensuring a suitable FSI interface. While directly modeling each plaque component as a geometric solid would allow for an even easier conforming mesh generation scheme, this would not allow sufficient control over the anisotropic mesh density needed for these models.

The time-savings in mesh generation would not be valuable if the solution of the truncated model were not accurate. Our results for the further truncation of the region of interest show that coarse-mesh displacement results can be successfully employed as fine-mesh boundary conditions with minimal effect on the converged stress predictions. The full description of material stress is given by a second-order tensor with six unique entries, and the patterns for each stress entry throughout the geometry are complex and different (Tang, Yang et al. 2005). We have chosen to examine only the first principle stress, the maximum value of normal stress obtained through coordinate transformation, rather than the von Mises stress that is commonly used in the literature. In our models, the principle stress direction is tensile and primarily circumferential with regard to the lumen surface. Circumferential tensile stress is thought to be the predominant mechanical factor associated with fibrous plaque rupture, and thus the first principle stress was studied (Lee, Grodzinsky et al. 1991; Loree, Kamm et al. 1992; Holzapfel and Sommer 2004). In this work we showed that first-principal stresses are well preserved during the two-stage solution approach. The behavior of other stress and strain measures in the two-stage solution should be investigated as well, although representation of loading and boundary displacements with the accuracy achieved here should satisfy all requirements for their preservation.

The two-stage approach does not perfectly re-create the loading that would be experienced in the region of interest using the traditional, one-stage analysis. The perturbations are small, however, and affect the plaque stress fields to a degree well within the limits of uncertainty that could be introduced through other features and assumptions of the analysis. Some of the image-based uncertainties will be discussed in

the next section, but flow rates, systemic pressure, and even patient posture can introduce deviations from the loading simulated. That we model only one of the many physiological conditions the vessel experiences does not mean, however, that we should neglect certain features we know to be true. The goal of the two-stage approach, in this case, was maintaining a load distribution consistent with the pressure drop seen across the tight stenosis and the pressure peak at the flow jet impingement zone, while preserving the vessel displacement behavior at the boundary of the model. In this regard, the two-stage approach allows very realistic image-based simulations to be run in a timely manner on a modest multi-core workstation, which will hopefully allow for greater use of sophisticated FSI models of diseased arteries.

A more general two-stage approach should be developed, whereby nodal solutions from the coarse-grained model, and use of the element shape functions will allow passage of data to serve as boundary conditions in a fine-mesh model defined entirely separate from the coarse model. In this way, no initial designation of a region of interest is needed, and mesh generation for both models is even less constrained. This will allow for even easier mesh generation, and the avoidance of mesh density anisotropy at the truncation planes of the first-stage model. The focal refinement of the mesh at the truncation planes, to match the fine-mesh model, can cause degradation in the condition of the global system matrix and cause slower convergence in iterative numerical solution. Direct solvers were used here to achieve maximum computation time reduction, and so this was not investigated. In principle, time-savings will be achieved using the two-stage method with iterative solvers, allowing even larger simulations, but a

detailed understanding of condition number dependence on mesh design should be sought.

## **5.2 FSI Stress Analysis**

In this work a patient-specific stress analysis of an atherosclerotic plaque was made based on pre-rupture imaging data, with post-rupture imaging data available for localization of rupture site and extent. The region of plaque rupture coincides with a local elevation of first principal stress, and with increasing proximity of the lipid pool to the lumen, stresses rise dramatically. Within an imaging or segmentation error of less than half a clinical imaging pixel-width, a strong stress concentration is revealed at the rupture location.

In an effort to realistically model the mechanical environment of the heavily diseased carotid bifurcation considered, we have utilized a 3-dimensional finite element model with highly resolved plaque structures and fluid-solid interaction. These sophisticated image-based models are increasingly being used to augment the understanding of plaque mechanics provided by simpler 2D models, and models of idealized vessel and plaque geometries. It is hoped that patient-specific biomechanical models will have clinical utility in the characterization of atherosclerotic lesions, and in the optimization of individual patient's treatment plans.

Before these models find a real place in routine clinical management, however, a suitable mechanical descriptor, or a combination of multiple descriptors must be correlated to plaque rupture vulnerability. Several mechanical factors have been proposed to be relevant to the initiation of plaque rupture, drawing from both the fluid



mechanics and solid mechanics of diseased vessels. While low and oscillatory flow-induced wall shear stress have long been known to influence plaque initiation, the endothelial damage caused by extreme shear stress is now suspected to contribute to rupture due to both mechanical and biological effects (Gertz and Roberts 1990; Groen, Gijssen et al. 2007; Fukumoto, Hiro et al. 2008). Critical pressure and flow conditions in stenotic vessels have also been suspected as contributing to rupture initiation (Binns and Ku 1989; Tang, Yang et al. 1999). A strong pressure drop at the throat of a stenosis can cause arterial collapse locally, most severely during peak systolic flow, altering arterial wall and plaque stresses significantly from the homeostatic norm. Among the structural mechanical factors suspected to influence plaque vulnerability, cyclic stress/strain and maximum stress stand out as likely determinants of plaque rupture potential. Although both descriptors are related to the stress within plaque tissues, the mechanisms by which they influence plaque destabilization differ. Cyclic stressing and deformation of plaque tissues have been shown to cause local tissue damage at stresses far less than the tissue failure strength, and thus plaque rupture is being investigated as a fatigue process (McCord and Ku 1993; Bank, Versluis et al. 2000; Versluis, Bank et al. 2006). A more acute form of plaque rupture is thought to occur when local plaque stresses, particularly those in the fibrous cap region, exceed the tissue failure strength causing catastrophic damage. Accordingly, several studies have sought to quantify either the first principal or von Mises stresses in the fibrous caps of idealized and patient-specific lesions (Loree, Kamm et al. 1992; Cheng, Loree et al. 1993; Li, Howarth et al. 2007).

The mechanical analyses used to explore these possible rupture mechanisms have, with exception to that by Groen et al (Groen, Gijssen et al. 2007), used idealized diseased

vessel geometries, artificially repaired geometries from ruptured lesions, or have used histological features, structural features, or symptom status of the patient as a surrogate for rupture. Groen et al, used serial MRI data of a 67 year old woman with pre- and post-rupture imaging studies to show that a carotid plaque ruptured in a region of locally elevated wall shear stress. The study used a rigid-wall CFD model to determine wall shear stress throughout the carotid bifurcation, and thus was incapable of resolving plaque stresses resulting from systemic pressure. Without patient-specific flow boundary conditions, only a steady-state simulation with equal normal tractions at the ICA and ECA was presented. Although these assumptions and limitations can severely affect the CFD results, the study is important because it examines a plaque known to have ruptured and the analysis is based on pre-rupture imaging data. Given the rarity of pre- and post-rupture imaging data being available for a particular patient, it is important that these cases be analyzed and interpreted with the inherent modeling limitations in mind.

In some sense, the analysis presented here is complementary to that of Groen et al. We have chosen, as a first analysis, to study the material stresses in the region where a carotid plaque rupture occurred, rather than the flow-induced shear stress at the diseased vessel wall. The main limitation to performing a flow analysis for this case is the same as in Groen's study, namely the lack of detailed patient-specific flow boundary conditions. The ultrasound data available to us has limited potential in providing fully accurate flow boundary conditions. This certainly can have an effect on the solid mechanics results, but the effect would no doubt be greater in wall shear stress calculations. A careful parameter sensitivity study is warranted to comment on shear stress in this geometry.

While our result showing co-localization of elevated first principal stress and plaque rupture is compelling and suggests that maximum local stress might be a primary influence on plaque vulnerability, our study has a number of limitations and we therefore cannot make definitive statements about a cause of rupture. The stress field at the luminal surface shows the peak stress at a location outside the region of rupture, and other areas of stress concentration exist. Stress concentration outside of the rupture region occurs where the fibrous plaque layer is especially thin and *not* directly overlying the lipid pool. The fibrous plaque in these regions is roughly half as thick as that overlying the lipid pool in the region of rupture.

Other FEM studies have shown peak stresses outside of a suspected “vulnerable” region, often in a relatively healthy portion of vessel. These observations inspired the “critical site tracking” approach of Tang, in which only particular features of the stress field are used to draw conclusions about lesion vulnerability (Tang, Yang et al. 2005). We suspect that detailed regional information about the material response or ultimate tensile strength of the fibrous plaque would help to reduce the apparent stress paradox. Until such information is available, indirect measures of local tissue strength may be of some use. For instance, proteolytic activity from macrophage-expressed matrix metalloproteinases may be limited to some distance from the lipid core, suggesting that we weigh the influence of the stress-field based on location. The rapid progress in lesion-specific constitutive modeling (Khalil, Bouma et al. 2006; Karimi, Zhu et al. 2008) and inflammation imaging will surely increase the realism and reliability of predictive modeling (Howarth, Tang et al. 2008).

As already mentioned, lack of detailed patient-specific flow boundary conditions required modification of conditions from another patient for use in this model. Because of the computational intensity of this type of problem, only one cardiac cycle was simulated to obtain the results presented. Transient effects are often seen in flow simulations, requiring multiple cardiac cycles to be run before flow solutions are considered reliable. In our case, because the flow field and shear stress patterns were not of primary interest, these small transients were ignored. The primary cause of wall stress, systemic pressure, was within physiologic range and transient effects are thought to be of second-order importance here. A more lengthy analysis should be conducted to verify this.

Most finite element analyses of atherosclerotic arteries derive the arterial and plaque geometries from a multi-sequence black-blood MRI study. The ability to manipulate soft tissue contrast in MR imaging is far greater than that of other imaging modalities, and recent work has shown that this allows accurate characterization of carotid plaques (Yuan, Mitsumori et al. 2001; Saam, Ferguson et al. 2005; Saam, Hatsukami et al. 2007). Owing to relative cost and availability, however, MR studies are performed far less often for suspected cerebrovascular events than computed tomography studies, including non-contrast, angiographic (CTA), and perfusion scans (Culebras, Kase et al. 1997).

Keeping in mind the rarity of a pre-rupture scan, and an estimated yearly rupture rate less than 1%, finding an appropriate patient with available pre- and post-rupture MR data proves difficult. Our group maintains a database of over 100 patients with carotid disease followed longitudinally with MRI, and none were found to have pre- and post-

rupture imaging. The CTA data used for this model was found during a case-search for a different retrospective study. Although the soft tissue discrimination capabilities of CT imaging are less impressive than those of MRI, recent work has shown that carotid plaques can be characterized well if their features are suitably large (de Weert, Ouhlous et al. 2006; de Weert, de Monye et al. 2008; Wintermark, Jawadi et al. 2008).

Like other image-based models, ours has uncertainty in the plaque component and vessel wall boundaries. The effect of lipid-pool boundary error was explored here, and another study (Chau, Chan et al. 2004) shows that errors in the outer wall boundary have a negligible effect on fibrous cap stresses for similar geometries. Because the distinction between fibrous plaque and artery wall tissue cannot be made based on image intensity alone, local features were used to estimate a fibrous plaque outer boundary. The estimation of the fibrous plaque outer boundary was reviewed by a pathologist for realism, yet uncertainty remains high. Studies similar to this one often do not make a material distinction between fibrous plaque and vessel wall in the finite element model, even when multi-contrast MRI capable of this discrimination is used. This makes for easier computational mesh generation, but we feel that our estimation of the fibrous plaque outer boundary is less artificial than simply ignoring the boundary. Ignoring this boundary would add thickness to the fibrous plaque layer outside of the region of rupture and reduce the apparent “maximum stress-rupture point” paradox. In a second analysis of the model using a 0.5 mm lipid surface offset (not shown), we replaced the vessel wall material with fibrous plaque to investigate the effects of ignoring this boundary. The peak stress magnitudes at slices 1-10 changed, on average, by 4.53% (std. dev. 2.99%), with the greatest changes being at slices containing no lipid pool. For slices 2-6, the

average peak stress change was 2.59% from the model with a fibrous plaque / vessel wall boundary intact. For this lipid dilation, it therefore seems reasonable to ignore the fibrous plaque/vessel wall boundary if conclusions are drawn from the region spanned by slices 1-10, but such an assumption needs to be carefully justified for each geometry considered.

We attempted to separate the influence of a thinned fibrous cap from that of a total lipid pool volume increase by only offsetting the luminal face of the lipid pool. This was very difficult due to the highly irregular patient-specific geometry. The lipid pool volume increased roughly 14% for every 0.2 mm of surface offset, resulting in a maximum volume increase of 37.5% in the 0.5 mm offset case. Performing an offset of all the lipid pool surfaces would have resulted in a 40% volume increase for just the 0.2 mm offset case. A simple translation of the lipid pool toward the lumen, which would have preserved lipid features *and* volume, is not able to simulate the effects of segmentation error in all 3 dimensions and would cause preferential fibrous cap thinning in certain regions due to lumen and lipid pool curvature. Partial volume errors at the lumen/wall interface are also common and can affect finite element predictions, but adjusting luminal geometry would have a stronger impact on the pressure-field solution making comparisons between cases more difficult and less meaningful.

Finally, our analysis does not account for residual arterial stresses, patient-specific material properties, or material anisotropy. Residual stresses and material anisotropy are difficult to account for in a realistic 3D geometry, and the available imaging data could not provide information for this case. The “shrink-stretch” technique employed by Huang et al (Huang, Yang et al. 2009) makes an attempt to approximate the zero-stress

state of a carotid bifurcation based on *in vivo* and unloaded *ex vivo* MRI data. *Ex vivo* data was not available for this study, and assumptions on circumferential and axial shrinking would have been entirely artificial and without a means for error estimation. Additionally, it is not clear how to best shrink and expand a multi-component model in which different plaque features may have different behaviors. In a geometry where lumen and plaque feature curvature may play a significant role in material stress patterns, the use of such a technique may compromise geometrical features if not carefully employed.

Because of our assumption that the geometry from the CTA data was stress-free, our pressurized model expands more than those accounting for the no-load, stress-free state. As inlet velocity was assigned as a fluid boundary condition, the expansion of the artery led to a flow rate greater than that used to generate velocity boundary conditions. The flow rates obtained in the simulation were still within the observed physiologic range, however, and a correction was not sought. At the inlet of the CCA, where the vessel is relatively healthy and compliant, the stresses are of no interest in a plaque rupture study. An artificial gradient in material stiffness, from stiffer at the inlet to normal at the region of pronounced disease could help eliminate flow rate overestimation while preserving flow lumen geometry. The effects of this technique on stresses within the region of interest should be investigated. Obtaining a proper zero-stress state for FSI simulations is an important concern, and more work needs to be done to find a practical solution for multi-component models with complex geometries.

## Chapter 6 – Conclusion

In this work, a comprehensive strategy has been presented for the construction of geometrically faithful finite element models of atherosclerotic arteries, specifically the carotid bifurcation. Additional methods were developed to implement realistic patient-specific flow boundary conditions for fluid-structure interaction simulations. To address the steep computational resource and time demand inherent to these highly detailed and complex simulations, a two-stage solution method was introduced. The solution method compliments the model construction method, and accurate stress solutions are obtainable with less computational power and computing time than possible with traditional one-stage solution methods.

The methods of geometric reconstruction and finite element representation of physical boundary conditions were used to make a detailed fluid-structure interaction stress analysis of a carotid atheroma known to have ruptured. In addition to resolving stress fields within the region of plaque rupture, models with alternate lipid pool boundaries were used to investigate the effects of imprecision in medical imaging, segmentation or geometric reconstruction. The studies show that plaque rupture occurred at a location of first principal stress concentration, and provide the first data on physiologic plaque rupture supported by finite element analysis. The alternate models revealed that the stress field in the region of rupture is highly sensitive to geometric imprecision. Our results therefore suggest cautious optimism toward patient-specific predictive biomechanical modeling. The stress fields predicted are sensitive to sources of uncertainty, but they don't appear unstable and thus careful interpretation of patient-specific studies with error sources in mind may allow this type of work to achieve a real



clinical utility. The integration of recent and future advances in inflammation imaging and image-based material response determination will improve the capabilities of the modeling effort, and biomechanical analysis coupled with medical imaging will become increasingly powerful for research investigations and clinical management alike.

## References

- Aoki, S., K. Aoki, et al. (1999). "Dynamic MR imaging of the carotid wall." J Magn Reson Imaging 9(3): 420-7.
- Bank, A. J., A. Versluis, et al. (2000). "Atherosclerotic plaque rupture: a fatigue process?" Med Hypotheses 55(6): 480-4.
- Bassiouny, H. S., Y. Sakaguchi, et al. (1997). "Juxtalumenal location of plaque necrosis and neof ormation in symptomatic carotid stenosis." J Vasc Surg 26(4): 585-94.
- Bathe, K.-J. (1996). Finite element procedures. Englewood Cliffs, N.J., Prentice Hall.
- Bathe, K. J. and J. Dong (1987). "Solution of Incompressible Viscous Fluid Flow with Heat Transfer Using ADINA-F." Computers and Structures 26(1/2): 14.
- Bergel, D. H. (1960). The viscoelastic properties of the arterial wall, University of London. PhD.
- Binns, R. L. and D. N. Ku (1989). "Effect of stenosis on wall motion. A possible mechanism of stroke and transient ischemic attack." Arteriosclerosis 9(6): 842-7.
- Bond, R., K. Rerkasem, et al. (2003). "Systematic review of the risks of carotid endarterectomy in relation to the clinical indication for and timing of surgery." Stroke 34(9): 2290-301.
- Carew, T. E., R. N. Vaishnav, et al. (1968). "Compressibility of the arterial wall." Circulation Res. 23: 61-69.

- Carr, S., A. Farb, et al. (1996). "Atherosclerotic plaque rupture in symptomatic carotid artery stenosis." J Vasc Surg 23(5): 755-65; discussion 765-6.
- Carr, S. C., A. Farb, et al. (1997). "Activated inflammatory cells are associated with plaque rupture in carotid artery stenosis." Surgery 122(4): 757-63; discussion 763-4.
- Chau, A. H., R. C. Chan, et al. (2004). "Mechanical analysis of atherosclerotic plaques based on optical coherence tomography." Ann Biomed Eng 32(11): 1494-503.
- Cheng, G. C., H. M. Loree, et al. (1993). "Distribution of circumferential stress in ruptured and stable atherosclerotic lesions. A structural analysis with histopathological correlation." Circulation 87(4): 1179-87.
- Coli, S., M. Magnoni, et al. (2008). "Contrast-enhanced ultrasound imaging of intraplaque neovascularization in carotid arteries: correlation with histology and plaque echogenicity." J Am Coll Cardiol 52(3): 223-30.
- Conklin, B. S., R. P. Vito, et al. (2007). "Effect of low shear stress on permeability and occludin expression in porcine artery endothelial cells." World J Surg 31(4): 733-43.
- Culebras, A., C. S. Kase, et al. (1997). "Practice guidelines for the use of imaging in transient ischemic attacks and acute stroke. A report of the Stroke Council, American Heart Association." Stroke 28(7): 1480-97.
- Dammert, S., T. Krings, et al. (2004). "Detection of intracranial aneurysms with multislice CT: comparison with conventional angiography." Neuroradiology 46(6): 427-34.

- de Weert, T. T., C. de Monye, et al. (2008). "Assessment of atherosclerotic carotid plaque volume with multidetector computed tomography angiography." Int J Cardiovasc Imaging 24(7): 751-9.
- de Weert, T. T., M. Ouhlous, et al. (2006). "In vivo characterization and quantification of atherosclerotic carotid plaque components with multidetector computed tomography and histopathological correlation." Arterioscler Thromb Vasc Biol 26(10): 2366-72.
- Delfino, A. (1996). Analysis of stress field in a model of the human carotid bifurcation. Physics, Ecole Polytechnique Federale De Lausanne. PhD: 106.
- Dewey, C. F., Jr., S. R. Bussolari, et al. (1981). "The dynamic response of vascular endothelial cells to fluid shear stress." J Biomech Eng 103(3): 177-85.
- Diethrich, E. B., M. Paulina Margolis, et al. (2007). "Virtual histology intravascular ultrasound assessment of carotid artery disease: the Carotid Artery Plaque Virtual Histology Evaluation (CAPITAL) study." J Endovasc Ther 14(5): 676-86.
- Droste, D. W., M. Karl, et al. (1997). "Comparison of ultrasonic and histopathological features of carotid artery stenosis." Neurol Res 19(4): 380-4.
- Farrashkhalvat, M. and J. P. Miles (2003). Basic Structured Grid Generation with an introduction to unstructured grid generation. Oxford, Butterworth-Heinemann.

- Finlay, H. M., L. McCullough, et al. (1995). "Three-dimensional collagen organization of human brain arteries at different transmural pressures." J Vasc Res 32(5): 301-12.
- Forrester, J. S. (2007). The pathogenesis of atherosclerosis and plaque instability. Atherosclerosis and oxidant stress: A new perspective. J. L. Holtzman. New York, Springer US.
- Friedman, M. H. and D. P. Giddens (2005). "Blood Flow in Major Vessels - Modeling and Experiments." Ann Biomed Eng 33(12): 3.
- Fukumoto, Y., T. Hiro, et al. (2008). "Localized elevation of shear stress is related to coronary plaque rupture: a 3-dimensional intravascular ultrasound study with in-vivo color mapping of shear stress distribution." J Am Coll Cardiol 51(6): 645-50.
- Fung, Y. C., K. Fronek, et al. (1979). "Pseudoelasticity of arteries and the choice of its mathematical expression." Am. J. Physiol. 237: H620-H631.
- Gao, P., Z. Q. Chen, et al. (2007). "Correlation between carotid intraplaque hemorrhage and clinical symptoms: systematic review of observational studies." Stroke 38(8): 2382-90.
- Gasser, T. C., R. W. Ogden, et al. (2006). "Hyperelastic modelling of arterial layers with distributed collagen fibre orientations." J R Soc Interface 3(6): 15-35.
- Gertz, S. D. and W. C. Roberts (1990). "Hemodynamic shear force in rupture of coronary arterial atherosclerotic plaques." Am J Cardiol 66(19): 1368-72.

- Giannoni, M. F. and E. Vicenzini (2009). "Focus on the "unstable" carotid plaque: detection of intraplaque angiogenesis with contrast ultrasound. Present state and future perspectives." Curr Vasc Pharmacol 7(2): 180-4.
- Glagov, S., E. Weisenberg, et al. (1987). "Compensatory enlargement of human atherosclerotic coronary arteries." N Engl J Med 316(22): 1371-5.
- Granada, J. F., D. Wallace-Bradley, et al. (2007). "In vivo plaque characterization using intravascular ultrasound-virtual histology in a porcine model of complex coronary lesions." Arterioscler Thromb Vasc Biol 27(2): 387-93.
- Grant, E. G., A. J. Duerinckx, et al. (2000). "Ability to use duplex US to quantify internal carotid arterial stenoses: fact or fiction?" Radiology 214(1): 247-52.
- Groen, H. C., F. J. Gijzen, et al. (2007). "Plaque rupture in the carotid artery is localized at the high shear stress region: a case report." Stroke 38(8): 2379-81.
- Guyton, A. C. (1974). Cardiovascular physiology. London,, Butterworths;.
- Guyton, A. C. (1976). Textbook of medical physiology. Philadelphia, Saunders.
- Hatsukami, T. S., R. Ross, et al. (2000). "Visualization of fibrous cap thickness and rupture in human atherosclerotic carotid plaque in vivo with high-resolution magnetic resonance imaging." Circulation 102(9): 959-64.
- He, X., D. N. Ku, et al. (1993). "Simple calculation of the velocity profiles for pulsatile flow in a blood vessel using Mathematica." Ann Biomed Eng 21(1): 45-9.
- Holzappel, G. A. (2000). Nonlinear solid mechanics : a continuum approach for engineering. Chichester ; New York, Wiley.

- Holzapfel, G. A., T. C. Gasser, et al. (2000). "A new constitutive framework for arterial wall mechanics and a comparative study of material models." J. Elasticity 61: 1-48.
- Holzapfel, G. A. and G. Sommer (2004). "Anisotropic mechanical properties of tissue components in human atherosclerotic plaques." J Biomech Eng 126: 657-665.
- Holzapfel, G. A., G. Sommer, et al. (2005). "Determination of layer-specific mechanical properties of human coronary arteries with nonatherosclerotic intimal thickening and related constitutive modeling." Am. J. Physiol. Heart Circ. Physiol. 289: H2048-H2058.
- Holzapfel, G. A. and H. W. Weizsacker (1998). "Biomechanical behavior of the arterial wall and its numerical characterization." Comput Biol Med 28(4): 377-92.
- Howarth, S. P., T. Y. Tang, et al. (2008). "Utility of USPIO-enhanced MR imaging to identify inflammation and the fibrous cap: A comparison of symptomatic and asymptomatic individuals." Eur J Radiol.
- Huang, H., R. Virmani, et al. (2001). "The impact of calcification on the biomechanical stability of atherosclerotic plaques." Circulation 103: 1051-1056.
- Huang, X., C. Yang, et al. (2009). "Patient-specific artery shrinkage and 3D zero-stress state in multi-component 3D FSI models for carotid atherosclerotic plaques based on in vivo MRI data." Mol Cell Biomech 6(2): 121-34.

- Humphrey, J. D. (2002). Cardiovascular solid mechanics : cells, tissues, and organs.**  
New York, Springer.
- Imoto, K., T. Hiro, et al. (2005). "Longitudinal structural determinants of atherosclerotic plaque vulnerability: a computational analysis of stress distribution using vessel models and three-dimensional intravascular ultrasound imaging." J Am Coll Cardiol 46(8): 1507-15.**
- Jander, S., M. Sitzer, et al. (1998). "Inflammation in high-grade carotid stenosis: a possible role for macrophages and T cells in plaque destabilization." Stroke 29(8): 1625-30.**
- Joan, M. M., B. G. Moya, et al. (2009). "Utility of Intravascular Ultrasound Examination during Carotid Stenting." Ann Vasc Surg.**
- Kaazempur-Mofrad, M. R., H. F. Younis, et al. (2003). "Cyclic strain in human carotid bifurcation and its potential correlation to atherogenesis: Idealized and anatomically-realistic models." J. Eng. Math. 47: 299-314.**
- Kak, A. C. and M. Slaney (1988). Principles of computerized tomographic imaging.**
- Karimi, R., T. Zhu, et al. (2008). "Estimation of nonlinear mechanical properties of vascular tissues via elastography." Cardiovasc Eng 8(4): 191-202.**
- Kerwin, W. S., K. D. O'Brien, et al. (2006). "Inflammation in carotid atherosclerotic plaque: a dynamic contrast-enhanced MR imaging study." Radiology 241(2): 459-68.**
- Khalil, A. S., B. E. Bouma, et al. (2006). "A combined FEM/genetic algorithm for vascular soft tissue elasticity estimation." Cardiovasc Eng 6(3): 93-102.**



- Kock, S. A., E. T. Frund, et al. (2006). Stresses in carotid plaques using MRI-based fluid structure interaction models. Nordic COMSOL Conference, Copenhagen, Denmark.
- Kock, S. A., J. V. Nygaard, et al. (2008). "Mechanical stresses in carotid plaques using MRI-based fluid-structure interaction models." J Biomech 41(8): 1651-8.
- Kooi, M. E., V. C. Cappendijk, et al. (2003). "Accumulation of ultrasmall superparamagnetic particles of iron oxide in human atherosclerotic plaques can be detected by in vivo magnetic resonance imaging." Circulation 107(19): 2453-8.
- Ku, D. N., D. P. Giddens, et al. (1985). "Pulsatile flow and atherosclerosis in the human carotid bifurcation. Positive correlation between plaque location and low oscillating shear stress." Arteriosclerosis 5(3): 293-302.
- Kumar, R. K. and K. R. Balakrishnan (2005). "Influence of lumen shape and vessel geometry on plaque stresses: possible role in the increased vulnerability of a remodelled vessel and the "shoulder" of a plaque." Heart 91(11): 1459-65.
- Laflamme, K., C. J. Roberge, et al. (2006). "Adventitia contribution in vascular tone: insights from adventitia-derived cells in a tissue-engineered human blood vessel." Faseb J 20(8): 1245-7.
- Lafont, A. (2003). "Basic aspects of plaque vulnerability." Heart 89(10): 1262-7.
- Lee, J. S., H. J. Kang, et al. (2006). "MR imaging of in vivo recruitment of iron oxide-labeled macrophages in experimentally induced soft-tissue infection in mice." Radiology 241(1): 142-8.

- Lee, R. T., A. J. Grodzinsky, et al. (1991). "Structure-dependent dynamic mechanical behavior of fibrous caps from human atherosclerotic plaques." Circulation 83(5): 1764-70.
- Lee, S. W. and D. A. Steinman (2007). "On the relative importance of rheology for image-based CFD models of the carotid bifurcation." J Biomech Eng 129(2): 273-8.
- Lell, M. M., K. Anders, et al. (2006). "New techniques in CT angiography." Radiographics 26 Suppl 1: S45-62.
- Lendon, C. L., M. J. Davies, et al. (1991). "Atherosclerotic plaque caps are locally weakened when macrophage density is increased." Atherosclerosis 87: 87-90.
- Li, Z.-Y., S. P. S. Howarth, et al. (2007). "Structural analysis and magnetic resonance imaging predict plaque vulnerability: A study comparing symptomatic and asymptomatic individuals." J. Vascular Surg. 45: 768-775.
- Li, Z. Y., S. Howarth, et al. (2006). "Stress analysis of carotid plaque rupture based on in vivo high resolution MRI." J Biomech 39(14): 2611-22.
- Li, Z. Y., S. P. Howarth, et al. (2006). "How critical is fibrous cap thickness to carotid plaque stability? A flow-plaque interaction model." Stroke 37(5): 1195-9.
- Libby, P. (2002). "Atherosclerosis: the new view." Sci Am 286(5): 46-55.
- Loftus, I. M., A. R. Naylor, et al. (2000). "Increased matrix metalloproteinase-9 activity in unstable carotid plaques. A potential role in acute plaque disruption." Stroke 31(1): 40-7.

- Loree, H. M., A. J. Grodzinsky, et al. (1994). "Static circumferential tangential modulus of human atherosclerotic tissue." J Biomech 27(2): 195-204.
- Loree, H. M., R. D. Kamm, et al. (1992). "Effects of fibrous cap thickness on peak circumferential stress in model atherosclerotic vessels." Circ Res 71: 850-858.
- Loree, H. M., B. J. Tobias, et al. (1994). "Mechanical properties of model atherosclerotic lesion lipid pools." Arterioscler Thromb 14(2): 230-4.
- Lovett, J. K. and P. M. Rothwell (2003). "Site of carotid plaque ulceration in relation to direction of blood flow: an angiographic and pathological study." Cerebrovasc Dis 16(4): 369-75.
- Maiellaro, K. and W. R. Taylor (2007). "The role of the adventitia in vascular inflammation." Cardiovasc Res 75(4): 640-8.
- Mann, J. and M. J. Davies (1999). "Mechanisms of progression in native coronary artery disease: role of healed plaque disruption." Heart 82(3): 265-8.
- McCord, B. and D. N. Ku (1993). Mechanical rupture of the atherosclerotic plaque fibrous cap. Trans 1993 ASME Bioeng Conf.
- Milei, J., J. C. Parodi, et al. (1996). "Carotid atherosclerosis. Immunocytochemical analysis of the vascular and cellular composition in endarterectomies." Cardiologia 41(6): 535-42.
- Molloy, K. J., M. M. Thompson, et al. (2004). "Unstable carotid plaques exhibit raised matrix metalloproteinase-8 activity." Circulation 110(3): 337-43.

- Moore, W. S., H. J. Barnett, et al. (1995). "Guidelines for carotid endarterectomy. A multidisciplinary consensus statement from the Ad Hoc Committee, American Heart Association." Circulation 91(2): 566-79.
- Morey, S. S. (1998). "AHA updates guidelines for carotid endarterectomy." Am Fam Physician 58(8): 1898, 1903-4.
- Moyle, K. R., L. Antiga, et al. (2006). "Inlet conditions for image-based CFD models of the carotid bifurcation: is it reasonable to assume fully developed flow?" J Biomech Eng 128(3): 371-9.
- Nagano, K., H. Yamagami, et al. (2008). "Quantitative evaluation of carotid plaque echogenicity by integrated backscatter analysis: correlation with symptomatic history and histologic findings." Cerebrovasc Dis 26(6): 578-83.
- Naghavi, M., P. Libby, et al. (2003). "From vulnerable plaque to vulnerable patient: a call for new definitions and risk assessment strategies: Part II." Circulation 108(15): 1772-8.
- Nair, A., B. D. Kuban, et al. (2002). "Coronary plaque classification with intravascular ultrasound radiofrequency data analysis." Circulation 106(17): 2200-6.
- Nerem, R. M., M. J. Levesque, et al. (1981). "Vascular endothelial morphology as an indicator of the pattern of blood flow." J Biomech Eng 103(3): 172-6.
- Patel, D. J. and D. L. Fry (1969). "The elastic symmetry of arterial segments in dogs." Circ Res 24(1): 1-8.
- Patel, S. Y., M. R. Kaazempur-Mofrad, et al. (2003). 2003 Summer Bioengineering Conference, Sonesta Beach Resort in Key Biscayne, Florida.

- Qiao, Y., A. Farber, et al. (2008). "Images in cardiovascular medicine. Healing of an asymptomatic carotid plaque ulceration." Circulation 118(10): e147-8.
- Redgrave, J. N., J. K. Lovett, et al. (2006). "Histological assessment of 526 symptomatic carotid plaques in relation to the nature and timing of ischemic symptoms: the Oxford plaque study." Circulation 113(19): 2320-8.
- Richardson, P. D. (2002). "Biomechanics of plaque rupture: Progress, problems, and new frontiers." Ann Biomed Eng 30: 524-536.
- Richardson, P. D., M. J. Davies, et al. (1989). "Influence of plaque configuration and stress distribution on fissuring of coronary atherosclerotic plaques." Lancet 2(8669): 941-4.
- Rosamond, W., K. Flegal, et al. (2007). "Heart disease and stroke statistics--2007 update: a report from the American Heart Association Statistics Committee and Stroke Statistics Subcommittee." Circulation 115(5): e69-171.
- Ross, R. (1999). "Atherosclerosis--an inflammatory disease." N Engl J Med 340(2): 115-26.
- Saam, T., J. Cai, et al. (2006). "Comparison of symptomatic and asymptomatic atherosclerotic carotid plaque features with in vivo MR imaging." Radiology 240(2): 464-72.
- Saam, T., M. S. Ferguson, et al. (2005). "Quantitative evaluation of carotid plaque composition by in vivo MRI." Arterioscler Thromb Vasc Biol 25(1): 234-9.
- Saam, T., T. S. Hatsukami, et al. (2007). "The vulnerable, or high-risk, atherosclerotic plaque: noninvasive MR imaging for characterization and assessment." Radiology 244(1): 64-77.

- Schulte-Altendorneburg, G., D. W. Droste, et al. (2002). "Detection of carotid artery stenosis by in vivo duplex ultrasound: correlation with planimetric measurements of the corresponding postmortem specimens." Stroke 33(10): 2402-7.
- Shinnar, M., J. T. Fallon, et al. (1999). "The diagnostic accuracy of ex vivo MRI for human atherosclerotic plaque characterization." Arterioscler Thromb Vasc Biol 19(11): 2756-61.
- Sary, H. C., A. B. Chandler, et al. (1995). "A definition of advanced types of atherosclerotic lesions and a histological classification of atherosclerosis. A report from the Committee on Vascular Lesions of the Council on Arteriosclerosis, American Heart Association." Arterioscler Thromb Vasc Biol 15(9): 1512-31.
- Sary, H. C., A. B. Chandler, et al. (1994). "A definition of initial, fatty streak, and intermediate lesions of atherosclerosis. A report from the Committee on Vascular Lesions of the Council on Arteriosclerosis, American Heart Association." Circulation 89(5): 2462-78.
- Stoll, G. and M. Bendszus (2006). "Inflammation and atherosclerosis: Novel insights into plaque formation and destabilization." Stroke 37: 1923-1932.
- Tang, D., C. Yang, et al. (2004). "Effect of a lipid pool on stress/strain distributions in stenotic arteries: 3-D fluid-structure interactions (FSI) models." J Biomech Eng 126(3): 363-70.

- Tang, D., C. Yang, et al. (2003). "Effect of stenosis asymmetry on blood flow and artery compression: A three-dimensional fluid-structure interaction model." Ann Biomed Eng 31: 1182-1193.
- Tang, D., C. Yang, et al. (1999). "A 3-D thin-wall model with fluid-structure interactions for blood flow in carotid arteries with symmetric and asymmetric stenoses." Computers and Structures 72 : 357-377.
- Tang, D., C. Yang, et al. (2005). "Local maximal stress hypothesis and computational plaque vulnerability index for atherosclerotic plaque assessment." Ann Biomed Eng 33(12): 1789-801.
- Tang, D., C. Yang, et al. (2005). "Quantifying effects of plaque structure and material properties on stress distributions in human atherosclerotic plaques using 3D FSI models." J Biomech Eng 127(7): 1185-94.
- Tang, D., C. Yang, et al. (2004). "3D MRI-based multicomponent FSI models for atherosclerotic plaques." Ann Biomed Eng 32(7): 947-60.
- Trivedi, R. A., U. K.-I. JM, et al. (2004). "MRI-derived measurements of fibrous-cap and lipid-core thickness: the potential for identifying vulnerable carotid plaques in vivo." Neuroradiology 46(9): 738-43.
- Vengrenyuk, Y., S. Carlier, et al. (2006). "A hypothesis for vulnerable plaque rupture due to stress-induced debonding around cellular microcalcifications in thin fibrous caps." Proc Natl Acad Sci U S A 103(40): 14678-83.
- Versluis, A., A. J. Bank, et al. (2006). "Fatigue and plaque rupture in myocardial infarction." J Biomech 39: 339-347.

- Virmani, R., A. P. Burke, et al. (2002). "Pathology of the unstable plaque." Prog Cardiovasc Dis 44(5): 349-56.
- Virmani, R., A. P. Burke, et al. (2006). "Pathology of the vulnerable plaque." J Am Coll Cardiol 47(8 Suppl): C13-8.
- Virmani, R., A. P. Burke, et al. (2003). "Pathology of the thin-cap fibroatheroma: a type of vulnerable plaque." J Interv Cardiol 16(3): 267-72.
- Virmani, R., E. R. Ladich, et al. (2006). "Histopathology of carotid atherosclerotic disease." Neurosurgery 59(5 Suppl 3): S219-27; discussion S3-13.
- Wintermark, M., S. S. Jawadi, et al. (2008). "High-resolution CT imaging of carotid artery atherosclerotic plaques." AJNR Am J Neuroradiol 29(5): 875-82.
- Womersley, J. R. (1955). "Mathematical theory of oscillating flow in an elastic tube." J Physiol 127(2): 37-8P.
- Younis, H. F., M. R. Kaazempur-Mofrad, et al. (2003). "Computational analysis of the effects of exercise on hemodynamics in the carotid bifurcation." Ann Biomed Eng 31(8): 995-1006.
- Yuan, C. and W. S. Kerwin (2004). "MRI of atherosclerosis." J Magn Reson Imaging 19(6): 710-9.
- Yuan, C., W. S. Kerwin, et al. (2002). "Contrast-enhanced high resolution MRI for atherosclerotic carotid artery tissue characterization." J Magn Reson Imaging 15(1): 62-7.
- Yuan, C., L. M. Mitsumori, et al. (2001). "Carotid atherosclerotic plaque: noninvasive MR characterization and identification of vulnerable lesions." Radiology 221(2): 285-99.



- Yushkevich, P. A., J. Piven, et al. (2006). "User-guided 3D active contour segmentation of anatomical structures: significantly improved efficiency and reliability." Neuroimage 31(3): 1116-28.**
- Yushkevich, P. A., H. Zhang, et al. (2005). "Parametric medial shape representation in 3-D via the Poisson partial differential equation with non-linear boundary conditions." Inf Process Med Imaging 19: 162-73.**
- Zienkiewicz, O. C. and R. L. Taylor (2000). The Finite Element Method (Fifth Edition) Volume 1: the Basis. Oxford, Butterworth-Heinemann.**

# Appendix

The following are a series of MatLab codes developed to implement the methods described in chapter 2. The codes are designed to accept nodal coordinate files as output directly from ADINA. For the work in this dissertation, each code was run sequentially to achieve a mapped Womersley profile. A more streamlined, one-step code is possible, but was not made. There is no friendly user interaction in these codes, and assignment of input data or code options is to be done by changing the codes themselves. Any questions about these codes (which are admittedly a little sloppy) can be sent to [joeleachis@gmail.com](mailto:joeleachis@gmail.com)

## 1 - FOURIER\_RECON.m

**Using flow rate waveforms as input, this code makes a Fourier decomposition of the waveform into a user-defined number of modes.**

```
cd 'C:\CURRENT_DIRECTORY';

type = 1; %1 for CCA BC, 2 for ICA BC

if(type ==1)
[time flow]= textread('cca_flow_new.txt', '%f %f', 'delimiter',
\t','headerlines', 1);
vector_size = size(time,1);
else
[time flow]= textread('ica_flow_new.txt', '%f %f', 'delimiter',
\t','headerlines', 1);
vector_size = size(time,1);
end

V = (flow(1:vector_size))';
tt = time(1:vector_size)';

plot(tt,V,'b-',tt,V,'ro')
title('Measured data')
%
% Number of data points
%
N=size(tt,2);
%
% Period
%
t1=double(tt(N));
t0=double(tt(1));
p=t1-t0;
```

```

tttt=double([0:p/50:p]);

ttt=double(tttt+t0*ones(size(tttt)));
%
% time increments Delta-t's
%
dt=tt(2:N)-tt(1:N-1);
%
% f_0(t) = 1, a_0 zeroth order Fourier coeff.
% using trapezoidal rule
%
a0=sum((V(2:N)+V(1:N-1))/2).*dt)/p;

hold on
c0=ones(size(ttt));
app=a0*c0;
plot(tt,V,'k-',tt,V,'bo',ttt,app)%,'r-',tt+p,V,'k-
',tt+p,V,'bo',ttt+p,app,'r-')
title('Zeroth order Fourier approximation')

% INPUT NUMBER OF MODES TO USE
M=20;

aa=double(zeros(1,M));
bb=double(zeros(1,M));
for k=1:M
    %pause(1.2)
    %
    % Evaluate the shifted sines and cosines at sample times

    %
    ck=cos(2*pi*k*(tt-t0*ones(size(tt)))/p);
    sk=sin(2*pi*k*(tt-t0*ones(size(tt)))/p);
    %
    % Multiply the data against the weight functions cos(kt) and
    sin(kt)
    %
    Vck=ck.*V;
    Vsk=sk.*V;

    %
    % Trapezoidal rule
    %
    ak=2*sum((Vck(2:N)+Vck(1:N-1))/2).*dt)/p;
    bk=2*sum((Vsk(2:N)+Vsk(1:N-1))/2).*dt)/p;
    %
    % Store newly computed coefficients for later access in arrays

```

```

%
aa(k)=ak;
bb(k)=bk;
app=app+ak*cos(tttt*2*pi/p*k)+bk*sin(tttt*2*pi/p*k);

if(k >= 15)
plot(tt,V,'k-',tt,V,'bo',ttt,app)%,'r-',tt+p,V,'k-
',tt+p,V,'bo',ttt+p,app,'r-')

mytitle=strcat('Fourier approximation of order ',num2str(k));
title(mytitle)
%pause
end
end
hold off
plot([1:M],aa,'b-',[1:M],bb,'g-',[1:M],sqrt(aa.*aa+bb.*bb),'r-
',[1,M],[0,0],'k-')

title('Fourier coefficients = spectrum of the signal')

OUT = cell(M,3);

if(type ==1)
fid = fopen('CCA_flow_Fourier_rep.txt', 'wt');
else
fid = fopen('ICA_flow_Fourier_rep.txt', 'wt');
end

fprintf(fid, '%20s\n', 'Mode#      Real      Im');
fprintf(fid, '%-i\t%-f\t%-f\n', [0 a0 0]);
for i = 1:1:M
OUT{i,1} = i;
OUT{i,2} = aa(1,i);
OUT{i,3} = bb(1,i);
fprintf(fid, '%-i\t%-f\t%-f\n', OUT{i,:});
end

status = fclose(fid);

```

## 2 - FLOW\_READER.m

**This code plots the original flow waveform and the reconstruction from the Fourier decomposition so the user can verify that the approximation using a limited number of modes is acceptable.**

```
cd 'C:\Documents and Settings\JOe\Desktop\Womersley Mapping';
```

```

if(type ==1)
    [mode, real_amp, imag]= textread('CCA_flow_Fourier_rep.txt', '%u %f
%f', 'delimiter', '\t','headerlines', 1);
    true_flow = flow;%cca_flow_smooth;
else
    [mode, real_amp, imag]= textread('ICA_flow_Fourier_rep.txt', '%u %f
%f', 'delimiter', '\t','headerlines', 1);
    true_flow = ica_flow_smooth;
end
im = (-1)^.5;

flow_recon = (zeros(1,vector_size))';

for i = 1:1:size(mode,1)-1
    flow_recon = flow_recon + real( (real_amp(i)+ im*imag(i))*exp(-
im*mode(i)*2*pi*time/time_max));
end

figure; plot(time,flow_recon, time, true_flow, 'r-');

```

### 3 – ROTATOR\_TESTER.m

**This code determines the transformation described in chapter 2, where the inlet or outlet mesh nodes are aligned with the global z-axis in preparation for Womersley profile mapping. The user must hard-code the mesh normal, centroid, and a vector from the centroid to a boundary node. The code outputs a transformation matrix that can be applied to nodal coordinates.**

```

centroid = [-.00919285 .01475428 .01207068]; %CCA new_seg

normal = [-.00131891 -.00047938 .00787976]; % old_seg CCA% in global
%frame

normal = normal/norm(normal); %in global frame

vec1 = [-.0132284 .0122919 .0630082]; % ICA new_seg

vec1 = vec1-centroid;
vec1 = vec1/norm(vec1);

vec2 = cross(normal, vec1);
vec2 = vec2/norm(vec2);

line_of_nodes = [-normal(2)*1 normal(1) 0];%/((normal(2)^2 +
normal(1)^2)^.5);

```

```

proj_lon_x = line_of_nodes*[1 0 0]';
proj_lon_y = line_of_nodes*[0 1 0]';

alpha = atan(proj_lon_y/proj_lon_x);
alpha = mod(alpha, 2*pi);

proj_z_Z = dot(normal,[0 0 1]');

beta = atan(norm(line_of_nodes)/(proj_z_Z));
beta = mod(beta, pi);

gamma = atan(vec1(3)/vec2(3));
gamma = -atan(proj_lon_y/proj_lon_x);
gamma = mod(gamma, 2*pi);

R1 = [cos(alpha) -sin(alpha) 0;sin(alpha) cos(alpha) 0;0 0 1];
R2 = [1 0 0;0 cos(beta) -sin(beta);0 sin(beta) cos(beta)];
R3 = [cos(gamma) -sin(gamma) 0;sin(gamma) cos(gamma) 0;0 0 1];
R = (R1*R2*R3);
R_extra = (R1*R2*R3)';

trans = inv(R)*normal'
trans_extra = inv(R_extra)*normal'

if (normal == [0 0 1])
    trans = [1 0 0; 0 1 0; 0 0 1];
    trans_extra = [1 0 0; 0 1 0; 0 0 1];
end

```

#### 4 – NODE\_TRANSFORMER.m

**This code applies the transformation from ROTATOR\_TESTER.m to the inlet or outlet mesh, aligning its normal with the global z-axis.**

```

cd 'C:\CURRENT_DIRECTORY';

[nums, x, y, z, sys]= textread('all_nodes.txt', '%u %f %f %f %f',
'delimiter', '\t');

if(type == 1)
    [meat, gar1, gar2]= textread('cca_meat.txt', '%u %u
%u','delimiter', '\t');
else
    [meat, gar1, gar2]= textread('ica_meat.txt', '%u %u
%u','delimiter', '\t');

```

```

end

%trans_matrix = R_extra; %may be R or R_extra
trans_matrix = R;

x_transformed = zeros(size(nums, 1),1);
y_transformed = zeros(size(nums, 1),1);
z_transformed = zeros(size(nums, 1),1);

for i = 1:size(nums, 1)
    node = nums(i);
    original_vec = [x(node) y(node) z(node)] - centroid;
    transformed_vec = inv(trans_matrix)*original_vec';
    x_transformed(i)= transformed_vec(1);
    y_transformed(i)= transformed_vec(2);
    z_transformed(i)= transformed_vec(3);
end

```

## 5 – WOMERSLEY\_TRANSFORMED.m

The code reads in the Fourier representation of the flow boundary conditions and constructs a Womersley profile, then maps this profile to the inlet or outlet mesh nodes. A steady-state profile at a user-specified cardiac phase is output, as well as time functions for each node so that the dynamic profile may be assigned as an FEM boundary condition. There are 3 modes for this code. Mode 0 will output the peak velocity of the profile at the cardiac phase of interest, allowing for a quick test of the input data. Mode 1 will output the profiles and time functions for the mesh. Mode 3 will generate a 3D triangulated surface representation of the mapped dynamic Womersley profile.

```

cd 'C:\Documents and Settings\JOe\Desktop\Womersley Mapping';

movietype = 1; % zero for quick tests of max vel.....1 for
output.....3 for 3D plot
TOTAL_MODES = 20;

if(type ==1)
    [bound, gar11, gar22]= textread('cca_bound.txt', '%u %u
    %u','delimiter', '\t');
else
    [bound, gar11, gar22]= textread('ica_bound.txt', '%u %u
    %u','delimiter', '\t');
end

```

```

if(type ==1)
[modes, real_amps, imags]= textread('cca_flow_Fourier_rep.txt', '%u %f
%f', 'delimiter', '\t','headerlines', 1);
else
[modes, real_amps, imags]= textread('ica_flow_Fourier_rep.txt', '%u %f
%f', 'delimiter', '\t','headerlines', 1);
end

if(type ==2)
    start = 296;    %starting time-function to output
else
    start = 0;
end

% mL to m^3 conversion
    real_amps = real_amps/1e6;
    imags = imags/1e6;

x = z_transformed;
y = x_transformed;
z = y_transformed;

output_time = .02;
vel_dir = '1';

period = time_max;
ang_freq = 2*pi/period;
dt = 0.01;

time = 0:dt:period;
viscosity = .0035;
dens = 1060;

centroid = [0 0 0]; %WRT the new coord. system!!!

%----calculate equivalent area-----%
% k = convhull(x_transformed,y_transformed);    % NO LONGER USED
% eq_area = polyarea(x_transformed(k),y_transformed(k));
%-----%
%NEED TO FIX THE EQUIVALENT AREA!!!
if(type == 1)
eq_area = 54.27/(10^6);

```



```

else
eq_area = 8.94/(10^6);
end

eq_circ_rad = ((eq_area/pi)^.5);
eq_circ_rad = 0.004;

%----Initialize variables-----%
eq_rad = zeros(size(meat,1),1);
eq_rel_pos = zeros(size(meat, 1),2);
avg_rad = zeros(size(meat,1),1);
%-----%

%----Step through inlet surface nodes and calculate-----
%----position and distance from centroid, boundary intersection-----
for i = 1:size(meat, 1)
    node = meat(i);
    x_node = x(node);
    y_node = y(node);
    z_node = z(node);

    distance_node = ((y_node)^2 + (z_node)^2 )^.5;

    angle_node = atan((z_node - centroid(3))/(y_node - centroid(2)));

    node_coords = [y_node z_node];

    Transform = [cos(angle_node) sin(angle_node);-sin(angle_node)
cos(angle_node)];

    rotated_coords = Transform*(node_coords - [centroid(2)
centroid(3)]);

    dx = zeros(size(bound,1),1);
    dy = zeros(size(bound,1),1);
    dz = zeros(size(bound,1),1);

    sorting_array = zeros(size(bound, 1), 3);

%-----sort through boundary nodes to find boundary intersection----
--

    for j = 1:size(bound,1)
        bound_node = bound(j);
        x_bound = x(bound_node);

```

```

y_bound = y(bound_node);
z_bound = z(bound_node);

bound_coords = [y(bound_node) z(bound_node)];
ss = Transform*(bound_coords - [centroid(2) centroid(3)])';

    dy(j) = ss(2);

ss = Transform*(bound_coords - [centroid(2) centroid(3)])';

    dz(j) = ss(1);

    sorting_array(j,1)= bound_node;
    sorting_array(j,2) = abs(dy(j));
    sorting_array(j,3) = dz(j);
end

%-----Now, Sort by dy-----
sorted = sortrows(sorting_array, 2);

count = 0;
k = 0;
while count < 2

    if (y_node - centroid(2)) < 0

        if sorted(1+k,3) < 0
            if count == 0
                node_match1 = sorted(1+k,1);
                node_disty1 = sorted(1+k,2);
                node_distz1 = sorted(1+k,3);
            else
                node_match2 = sorted(1+k,1);
                node_disty2 = sorted(1+k,2);
                node_distz2 = sorted(1+k,3);
            end
            count = count+1;
            k = k+1;
        else
            k = k+1;
        end

    else

        if sorted(1+k,3) > 0

```

```

        if count == 0
            node_match1 = sorted(1+k,1);
            node_disty1 = sorted(1+k,2);
            node_distz1 = sorted(1+k,3);
        else
            node_match2 = sorted(1+k,1);
            node_disty2 = sorted(1+k,2);
            node_distz2 = sorted(1+k,3);
        end
        count = count+1;
        k = k+1;
    else
        k = k+1;
    end
end

end

%-----Record equivalent distance from origin in Womersley circle-----
-

    sum_z = node_distz1 + node_distz2;

    dissy1 = (node_disty1^2 + node_distz1^2)^.5;
    dissy2 = (node_disty2^2 + node_distz2^2)^.5;

    avg_rad(i) = ((node_distz1/sum_z)*dissy2 +
(node_distz2/sum_z)*dissy1);

    eq_rel_pos(i,1) = node;
    eq_rel_pos(i,2) = distance_node/avg_rad(i)*eq_circ_rad;

end

%-----Make Womersley Profile-----

wom_vels = zeros(size(meat, 1),round(period/dt),5);

im = (-1)^.5;
for i = 1:1:size(meat, 1)

    r = eq_rel_pos(i,2);

    wom_vels(i,:,2) = (1-

```

```

(r/eq_circ_rad)^2)*real_amps(1)*2/(pi*eq_circ_rad^2);
end

for i = 1:1:size(meat, 1)

    r = eq_rel_pos(i,2);

    for t = time(1):dt:period

        for mode = 2:1:TOTAL_MODES
            mode_num = modes(mode);
            rea = real_amps(mode);
            imaginar = imags(mode);

            lambda_sq = im^3*mode_num*ang_freq*dens/viscosity;

            FTP = (-
            rea+im*imaginar)*im*mode_num*ang_freq/(pi*eq_circ_rad^2*(1-
            2*bessel(1,eq_circ_rad*lambda_sq^.5)/((eq_circ_rad*lambda_sq^.5)*bessel
            (0,eq_circ_rad*lambda_sq^.5)))));
            wom_vels(i, round((t+dt)/dt), 1) = t;
            wom_vels(i, round((t+dt)/dt), 2) = wom_vels(i,
            round((t+dt)/dt),2)+ real(((FTP*dens)/(viscosity*lambda_sq))*(1 -
            (besselj(0,(lambda_sq^.5)*r)/besselj(0,(lambda_sq^.5)*eq_circ_rad))))*ex
            p(im*mode_num*ang_freq*t));

            end

        end

    end

    %CORRECT LAST VELOCITY TIME POINT
    wom_vels(:,time_max/dt+1, 2) = wom_vels(:,1,2);

    wom_vels(i, :, 3)= x(eq_rel_pos(i,1));
    wom_vels(i, :, 4)= y(eq_rel_pos(i,1));
    wom_vels(i, :, 5)= z(eq_rel_pos(i,1));

    end

%-----DISPLAY MOVIE-----
if (movietype == 0);
    max_vel = max(wom_vels(:,1,2))
    min_vel = min(wom_vels(:,1,2))

```

```

elseif (movietype == 1);
%
% for t = time(1):dt:period
%     r_max = .04;
%     index = round((t+dt)/dt);
%
%     vel_vec = [0 wom_vels(21,index,2) wom_vels(20,index,2)
wom_vels(19,index,2) wom_vels(39,index,2) wom_vels(38,index,2)
wom_vels(1,index,2) wom_vels(2,index,2) wom_vels(3,index,2) 0];
%
%
%     plot(vel_vec);
%     axis([1 10 -.5 2.3])
%     F(index) = getframe;
%     pause(.0001)
% end
% movie(F,5)

bound_points = zeros(size(bound,1),3);
for n=1:size(bound)
    bound_points(n,1) = y(bound(n));
    bound_points(n,2) = z(bound(n));
    bound_points(n,3) = 0;
end
%-----Generate Nodal Steady-State Velocity Input File for ADINA-----
-----%
OUTss = cell(size(meat, 1),5);
fid = fopen('OUTss.txt', 'wt');
fprintf(fid, '%50s\n', 'Node #      Load Type  Weight      Time
Function... Arrival Time      Birth Time  Death Time');
for i = 1:1:size(meat, 1)
    OUTss{i,1} = eq_rel_pos(i,1);
    OUTss{i,2} = vel_dir;
    OUTss{i,3} = wom_vels(i, (output_time-dt)/dt, 2);
    OUTss{i,4} = 1;
    OUTss{i,5} = 0.0;
    fprintf(fid, '%-i\t%-s\t%-f\t%-i\t%-f\n', OUTss{i,:});
end
for i = 1:1:size(bound,1)
    OUTss{i,1} = bound(i,1);
    OUTss{i,2} = vel_dir;
    OUTss{i,3} = 0;
    OUTss{i,4} = 1;
    OUTss{i,5} = 0.0;
    fprintf(fid, '%-i\t%-s\t%-f\t%-i\t%-f\n', OUTss{i,:});

```

```

end

fclose(fid);

%-----Generate Nodal Transient Velocity Input File for ADINA-----
-%
OUTt = cell(size(meat, 1),5);
fid = fopen('OUTt.txt', 'wt');
fprintf(fid, '%50s\n', 'Node #      Load Type  Weight      Time
Function... Arrival Time      Birth Time  Death Time');
for i = 1:size(meat, 1)
    OUTt{i,1} = eq_rel_pos(i,1);
    OUTt{i,2} = vel_dir;
    OUTt{i,3} = 1;
    OUTt{i,4} = i+start;
    OUTt{i,5} = 0.0;
    fprintf(fid, '%-i\t%-s\t%-f\t%-i\t%-f\n', OUTt{i,:});
end
for i = 1:size(bound,1)
    OUTt{i,1} = bound(i,1);
    OUTt{i,2} = vel_dir;
    OUTt{i,3} = 0;
    OUTt{i,4} = 1;
    OUTt{i,5} = 0.0;
    fprintf(fid, '%-i\t%-s\t%-f\t%-i\t%-f\n', OUTt{i,:});
end

fclose(fid);

%-----Generate Time Functions for ADINA-----%
cd 'C:\Documents and Settings\JOe\Desktop\Womersley
Mapping\time_funcs';
for i = 1:size(meat, 1)
    OUTtf = cell(size(time,2),2);
    filename = strcat('TIMEFUNC',num2str(i+start), '.txt');
    fid = fopen(filename, 'wt');
    fprintf(fid, '%50s\n', 'Node #      Load Type  Weight      Time
Function... Arrival Time      Birth Time  Death Time');

    for t = time(1):dt:period
        index = round((t+dt)/dt);
        OUTtf{index,1} = t;
        OUTtf{index,2} = wom_vels(i,index,2);
    %        fid = fopen(filename, 'wt');
    %        fseek(fid,0, 'eof');
        fprintf(fid, '%-f\t%-f\n', OUTtf{index,:});
    end
end
fclose(fid);

```

```

end

else

for t = time(1):dt:period
    index = round((t+dt)/dt);
    bound_points = zeros(size(bound,1),3);
    for n=1:size(bound)
        bound_points(n,1) = y(bound(n));
        bound_points(n,2) = z(bound(n));
        bound_points(n,3) = 0;
    end
    % index = 3;
    surfy = cat(1,wom_vels(:, index, 4),bound_points(:,1));
    surfz = cat(1,wom_vels(:, index, 5),bound_points(:,2));
    surfv = cat(1,wom_vels(:, index, 2),bound_points(:,3));

    %
    colormap Autumn

    surface = delaunay3(surfy, surfz, surfv, {'Qt', 'Qbb', 'Qc', 'Qz',
    'Pp'});
    XX =[surfz surfz surfv];
    C = ones(1,size(surface,1));
    tetramesh(surface,XX,C, 'FaceAlpha', 1, 'EraseMode', 'normal');

    if(type == 1)
        axis([-0.005 0.005 -0.005 0.005 -0.1 0.75]);
    else
        axis([-0.003 0.003 -0.003 0.003 -0.1 2.0])
    end

    axis normal;
    axis vis3d;
    campos([-0.05 -0.05 0.00])
    % campos([-3 -3 0.3])

    light('Position',[0 -2 1])
    F(index) = getframe;
    pause(0.004)

end

movie(F,3)

end

```

%-----END MOVIE-----

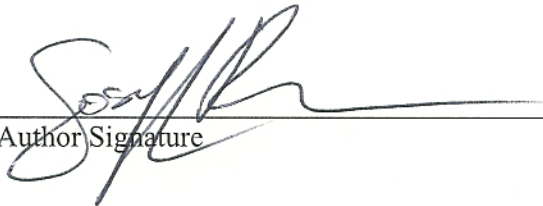


**Publishing Agreement**

*It is the policy of the University to encourage the distribution of all theses, dissertations, and manuscripts. Copies of all UCSF theses, dissertations, and manuscripts will be routed to the library via the Graduate Division. The library will make all theses, dissertations, and manuscripts accessible to the public and will preserve these to the best of their abilities, in perpetuity.*

***Please sign the following statement:***

*I hereby grant permission to the Graduate Division of the University of California, San Francisco to release copies of my thesis, dissertation, or manuscript to the Campus Library to provide access and preservation, in whole or in part, in perpetuity.*

  
\_\_\_\_\_  
Author Signature

9/1/09  
\_\_\_\_\_  
Date